The Dissertation Committee for Alexander Jin Pak Certifies that this is the approved version of the following dissertation:

First-Principles Investigation of Carbon-Based Nanomaterials for Supercapacitors

Committee:

Gyeong S. Hwang, Supervisor

John G. Ekerdt

Arumugam Manthiram

Deji Akinwande

Pengyu Ren

First-Principles Investigation of Carbon-Based Nanomaterials for Supercapacitors

by

Alexander Jin Pak, B.S.C.E.

Dissertation

Presented to the Faculty of the Graduate School of

The University of Texas at Austin

in Partial Fulfillment

of the Requirements

for the Degree of

Doctor of Philosophy

The University of Texas at Austin
August 2016

Dedication

To my mother, father, and sister for their support over the years and to Harley, my quirky but lovable cat.

Acknowledgements

First and foremost, I gratefully acknowledge Professor Gyeong S. Hwang, my dissertation supervisor, for his mentorship, advice, encouragement and patience throughout my graduate studies. I am immensely thankful for the countless hours he dedicated toward our lively scientific debates, discussions of my professional career, and meticulous review of our manuscripts and presentations. I would also like to express gratitude toward my other committee members – Professors John G. Ekerdt, Arumugam Manthiram, Deji Akinwande, and Pengyu Ren – for their invaluable insights and suggestions.

My fellow group members, both past and current, were an integral part of my journey as a student, mentor, and scientist. In particular, I would like to thank Eunsu Paek, Yongjin Lee, Kyoung E. Kweon, Yuhao Tsai, Haley Stowe, Matt Boyer, and Greg Hartmann for our many spontaneous and fruitful discussions. I am also grateful for the opportunity to interact with some brilliant experimental collaborators including Professors Rodney S. Ruoff, Christopher W. Bielawski, Li Shi, and Keji Lai and their students. Finally, I would like to acknowledge Professors Roger T. Bonnecaze and S.V. Sreenivasan who allowed me to participate in the NASCENT Center and their shared vision for nanomanufacturing.

My time in Austin was incredibly amazing thanks to the many friends I have made here. They encouraged me to try new things, supported me throughout graduate school, and hosted some legendary potlucks. I will miss them but I also know they will go on to

do great things. I also want to thank my family and their unwavering faith in me which has

allowed me to get to this point in my career.

<div align="right">Alexander J. Pak</div>

University of Texas at Austin

August 2016

First-Principles Investigation of Carbon-Based Nanomaterials for Supercapacitors

Alexander Jin Pak, Ph.D.

The University of Texas at Austin, 2016

Supervisor: Gyeong S. Hwang

Supercapacitors are electrochemical energy storage devices known for their large power densities and long lifetimes yet limited energy densities. A conventional understanding of supercapacitors relates the high power to fast ion accumulation at the polarized electrode interface, forming the so-called electric double layer (EDL), and the low energy to limited electrode surface area (SA). To improve the energy density, the capacitance may be enhanced by using high SA electrode materials such as carbon-based nanomaterials. While promising results have been experimentally reported, capacitances have also been noted to exhibit a highly non-linear relationship with SA. These interesting observations suggest that a gap exists in our fundamental understanding of charge storage mechanisms in the EDL of carbon nanomaterials. Given that EDLs are typically on the order of 1-3 nm thick, theoretical simulations can elucidate these unknown physical insights in order to identify new design principles for future electrode materials.

In this dissertation, we explore two broad types of carbon-based nanomaterials, which are separated into two Parts, using a combined density functional theory and classical molecular dynamics computational approach. In Part I, we study the capacitance

using various chemically and/or structurally modified graphene (or graphene-derived) materials which is motivated by previous accounts of the limited capacitance using pristine graphene. Our analysis demonstrates the viability of dramatically improving the capacitance using graphene-derived materials owing to enhancements in the quantum capacitance with marginal effects on the double layer capacitance. In Part II, we investigate the capacitance using nanoporous carbon materials which is motivated by experimental observations that relate capacitance to pore width rather than SA. Our findings confirm that promoting ion confinement through pore width control can enhance capacitance, but also identify pore shape dispersity as another important structural feature that facilitates fast ion dynamics during charging/discharging.

The work in this dissertation presents an overview of new insights into charge storage mechanisms using low-dimensional carbon-based nanomaterials and future directions for materials development. Moreover, we anticipate that the established methodologies and analyses can be broadly applicable to the study of other applications utilizing electrified interfaces, including capacitive deionization and liquid-gated field effect transistors.

Table of Contents

List of Tables

List of Figures

Chapter 1: Introduction

1.1 BACKGROUND AND MOTIVATION

A. Necessity of Energy Storage

The rise in global demand for energy has spurred an increasingly distributed variety of technologies and methods for energy conversion. However, providing the population access to energy requires efficient means of storage. For example, the disconnect between the energy supplied by intermittent alternative energy sources (*e.g.*, solar and wind) or power plants and the energy demanded by consumers using the electric grid can be bridged by large-scale energy storage technologies.[1,2] Small-scale energy storage is also a necessity as the world becomes increasingly reliant on mobile devices, electric vehicles, and other portable electronics.[3,4]

Within the energy storage landscape, two classes of technologies can be considered ubiquitous – electrochemical double layer capacitors (EDLCs) and batteries.[5,6] The major differences between the two are the rate at which charge can be stored/extracted (*i.e.*, the power density) and the total amount of charge that can be stored/extracted (*i.e.*, the energy density). As seen in Figure 1.1, batteries tend to have large energy densities (10-100 Wh/kg) but limited power densities (< 1 kW/kg). On the other hand, EDLCs (also referred to as supercapacitors) tend to have large power densities (1-10 kW/kg) and long lifetimes (> 100000 cycles). Due to these favorable properties, supercapacitors have been envisioned to provide high-power energy storage capabilities as both a stand-alone solution and hybrid

solution with batteries.[6,7] However, the adoption of these devices has been curtailed by their characteristically finite energy densities (< 5 Wh/kg). Given that the energy density ($E = \frac{1}{2}CV^2$) is proportional to the capacitance (C) and the square of the applied voltage (V), the ultimate aim of research directed towards EDLCs is to find strategies to improve C and V while maintaining their excellent power densities and lifetimes.
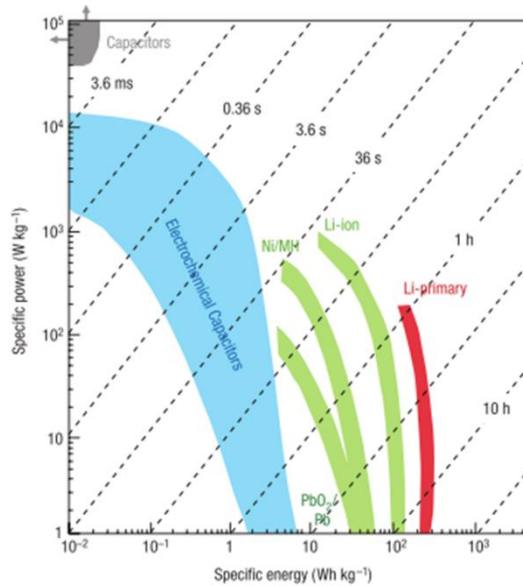
Figure 1.1   Ragone plot comparing the specific power (*i.e.*, how quickly charge is delivered) and energy (*i.e.*, how much charge it contains) of capacitors (grey and blue) and batteries (green and red). Reprinted by permission from Macmillan Publishers Ltd: Nature Materials, Simon and Gogotsi, Nature Materials, 7, 845, 2008, copyright 2008.

B. Supercapacitor Fundamentals

The history of supercapacitor devices dates back to 1957 when researchers at General Electric noticed that porous carbon materials filled with an aqueous salt or acidic solution (US Patent 2,800,616) could be used as a low-voltage electrolytic capacitor. The

first practical device, however, was introduced in 1962 by the Standard Oil Company of Ohio (US Patent 3,288,641) in which activated carbon black electrodes were used. In particular, the patent recognized the formation of the electric double layer (EDL) as the primary charge storage mechanism.

The conception of EDLs can be traced to the work of Helmholtz in 1853 when he made the observation that charges in a polarized metallic electrode accumulate at the surface and attract ions of opposite charge (so-called counter-ions).[8] The two distinct and segregated layers of charge formed by the electrode surface charge and the compact layer of counter-ions were collectively called the EDL. Due to the notable similarities to parallel-plate capacitors, the EDL was thought to have a constant C ($=\varepsilon_r\varepsilon_0/d$) proportional to the dielectric constant of the electrolyte (ε_r) and the separation distance between the surface ions and the electrode (d). However, subsequent work demonstrated that C was, in fact, not constant and depended on V. The work of Gouy and Chapman, and later amended by Stern, resolved this observation by showing that C essentially depended on two capacitors in series (now called GCS theory).[9] The first referred to the compact monolayer of ions accumulating at the electrode surface (the so-called inner Stern layer or inner Helmholtz layer) with constant capacitance C_H. The second was created by the diffuse outer layer of electrolyte ions with potential-dependent capacitance C_{GC}. The overall C, then, can be determined from the relative contributions of C_H and C_{GC} such that $1/C = 1/C_H + 1/C_{GC}$. More importantly, these theories underscored that the operation of supercapacitors strongly depends upon the molecular packing of ions at the electrode-electrolyte interface.

3

The patent by the Standard Oil Company of Ohio was also an important roadmap that has driven the direction of supercapacitor research since then. Two key points were highlighted. The first was the necessity of a conductive electrode material with large surface area (in this case, larger than 300 m^2/cm^3). The second was the recognition that the operating voltage was limited by the electrochemical stability of the electrolyte. Today, most supercapacitors in the market utilize activated carbon electrodes with aqueous or organic electrolytes. However, significant progress cannot be made unless new materials can be designed and fabricated.

To extend the operational voltage, and therefore the energy density, ionic liquids (ILs) have been widely explored as a potential electrolyte material. These solvent-free ions remain in the liquid phase at room temperature and have excellent thermal stability, tunable solvent properties, low volatility, and moderate ionic conductivity.[10,11] Most importantly, ILs are purported to have electrochemical window up to 4 V, which is much larger than that of aqueous (up to 1 V) or organic (up to 2.5 V) electrolytes.[5,12] Due to their small Debye lengths, which is comparable to the size of an ion, and the strong electrode-ion and ion-ion electrostatic interactions, IL ions display unique layering behavior that can extend up to a few nanometers.[13-15] In addition, the differential capacitance profiles using metal electrodes commonly show a convex parabolic shape with one maximum (*i.e.*, bell-shaped) or two local maxima (*i.e.*, camel-shaped) in contrast to the U-shaped profiles observed using aqueous electrolytes and predicted by GCS theory.[16-18] To explain these trends, theoretical studies have been shown to be well-suited for understanding the mechanistic relationships between the ion packing behavior at the interface, hereafter referred to as the

EDL microstructure, and the EDL capacitance (C_D). Kornyshev derived an elegant analytical expression based on the Poisson-Boltzmann lattice-gas model which identified the importance of the void fraction, or compressibility, of the EDL to explain the observed differential capacitance profiles.[19] Inspired by this work, molecular-level computer simulations have been used to further examine the relationship between the C_D and the EDL microstructure and identified many other factors – such as the size, configuration and polarizability of ions, the effective dielectric constant of the electrolyte solution, and the surface topology and shape of the electrode – as potentially important descriptors of the EDL capacitive behavior.[20-23] However, the relative importance of these factors, especially at the interface of different electrode materials, is not yet clearly understood; this leaves room for further investigation.

Carbon-based nanomaterials are another class of materials that offer rich possibilities for use as future EDLC electrodes.[24,25] Materials such as graphene, carbon nanotubes, templated carbon, nanoporous carbon, and carbide-derived carbon are all candidates owing to their large surface area, electrical conductivity, thermal conductivity, and excellent mechanical strength and flexibility. However, early experimental work using graphitic electrodes and ILs, such as highly ordered pyrolytic graphite (HOPG), were observed to display anomalous capacitive behavior compared to standard metallic electrodes; the differential C profiles exhibits the aforementioned U-shape in contrast to the bell-shape or camel-shape profiles observed in metal/IL systems.[26-28] To explain this inconsistency, the capacitance of the electrode itself must be considered. At the interface of a polarized semiconductor (or semimetallic) electrode and electrolyte, charge segregates

within the electrode surface forming the so-called space charge layer and essentially serves as another capacitor in series. Randin and Yeager first applied the semiconductor "space charge" capacitance picture for graphite with NaF.[29] Gerischer and coworkers[30,31] later amended this theory to incorporate the electronic density of states (DOS) of graphite within the framework of semiconductor theory; their analysis suggested that the finite DOS of graphite near the Fermi level resulted in the dominance of the space charge contribution to the measured capacitance. While the classical definition of the space charge layer cannot apply to low-dimensional carbon nanomaterials, the quantized nature of their electronic states lends itself to the adoption of the quantum capacitance (C_Q) formalism, which is proportional to the DOS.[13,32] Simply put, while C_D quantifies the ease in which ions can accumulate in the EDL to screen the applied electric field, C_Q quantifies the ease in which charge carriers can be injected into the electrode itself.

Combining the two contributions described above, it is evident that the total capacitance (C_T) at the electrode/electrolyte interface can be represented as a series of the C_Q and C_D, as shown in Figure 1.2(a), such that:

$$\frac{1}{C_T} = \frac{1}{C_Q} + \frac{1}{C_D} \tag{1.1}$$

In addition, as shown in Figure 1.2(b), the total applied potential (ϕ_a) is given by:

$$\phi_a = \phi_Q + \phi_D \tag{1.2}$$

in which ϕ_Q is the potential shift within the electrode and ϕ_D is the potential drop across the EDL. Understanding the relative contributions of the C_Q and C_D is a primary theme throughout this dissertation.
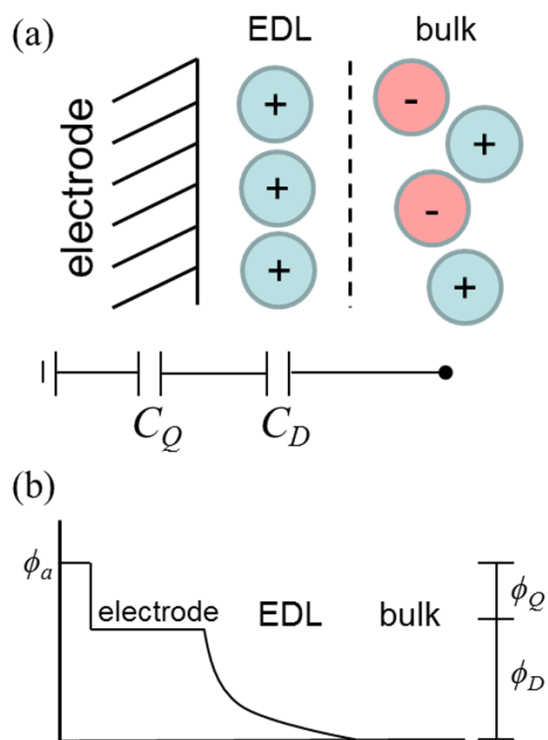
Figure 1.2 Schematic of the carbon nanomaterial electrode/ionic liquid interface with (a) an illustration of the equivalent circuit with series capacitance from the quantum (C_Q) and double layer (C_D) capacitances and (b) an idealized potential profile where the total applied potential (ϕ_a) is the sum of the electrode (ϕ_Q) and double layer (ϕ_D) potential drop.

1.2 RESEARCH OBJECTIVES

The broad aim of the research in this dissertation is to develop material design principles to help guide future directions in supercapacitor research by understanding the relationship between the chemistry and structure of carbon nanomaterials and the C_T once immersed in an IL. A computational approach is used in this work in order to probe the fundamental molecular mechanisms at the carbon nanomaterial/IL interface under external potential. The general computational framework is as follows. First, the structure of the

electrode is determined through a variety of simulation techniques ranging from Metropolis Monte Carlo methods to quantum mechanical calculations; an appropriate technique is determined on a case-by-case basis depending on the complexity of the disorder investigated. Next, the electronic structure and C_Q of the electrode is determined through quantum mechanical calculations. These calculations are also essential to understand the nature of excess charge accumulation. These insights, in turn, are utilized in classical molecular dynamics simulations to determine the EDL microstructure and C_D.

Two primary types of carbon nanomaterials are explored in this work. The first is graphene and its direct derivatives. Previous theoretical studies in our group[13,33] and independent experiments[34,35] have shown that despite the exceptionally high surface area of graphene (2630 m^2/g), its nature as a zero-gap semi-metal limits its C_T by virtue of its low C_Q. However, the electronic structure and C_Q may be tunable through the introduction of dopants, defects, and functional groups. Four different types of modifications to graphene, as described in the next section, are presented in this work. These studies also serve to develop a foundation to investigate more complex electrode materials, such as nanoporous carbon (NPC). Similar to graphene, NPCs consist of monolayer sp^2 carbon crumbled in three-dimensional networks. The current interest in NPCs largely stems from the observation that ions confined in pores comparable to their sizes exhibit dramatically enhanced areal C_T.[36,37] Understanding this mechanism is therefore the second focus of this work.

1.3 DISSERTATION OVERVIEW

The organization of the dissertation is as follows:

In Chapter 1, the background, motivation, research framework, and objectives are described. In Chapter 2, the theoretical background of the simulation techniques used in this work are explained.

In Part I of this dissertation, graphene-based materials immersed in ionic liquid electrolyte are explored. Specifically, the influence of four broad types of chemical and/or structural modifications to graphene on the electronic structure (and C_Q) and EDL microstructure (and C_D) is investigated. Chapters 3-6 accounts for point-like structural defects as represented by topological defects (Chapter 3), chemical dopants as represented by transition metal dopants (Chapter 4), extended structural defects as represented by edge defects (Chapter 5), and chemical functionalization as represented by hydroxyl functionalization of the basal plane (Chapter 6).

In Part II of this dissertation, nanoporous carbon materials immersed in ionic liquid electrolyte are explored. Specifically, the influence of pore size and curvature on C_T is investigated. The electronic structure and EDL microstructure outside of carbon nanotubes (Chapter 7) and within carbon nanotubes (Chapter 8) are presented. This work culminates in the study of capacitive mechanisms using nanoporous carbon materials with varying pore dispersity (Chapter 9).

Chapter 10 summarizes the overall conclusions of this dissertation and provides perspectives on potential future directions for research.

Chapter 2: Theoretical Background

2.1 SIMULATION TECHNIQUES

A. Quantum Mechanical Calculations

The basis of all quantum mechanical calculations is to find solutions to the wavefunction Ψ based on the Schrödinger equation[38]:

$$H\Psi = E\psi \tag{2.1}$$

in which the Hamiltonian (*H*) is a linear operator that describes the total energy (the combined kinetic and potential energy) of the system which consists of:

$$H = \sum_\alpha \frac{-\hbar^2}{2m_\alpha}\nabla^2 + \sum_i \frac{-\hbar^2}{2m_i}\nabla^2 + \sum_{\alpha,\alpha<\beta}\frac{e^2}{|r_\alpha-r_\beta|} + \sum_{i,i<j}\frac{e^2}{|r_i-r_j|} + \sum_{i,\alpha}\frac{e^2}{|r_i-r_\alpha|} \tag{2.2}$$

where the first two terms are the kinetic energies of the nuclei (denoted by the α and β subscripts) and electrons (denoted by the i and j subscripts) and the last three terms are the potential energies of the nuclei-nuclei, electron-electron, and electron-nuclei interactions. Beyond the case of small atoms and molecules (*e.g.*, hydrogen gas), analytical solutions to Equation (2.1) and (2.2) do not exist. However, numerical solutions are also computationally unwieldly due to the large number of degrees of freedom that are necessary in contemporary research. Two approximations are commonly used to overcome this deficiency.

The first approximation is known as the Born-Oppenheimer approximation.[39] Due to the large difference in nuclear and electronic mass (and therefore, large difference in kinetic energy), the nuclear and electronic Ψ are assumed to be decoupled such that the

electronic portion within Equation (2.2) can be solved assuming fixed nuclear positions. The electronic H therefore simplifies to:

$$H = \sum_i \frac{-\hbar^2}{2m_i}\nabla^2 + \sum_{i,i<j}\frac{e^2}{|r_i-r_j|} + \sum_i V_{ext}(r_i)$$ (2.3)

where V_{ext} is the external potential (*e.g.*, the nuclear contribution) felt by the electron. Unfortunately, the many-body electron-electron interactions still pose a significant computational burden. This problem is addressed by the second approximation which is broadly called density functional theory (DFT).

In 1964, Hohenberg and Kohn introduced two important theorems that lay the foundation for DFT methods.[40] The first theorem showed that in any system of interacting electrons under V_{ext}, the total energy and V_{ext} are a unique functional of the electron density $\rho(r)$. The second theorem stated that the ground-state energy can be obtained through the variational principle, such that the $\rho(r)$ that minimizes the total energy is the ground-state electron density. Under Hohenberg-Kohn theory, the total energy (E_{HK}) can be reformulated with respect to $\rho(r)$ by the following expression:

$$E_{HK} = T[\rho(r)] + V_{ee}[\rho(r)] + \int V_{ext}(r)\rho(r)dr$$ (2.4)

where $T[\rho(r)]$ and $V_{ee}[\rho(r)]$ are functionals for the kinetic energy and electron-electron potential energy, respectively. Yet, Equation (2.4) remained impractical as the exact functionals were unknown.

In 1965, the Kohn-Sham formulation was introduced and presented a practical means of solving Equation (2.4).[41] Here, the many-body problem (with order N^2) is

11

remapped to N non-interacting single electron problems interacting within an effective

Kohn-Shan potential (V_{KS}). The total electronic energy E_{KS} can be expressed as:

$$E_{KS} = T_S[\rho(r)] + E_{Hartree}[\rho(r)] + E_{XC}[\rho(r)] + \int V_{ext}(r)\rho(r)dr \qquad (2.5)$$

in which $T_S[\rho(r)]$ is the analytically known kinetic energy functional of a non-interacting

electron gas, $E_{Hartree}[\rho(r)]$ is the analytically known classical electrostatic energy of a non-

interacting gas, and $E_{XC}[\rho(r)]$ is the exchange-correlation functional which essentially

describes the small error in kinetic and potential energies between the exact and non-

interacting electron gas systems. As the potential is simply the derivative of the energy (for

example, $V_{KS} = \delta E_{KS}/\delta\rho(r)$), the single-electron Schrödinger equation can now be

simplified to:

$$\left[\frac{-\hbar^2}{2m_i}\nabla_i^2 + V_{Hartree}(r) + V_{xc}(r) + V_{ext}(r)\right]\Psi_i = \epsilon_i\Psi_i \qquad (2.6)$$

which can be solved self-consistently. In other words, numerical solvers can iteratively

solve Equation (2.6) by guessing an initial $\rho(r)$, constructing V_{KS} ($= V_{Hartree} + V_{xc} + V_{ext}$),

solving Equation (2.6) to calculate a new $\rho(r)$, and repeating until convergence is achieved.

By reducing the problem into N tractable equations, a considerable speed-up is

accomplished compared to all-electron methods. For periodic systems, another significant

speed-up is realized by using plane-wave basis sets to solve the Kohn-Sham equations in

reciprocal space.[42] However, the accuracy of the obtained results depends on the

approximations used to describe V_{xc} and V_{ext}. While the development of these

approximations has a long history, the common practices used in this dissertation will be

described. First, the E_{XC} is represented by the generalized gradient approximation (GGA)

which considers both $\rho(r)$ and $\nabla\rho(r)$ (a so-called semi-local functional). The most popular form of the functional was introduced by Perdew, Burke, and Ernzerhof (PBE) in 1996 and has successfully been used to predict the chemical, electronic, and optical properties of many materials.[43-45] In the second approximation, the all-electron problem is reduced to only the valence electrons as these tend to be the most chemically important; the core electrons are considered frozen (or tightly bound).[46] Therefore, a potential must be used to describe the interaction between valence and core electrons. Due to large number of basis sets required to describe the rapidly oscillating Ψ near the ion core, a technique called the projector augmented wave (PAW) method[47] is typically used to transform the all-electron Ψ into a smooth pseudo Ψ; note that outside a certain cutoff radius, the pseudo Ψ and all-electron Ψ are equal.

B. Classical Molecular Dynamics

The basis of all classical molecular dynamics (cMD) simulations is to calculate the positions (r_i) and velocities (v_i) of atoms over time (t) based on Newton's equation of motion[48]:

$$F_i = -\nabla E_i = m_i \frac{d^2 r_i}{dt^2} = m_i a_i \qquad (2.7)$$

where F_i is the per-atom force, E_i is the per-atom energy, m_i is the atomic mass, and a_i is the atomic acceleration. Through numerical time-integration of Equation (2.7), a time-dependent trajectory of atoms can be simulated. In addition, cMD simulations maintain a thermodynamic ensemble (*e.g.*, canonical NVT) in order to sample all possible atomic

microstates over time; according to the ergodic hypothesis, the time-averaged states are equivalent to the ensemble-averaged states which is necessary to estimate thermodynamic properties from statistical mechanics. Here, a key assumption is that the total energy can be described classically by a so-called force field. Given current computing power from the use of supercomputers, cMD simulations have successfully reported length- and time-scales up to millions of atoms and hundreds of nanoseconds, respectively[49]; unlike *ab-initio* MD simulations, cMD simulations assume that the quantum (or electronic) effects occur on length- and time-scales too small to be relevant.
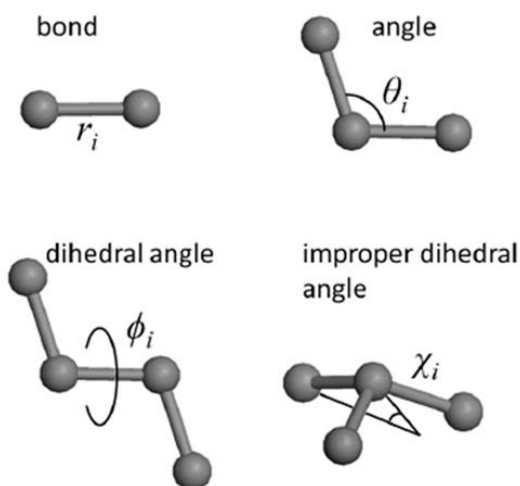
Figure 2.1   Schematic of the geometric properties used in the force fields to describe bonds, angles, dihedrals, and impropers.

The reliability of cMD is contingent on the appropriate choice of force field. Here, the force field refers to the model (both the functional form and the parameters) used to describe the energetics of the system. The force-field typically takes the following form:

$$E_{total} = E_{bond} + E_{angle} + E_{dihedral} + E_{improper} + E_{vdW} + E_{elec} \qquad (2.8)$$

14

in which the first four term describe the intra-atomic or bonding interactions (*e.g.*, within a molecule) and the last two terms describe the inter-atomic interactions (*e.g.*, electrostatic and van der Waals).

Many functional forms exist to describe the bonding and non-bonding interactions. The one most commonly used in this dissertation is the all-atom OPLS (Optimized Potentials for Liquid Simulations) force field[50], derived from the AMBER force field[51], which has the following form:

$$E_{bond} = \Sigma_{bonds} \frac{1}{2} K_b (r - r_o)^2 \tag{2.9}$$

$$E_{angle} = \Sigma_{angles} \frac{1}{2} K_a (\theta - \theta_o)^2 \tag{2.10}$$

$$E_{dihedral} = \Sigma_{dihedral} \Sigma_{n=1}^{4} \frac{V_n}{2} [1 - (-1)^n \cos(n\phi - \phi_n)] \tag{2.11}$$

$$E_{vdW} = \Sigma_{i>j} f_{ij} \left[4\epsilon_{ij} \left(\left(\frac{\sigma_{ij}}{r_{ij}} \right)^{12} - \left(\frac{\sigma_{ij}}{r_{ij}} \right)^{6} \right) \right] \tag{2.12}$$

$$E_{elec} = \Sigma_{i>j} f_{ij} \frac{q_i q_j e^2}{4\pi\epsilon_0 r_{ij}} \tag{2.13}$$

where K_b/K_a/V_n are the bond/angle/dihedral force constants and r_o/θ_o/ϕ_o are the equilibrium bond lengths/angles/dihedral angles with the geometric properties depicted in Figure 2.1. The bond and angle energies take the harmonic form while the dihedral energy takes the form unique to OPLS; note that the inclusion of impropers is usually unnecessary except in some cases when the harmonic form is taken. The van der Waals (vdW) energy follows the pair-wise 12-6 Lennard Jones form described by the potential well (ε_{ij}), zero-energy distance (σ_{ij}), and radial distance between atoms *i* and *j* (r_{ij}).[52] The electrostatic energy is described using the classical Coulomb relation based on the atomic charges q_i/q_j and the

vacuum permittivity (ε_0).[53] A fudge factor (f_{ij}) is introduced to scale the vdW and electrostatic interaction energies for bonded atoms (up to the 3rd nearest connected neighbor). Finally, a practical cut-off radius (r_c) is introduced to limit the computational burden of calculating all of the non-bonding interaction energies. This r_c is commonly around 12 Å, which is large enough to sufficiently capture the relevant vdW interactions due to its rapid decay. However, this can introduce large errors in the electrostatic energy due to its long-range nature. To overcome this limitation, the long-range contribution to the electrostatic energy is computed using Ewald summations, which offers a fast way to approximate this energy in Fourier space if periodicity is assumed.[54,55] Another way to speed-up computations is to use a coarse-grained approach in which several atoms are grouped together into a single interaction center to significantly reduce the number of pairwise (and bonding) interactions that require computation.[56,57]

Once the energies are calculated, the computed forces are used to update atomic velocities and positions through numerical time-integration of Equation (2.7). The naïve approach is to use the Taylor expansion of r_i such that $r_i(t+\Delta t) = r_i(t) + v_i(t)\Delta t + a_i(t)\Delta t^2/2 + O(\Delta t^3)$ where Δt is the simulation time step. However, this method is known to introduce large errors and significant drift in energy due to errors in the predicted velocities.[58] Many time-integration methods have therefore been developed to be both efficient and reduce errors. One popular scheme is known as the Velocity Verlet algorithm[59] which is simplified to the following 4 steps:

1. Calculate $v_i(t+\tfrac{1}{2}\Delta t) = v_i(t) + \tfrac{1}{2}a_i(t)\Delta t$

2. Calculate $r_i(t+\Delta t) = r_i(t) + v_i(t+\tfrac{1}{2}\Delta t)\Delta t$

16

3. Calculate $a_i(t+\Delta t)$ from the forces based on $r_i(t+\Delta t)$

4. Calculate $v_i(t+\Delta t) = v_i(t+\tfrac{1}{2}\Delta t) + \tfrac{1}{2}a_i(t+\Delta t)\Delta t$

Integration using this method conserves the total energy, yielding the microcanonical ensemble (*NVE*) where the total number of atoms N, the system volume V, and the total energy E are fixed.

In most cases, it is helpful to sample the system under different thermodynamic ensembles in order to emulate more realistic experimental conditions. For example, the canonical ensemble (*NVT*) can be used to assess the microstates of a system in thermal equilibrium with a heat bath while the isobaric-isothermal ensemble (*NPT*) can be used to do the same for systems under constant pressure conditions. Doing so requires an external bias to the system, which therefore removes energy conservation and requires modifications to the equations of motion.[60] This external bias is known as a thermostat when the temperature is controlled and as a barostat when the pressure is controlled. Again, many thermostats and barostats have been developed but for the purposes of this dissertation, the commonly used Nosé-Hoover thermostat[60] will be reviewed.

The Nosé-Hoover thermostat is an extended Lagrangian approach that connects the physically simulated system to a fictitious heat bath between which heat can be exchanged. The benefit of this approach compared to other approaches, such as velocity re-scaling, Berendsen, and Anderson thermostats, is that the kinetic energy samples a canonical distribution centered around the target T_0 in conjunction with smoothly changing dynamics. The fictitious heat bath is included as an extra degree of freedom s with velocity v_s

(typically substituted with $\gamma = v_s/s$) and effective mass Q (*i.e.*, the degree of coupling) such that the Hamiltonian is now:

$$H = \sum_i \frac{1}{2} m_i v_i^2 + E_{total}(r) + \frac{1}{2} Q\gamma^2 + N_{df} k_B T_0 ln(s) \tag{2.14}$$

where the first two (final two) terms are the kinetic and potential energies of the real (virtual) system and N_{df} refers to the degrees of freedom. The equations of motion are accordingly amended:

$$\frac{dr_i^2}{dt} = \frac{F_i}{m_i} - \gamma r_i \tag{2.15}$$

$$\frac{d\gamma}{dt} = \frac{-k_B N_{df}}{Q} T(t) \left(\frac{T_0}{T(t)} - 1\right) \tag{2.16}$$

Note that this approach introduces a natural fluctuation in T that depends on the choice of Q. The frequency of these oscillations can be estimated from the effective relaxation time τ_{NH}:

$$\tau_{NH} = \sqrt{\frac{Q}{N_{df} k_B T_0}} \tag{2.17}$$

2.2 CAPACITANCE CALCULATIONS

A. Quantum Capacitance

The quantum capacitance (C_Q) is a term that refers to the capacitance of an electrode with quantized electronic states.[32] Essentially, the C_Q indicates the ease in which excess charge carriers (*i.e.*, electrons and holes) fill these quantized states. This is appropriate for the electrode materials explored in this dissertation as they are low-dimensional carbon

nanomaterials. The differential $C_{Q,diff}$ is defined as $d\sigma/d\phi_G$, where $d\sigma$ and $d\phi_G$ refer to the variations of excess charge density and local potential in graphene, respectively. Under an external bias, the electrochemical potential is assumed to rigidly shift by μ $(=-e\phi_G)$. Hence, the excess charge density σ from the electron density (n) can be analytically expressed by:

$$\sigma = e(n_o - n_\mu) = e \int_{-\infty}^{\infty} D(E)[f(E) - f(E+\mu)]dE \qquad (2.18)$$

where $D(E)$ is the density of states, $f(E)$ is the Fermi-Dirac distribution function, E is the relative energy with respect to E_F, e is the elementary charge, and the subscripts o and μ refer to the neutral and non-neutral cases, respectively. Subsequently, the $C_{Q,diff}$ of graphene is given by:

$$C_{Q,diff} = d\sigma/d\phi_G = e^2 \int_{-\infty}^{\infty} D(E)F_T(E+\mu)dE \qquad (2.19)$$

where the thermal broadening function ($F_T(E)$) is also expressed as:

$$F_T(E) = -\frac{df}{dE} = (4k_BT)^{-1} \operatorname{sech}^2 \frac{E}{2k_BT} \qquad (2.20)$$

Note that the integral $C_{Q,int}$ can be obtained from the integration of $C_{Q,diff}$ such that:

$$C_{Q,int} = \frac{\int_0^{\phi_G} C_{Q,diff}d\phi}{\phi_G} \qquad (2.21)$$

B. Double Layer Capacitance

The double layer capacitance (C_D) is a term that refers to the capacitance of the EDL that develops at the electrode-electrolyte interface under an applied potential. The two definitions commonly used are the differential $C_{D,diff}$ and the integral $C_{D,int}$ with the following forms:

$$C_{D,diff} = \frac{d\sigma}{d\phi_D} \tag{2.22}$$

$$C_{D,int} = \frac{\sigma}{\phi_D} \tag{2.23}$$

where σ is the electrode surface charge density and ϕ_D is the potential drop over the EDL.

The surface charge at the electrode-electrolyte interface is commonly modeled using two techniques. The first is called the constant-charge condition in which fixed charges are used for each electrode atom. In the simplest case, the charges are distributed uniformly. However, in the presence of defects and dopants, charge tends to redistribute along the electrode surface and can be estimated from quantum mechanical approximations, such as the Bader charge method[61] or RESP method[62]. Given that the σ is fixed, the ϕ_D must be computed from the microstructure of the electrolyte. This is done by solving Poisson's equation in one-, two-, or three-dimensions depending on the system under investigation:

$$\nabla^2\phi = -\frac{\rho_q}{\epsilon_0} \tag{2.24}$$

where ρ_q is the time-averaged spatial charge density extracted from the simulation trajectories. From the ϕ profiles, ϕ_D is calculated as the difference between the electrode surface potential and the bulk electrolyte potential. Note that the choice of boundary conditions will also depend on the system under investigation.

The second scenario is called the constant-potential condition in which the electrode point charges are allowed to fluctuate at a fixed potential. There are numerous methods[63] of doing this but only one method is used in this dissertation and described in Chapters 8 and 9. In this case, two electrodes are required in the simulation and ϕ_D is

typically redefined in terms of the overall potential difference between the surfaces of the positively and negatively polarized electrodes. As such, the time-averaged σ is used to calculate the integral capacitance of the two-electrode cell $C_{D,cell} = \sigma/\phi_D$.

C. Interfacial Capacitance

As described in Chapter 1, the total interfacial capacitance (C_T) is given by the series capacitances of C_Q and C_D following Equation (1.1). However, the C_Q and C_D can only be combined when the σ associated with both values is equivalent. Hence, the easiest way to compute C_T is to evaluate ϕ_a from Equation (1.2) at a given σ since the integral $C_T = \sigma/\phi_a$.

PART I: GRAPHENE-DERIVED MATERIALS

In Part I, the fundamental charge storage mechanisms in graphene-based materials are explored using a combined density functional theory (DFT) and classical molecular dynamics (MD) methodology. Although the excellent electrical conductivity and high specific surface area of graphene motivates its use as a supercapacitor electrode material, recent results have demonstrated that the intrinsically low quantum capacitance of graphene can inhibit the total capacitance. This work aims to develop graphene modification strategies, encompassing both chemical and structural changes, as a viable means of engineering graphene-derived materials for use in supercapacitors.

Several types of modifications are independently investigated. First, localized defects and/or chemical dopants on the basal plane of graphene are considered, such as topological point-like defects and transition metal dopants. Then, extended edge defects with different passivation chemistries are investigated. Finally, oxidation of the basal plane, such as seen in graphene oxide, is studied. In all of these cases, the intent is to probe the influence of disorder throughout the graphene π system on the accumulation of both the electrode charge carriers and the electrolyte ions at the interface.

Chapter 3: Topological Point-like Defects

Work in this chapter was published and reprinted from Carbon, Vol. 68, A. J. Pak, E. Paek, and G. S. Hwang, Tailoring the Performance of Graphene-based Supercapacitors using Topological Defects: A Theoretical Assessment, pg. 734−41, Copyright (2014), with permission from Elsevier.

3.1 INTRODUCTION TO POINT-LIKE DEFECTS

Topological point-like defects describe structural deformations to the pristine graphene lattice, including non-hexagonal rings, localized vacancies, and hillock deformations. Depending on the growth conditions or processing by either irradiation or chemical treatment, these defects have been readily observed on the basal plane of graphene.[64-67]

In this chapter, the impact of topological defects primarily on the electronic structure and quantum capacitance (C_Q) of graphene are examined. Three types of topological defects – Stone Wales, di-vacancies, and di-interstitials – are simulated using density functional theory (DFT) at a defect density $n_d = 3 \times 10^{13}$ cm^{-2} ($\approx$ 0.8-1.6 at.%). The influence these defects have on the double layer capacitance (C_D), and therefore the overall capacitance (C_T), are briefly discussed. Finally, strategies to tune the electronic structure using topological defects are presented.

3.2 COMPUTATIONAL METHODS

The atomic and electronic structures of pristine and defective graphene sheets were calculated using DFT within the Perdew-Wang 91 generalized gradient approximation (GGA-PW91)[68], as implemented in the Vienna Ab initio Simulation Package (VASP)[42]. The projector augmented wave (PAW) method[69] was used to describe the interaction between ion core and valence electrons based on a planewave basis set with a kinetic energy cutoff of 400 eV. The simulation domain consisted of a hexagonal 8×8 supercell with a GGA-optimized lattice constant of 2.466 Å and a vacuum space of 15 Å in the z direction to avoid interactions with the periodic image. Each supercell had one defect, corresponding to a defect density of 3.0×10^{13} cm^{-2} ($\approx$ 0.8-1.6 at.%). For the Brillouin zone integration, a (6×6×1) Monkhorst-Pack (M-P) k-point mesh[70] for geometry optimization and energy calculations and a (12×12×1) M-P k-point mesh for electronic structure calculations were employed. Bader charge[61] distributions were calculated using a rectangular 4×8 supercell with the same lattice constant, vacuum spacing, and k-point mesh under charge neutral conditions and with the injection of one electron or hole. The larger, mixed-defect system was created using a rectangular 8×16 supercell (34.18×39.46 Å^2) with 15 Å of vacuum space; here, (3×3×1) and (6×6×1) M-P k-point meshes were used for geometry optimization and electronic structure calculations, respectively.

3.3 DEFECT STRUCTURES AND FORMATION ENERGIES

A variety of topological defects can be found in graphene, including the three types of point-like defects considered here: Stone Wales (SW), di-vacancies (DVs), and di-interstitials (DIs). The most fundamental of these is the SW defect[71], which occurs when a C-C bond rotates in-plane 90° and results in the structure with two pentagons and two heptagons shown in Figure 3.1(a). According to our DFT-GGA calculations, the formation energy $E_f = 5.0$ eV, which is in good agreement with previously reported values (≈ 5 eV).[71,72]
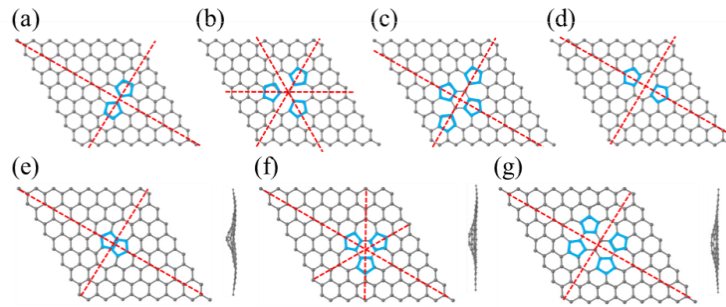
Figure 3.1   Schematic of the investigated topological defect structures: (a) SW, (b) V_2(555-777), (c) V_2(5555-6-7777), (d) V_2(5-8-5), (e) I_2(ISW), (f) I_2(555-6-777), (g) I_2(5555-66-7777). Symmetry lines are shown as red, dashed lines. Five-membered carbon rings are outlined in blue. The SW and V_2 structures (upper panels) remain planar while the I_2 structures (lower panels) contain hillocks that are shown in the side-view snapshots.

DVs in graphene can be created through either the agglomeration of mono-vacancies or the ejection of adjacent C atoms and have been observed using high resolution transmission electron microscopy.[65,66,73] Figure 3.1(b)-(d) shows three possible DV reconstructions: V_2(555-777), V_2(5555-6-7777), and V_2(5-8-5). The predicted E_f of these defects range from $6.7 < 7.2 < 7.6$ eV for V_2(555-777) $< V_2$(5555-6-7777) $< V_2$(5-8-5).

DV defects also tend to be stationary with a migration barrier around 7 eV.[74] Mono-vacancies, on the other hand, tend to be mobile (with a barrier of 1-2 eV) and can be annihilated after thermal annealing.[74] We therefore do not consider mono-vacancies in this analysis.

The formation of DIs has been proposed through the adsorption of C-C dimers, which results in local corrugations or so-called hillocks.[75,76] Figure 1(e)-(g) shows three minimum-energy DI structures considered: the inverse SW I_2(ISW), I_2(555−6−777), and I_2(5555-66-7777). The E_f of these defects are predicted to range from 6.2 < 6.6 < 7.3 eV for I_2(ISW) < I_2(555-6-777) < I_2(555-66-7777). Similar to DVs, DI defects are also expected to be fairly stationary, although single C adatoms have been predicted to be mobile with a barrier of 0.4−0.9 eV.[77,78]

3.4 RELATIONSHIP BETWEEN DEFECTS AND ELECTRONIC STRUCTURE

We calculated the electronic band structure and density of states (DOS) of each of the fully relaxed defects using DFT. Point-like topological defects locally reconstruct the lattice and thereby reduce the six-fold symmetry of graphene (D_{6h}) to either two-fold (D_{2h} or C_{2v}) or three-fold (D_{3h} or C_{3v}) symmetry. The high symmetry lines along the Γ-K-M-Γ Brillouin zone (BZ) path are usually sufficient to represent the important features of the band structure for six- and three-fold symmetry. However, the two K_1/K_2 and M_1/M_2 are no longer symmetric in the case of two-fold symmetry as seen in Figure 3.2. We therefore

compare the extended Γ-K_1-M_1-Γ-M_2-K_2-Γ BZ path for each defect, despite the redundancy in the three-fold cases.
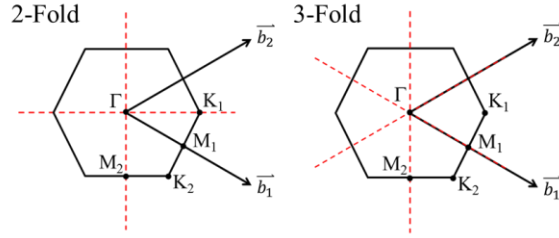
Figure 3.2   Schematic of the Brillouin zones for the listed degree of symmetry. The high symmetry points, symmetry lines, and reciprocal lattice vectors are also shown.
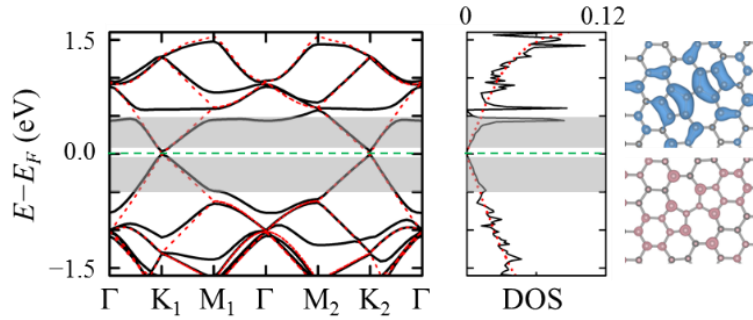
Figure 3.3   Band structure (left) and density of states (DOS in eV^{-1} Å^{-2}) (middle) of the Stone-Wales defect (black, solid) and pristine graphene (red, dashed) cases with the Fermi level indicated by the green, dashed line. Band decomposed charge density isosurfaces of the shaded regions are displayed to the right ($\pm$0.002 e/bohr^3).

Figure 3.3 shows the band structure [left] and DOS [middle] of the SW defect (black) compared to pristine graphene (red, dashed). In the latter case, the valence (VB) and conduction (CB) bands display linear dispersion that extends about 1 eV. In the SW case, however, the bands near the Fermi level (E_F) are partially flattened; this effect is more marked around 0.45 and 0.60 eV above E_F and gives rise to the distinct peaks in the DOS that are a well-known characteristic of the SW defect[79,80]. These flat bands are indicative

27

of the quasi-localization of the p_z states in the vicinity of the SW defect, due to the disruption of the graphene π system. Hence, injected charge carriers, especially electrons, will accumulate near the pentagon-heptagon C rings, as seen from the band decomposed charge density isosurfaces [right]. However, the flat bands are also smoothly connected to the low-energy dispersion of graphene (more so in the filled states), which suggests that a large fraction of the excess charge can also widely spread over the graphene lattice.
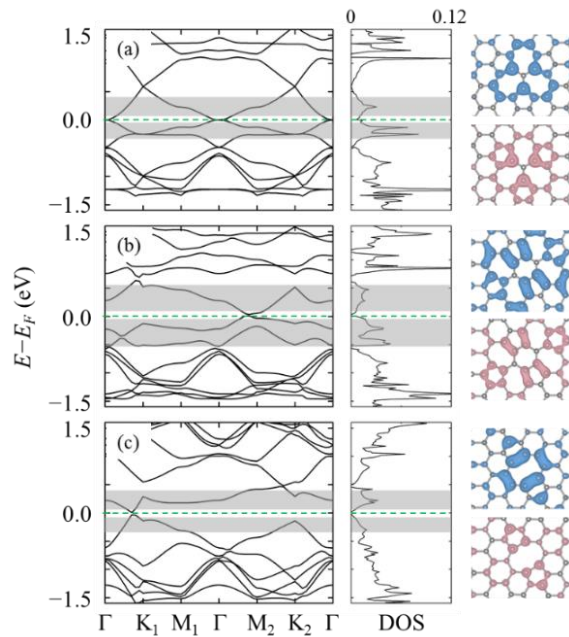
Figure 3.4   Band structure (left) and density of states (DOS in eV^{-1} Å^{-2}) (middle) of the (a) V$_2$(555-777), (b) V$_2$(5555-6-7777), and (c) V$_2$(5-8-5) cases with the Fermi level indicated by the green, dashed line. Band decomposed charge density isosurfaces of the shaded regions are displayed to the right (± 0.002 e/bohr^3).

Figure 3.4 shows the band structures [left] and DOS [middle] for each of the DV structures. In all three cases, the E_F is shifted down below the VB of graphene primarily due to electron deficiency; note that V$_2$ removes two electrons from the π system of graphene. The DOS plots show several pronounced peaks near the E_F which correspond to

partial flattening of the bands, in good agreement with previous work[79]. This is apparently

attributed to the quasi-localized p_z states in the vicinity of the DV defects, as also depicted

in the band decomposed charge density isosurfaces. The degree of localization, however,

tends to successively decrease in the V_2(555-777), V_2(5555-6-7777), and V_2(5-8-5) cases;

this is well demonstrated by the increased dispersion of the corresponding bands and the

broadening of the DOS peaks within 0.5 eV below E_F. The difference in localization

tendency amongst the DV configurations is likely related to the relative stability of the

coupling of the p_z states in the defect region. In addition, the increased coupling of the

quasi-localized p_z states in the V_2(555-777) > V_2(5555-6-7777) > V_2(5-8-5) cases is

reflected by the respective decrease in E_f and increase in the shift of E_F from that of

graphene [Figure 3.5].
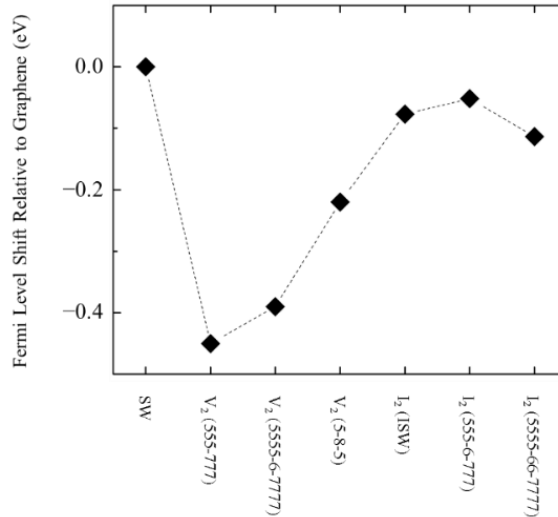
Figure 3.5   DFT-calculated shift in the Fermi level relative to graphene for each of the
            listed topological defect cases. The dotted line is a visual guide.
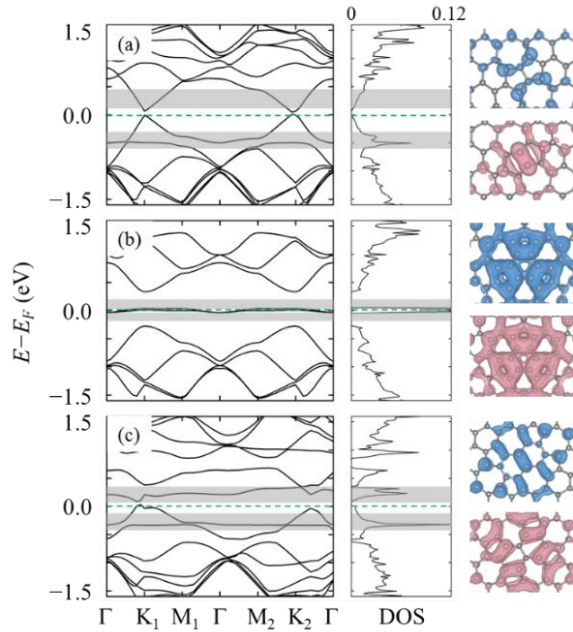
Figure 3.6 Band structure (left) and density of states (DOS in eV^{-1} $Å^{-2}$) (middle) of the (a) I_2(ISW), (b) I_2(555-6-777), and (c) I_2(5555-66-7777) cases with the Fermi level indicated by the green, dashed line. Band decomposed charge density isosurfaces of the shaded regions are displayed to the right (±0.002 e/bohr^3).

The band structures [left] and DOS [middle] for each of the DIs are presented in Figure 3.6. Here, the introduction of the C-C dimer creates defect states near E_F, rather than adding two electrons into the π system of graphene and shifting the E_F above the CB. Furthermore, the graphene lattice is distorted and forms so-called hillocks in each of these cases, thereby disrupting the graphene π system. Depending on the defect type, the additional p_z states tend to be partially coupled to the graphene π bands as seen in the I_2(ISW) and I_2(5555-66-7777) cases or highly localized such as in the I_2(555-6-777) case. Comparing the former two cases, we observe that the dispersion of the bands is reduced (or the DOS peaks are sharpened) within 0.6 eV of E_F in the I_2(5555-66-7777) case,

suggesting that a greater fraction of p_z states are quasi-localized as a result of the greater extent in lattice disorder. In the I_2(555-6-777) case, the partially filled flat bands (or sharp DOS peaks) at E_F are primarily attributed to the sp^3-like dangling bonds and p_z orbitals of the hillock C atoms. Similarly, such flat bands at E_F have been identified in zigzag graphene nanoribbons (GNR) in large association with the sp^2-like dangling bonds.[81] These results suggest that upon electron (hole) injection, the quasi-localized states in the vicinity of the defect are preferentially filled (emptied).

3.5 IMPACT OF TOPOLOGICAL DEFECTS ON QUANTUM CAPACITANCE
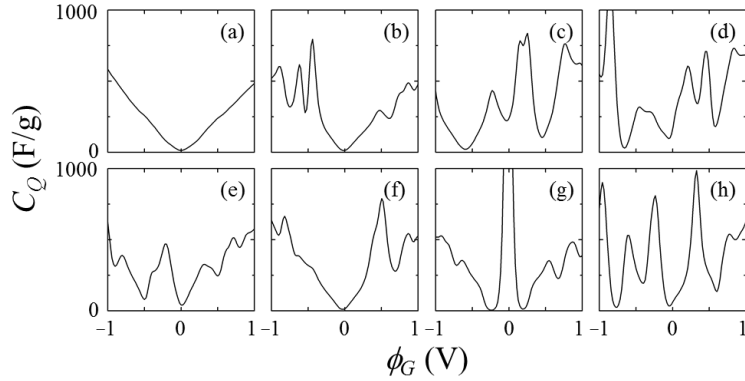
Figure 3.7   Calculated differential quantum capacitance (C_Q) of the (a) pristine graphene and the (b) SW, (c) V_2(555-777), (d) V_2(5555-6-7777), (e) V_2(5-8-5), (f) I_2(ISW), (g) I_2(555-6-777), and (h) I_2(5555-66-7777) defect cases.   All profiles are shown as a function of the local electrode potential (ϕ_G).

Figure 3.7 shows the calculated differential C_Q for pristine [(a)] and each of the defective [(b)-(h)] graphene electrodes at 300 K, which tend to resemble their respective DOS profiles under thermal broadening. In Figure 3.7(a), we observe that the C_Q of pristine graphene is zero at $\phi_G = 0$ V where the Dirac cone is located but increases linearly to around

500 F/g at $\phi_G = \pm 1$ V. In contrast, all of the defective graphene sheets tend to have highly irregular C_Q profiles with local sharp enhancements close to the neutrality point; these peaks correspond to the aforementioned quasi-localized p_z states.
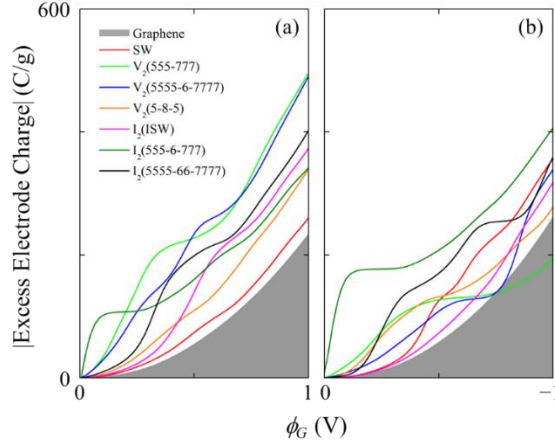
Figure 3.8   Comparison of the total amount of excess charge stored under (a) positive and (b) negative bias for pristine graphene and each defective graphene sheet as a function of the local electrode potential (ϕ_G).

In Figure 3.8, we show σ as a function of ϕ_G to represent the cumulative excess charge in the electrode (*i.e.*, the integral σ) at a given electrode potential. The defective graphene electrodes generally store more charge than pristine graphene within the 2 V window presented here, although the $V_2(555\text{-}777)$ case is the exception beyond $\phi_G < -0.75$ V. This increased charge capacity is a direct consequence of the additional availability of states near E_F. In other words, to achieve the same electrode charge density, a lower ϕ_G is required for the defective graphene electrodes. However, it is also evident that these electrodes no longer store charge symmetrically. As a result, certain defect types are better suited for different terminals; the SW case, for example, is clearly more effective as a

negative electrode while the V_2(555-777), V_2(5555-66-7777), and I_2(ISW) cases are more effective as positive electrodes.

3.6 INFLUENCE ON THE DOUBLE LAYER AND TOTAL INTERFACIAL CAPACITANCE

Along with C_Q, the electric double layer (EDL) capacitance (C_D) will also influence the total interfacial capacitance (C_T), which is given by $1/C_T = 1/C_Q + 1/C_D$. The EDL capacitance is evaluated based on the microstructure of the electrolyte near the electrode under applied potential and has been studied using computational methods for a variety of ILs near pristine graphene.[13-15,82,83] However, the presence of defects affects the charge distribution along the electrode surface, which in turn may influence the IL arrangement near the surface. For example, previous work[33] with nitrogen-doped graphene (at 2.7 at.%) showed that the maximum (minimum) atomic charge near the defect sites was 0.66 (−1.14) e when $\sigma = 5.43$ μC/cm^2. Yet, the N-doping was found to have little influence on the EDL microstructure and capacitance.
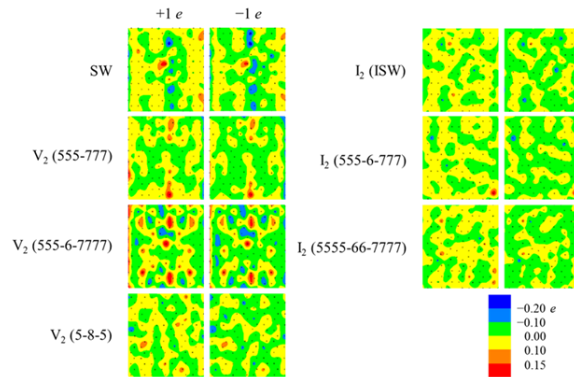
Figure 3.9   Electrode charge distributions calculated from Bader charge analysis for each defect case after one electron or hole (per supercell) has been added.
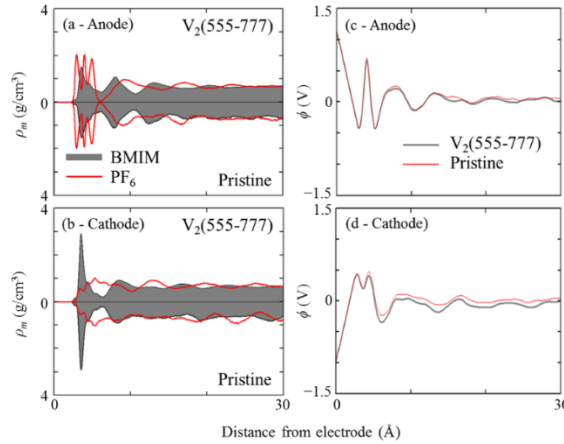
Figure 3.10 Mass density (ρ_m) profiles for the anode (a) and cathode (b) and potential (ϕ) profiles for the anode (c) and cathode (d) for [BMIM][PF$_6$] IL using V$_2$(555-777) and pristine graphene electrodes at $\sigma = \pm 4.75$ μC/cm^2. Here, the potential of the bulk electrolyte is set to $\phi = 0$ V.

According to Bader charge analysis [Figure 3.9], the injection of one electron or hole into the defect lattice is spread broadly, with a maximum (minimum) atomic charge of 0.20 (−0.25) e on select atoms. Given that the charge distribution exhibits smaller fluctuations compared to the N-doped case, we can expect that these small point-like topological defects will also have a marginal effect on C_D. To test this, we computed the EDL microstructure near V$_2$(555-777) electrodes, as depicted in Figure 3.10(a)-(b), and find that the packing of IL ions is nearly the same as that of the pristine graphene interface. As a result, the potential profiles, and therefore C_D, remain unperturbed (Figure 3.10(c)-(d)). We should note that in the DI cases, the curvature of the hillocks could additionally affect C_D; previous studies have demonstrated that C_D improves with increasing electrode curvature[20,84,85] or surface roughness[86]. However, we can expect the effect of surface topology on C_D to also be marginal since the hillocks are both isolated and have small curvature. In short, the C_D using graphene electrodes with the considered topological

34

defects is likely similar to that of pristine graphene electrodes, although this may not be the case when we consider larger concentrations of defects or larger-scale defects.

Due to the aforementioned relationship between C_Q and C_D to C_T, we can expect C_T to increase due to the enhanced C_Q as depicted in Figure 3.11. To the best of our knowledge, comparisons to experimental results are not possible at this time since the (differential) C_T of supercapacitors using graphene with topological defects has never been reported. But we should also note that our quantitative results may require further refinement. For instance, we have neglected the possible polarization of the electrodes[87,88] and IL ions at the interface and its effects on the electrode charge redistribution, the space charge density, and subsequently, C_D. In addition, the DOS (and C_Q) may be altered to a certain extent if the electronic structure is locally modified by electrode-IL interactions, which were omitted for simplicity. Nonetheless, our analysis clearly shows that topological defects can have a profound impact on, and likely improve, C_Q and thus, C_T.
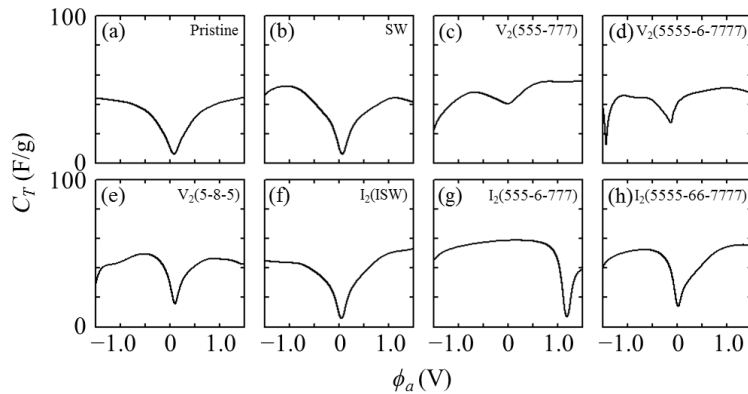
Figure 3.11 The (differential) total interfacial capacitance (C_T) of [BMIM][PF$_6$] IL using the listed types of graphene electrodes. The double layer capacitance for each case was represented by that of pristine graphene.

35

3.7 TUNING THROUGH COMBINATIONS OF TOPOLOGICAL DEFECTS

In the previous section, we presented the electronic structure and C_Q of individual topological defects. Experimentally, however, it may be quite challenging to recreate such homogeneity along the graphene lattice. Therefore, in this section, we increase the complexity by exploring the impact of having different combinations of topological defects on the electronic structure and C_Q. To this end, we have simulated two scenarios: graphene sheets with an overall $n_d = 3 \times 10^{13}$ cm^{-2} using (1) SW, V_2(555-777), I_2(555-6-777), and I_2(5555-66-7777) defects [Figure 3.12(a)] and (2) V_2(555-777) and I_2(5555-66-7777) defects at a 3:1 ratio [Figure 3.12(b)].

Figures 3.12(a)-(b) show the DOS of each of the two configurations of defective graphene sheets, which exhibit several sharp peaks near E_F. According to our analysis of the projected DOS [Figure 3.13 and 3.14], each of these peaks is attributed to a particular defect-induced quasi-localized state (see markings), which has been similarly observed in previous theoretical work.[79,89] Note that the positions of these quasi-localized states relative to each other remain largely unchanged; the position of E_F is approximated by the (density-weighed) average positions of each E_F in the associated individual defect cases (which can be possible when long-range coupling between adjacent defect types is absent). This analysis implies that the following two-step process can be used to tailor the electronic structure of defective graphene: (1) determine the relative positions of quasi-localized states from the chosen array of topological defects and (2) shift the position of E_F based on the densities of each topological defect. However, this procedure is likely possible only

when defect states are both relatively close in energy and coupled to the π system; without these conditions, gaps in the DOS would appear between the localized states.
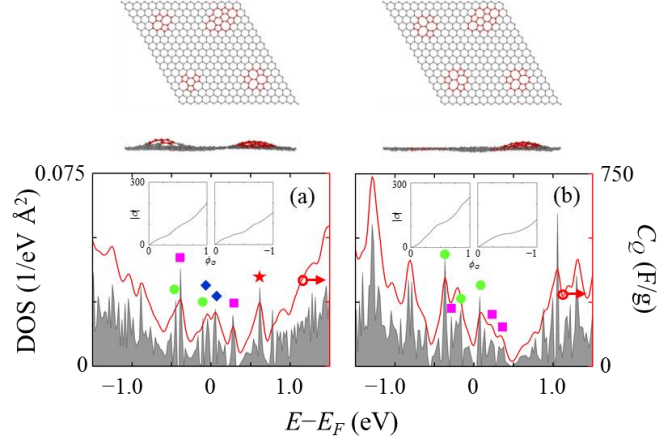
Figure 3.12 The density of states (DOS) and quantum capacitance (C_Q) of the (a) SW/V$_2$(555-777)/I$_2$(555-6-777)/I$_2$(5555-66-7777) and (b) V$_2$(555-777)/I$_2$(5555-66-7777) at 3:1 ratio mixed defect cases (the upper panel shows top- and side-view schematics of the corresponding structures with the defect region highlighted in red); the DOS (C_Q) is depicted by the shaded region (red line). The markings indicate the positions of resonant defect states associated with the (★) SW, (●) V$_2$(555-777), (◆) I$_2$(555-6-777), and (■) I$_2$(5555-66-7777) defects. The inset shows the excess electrode charge ($|\sigma|$ in C/g) as a function of electrode potential (ϕ_G in V).

Figure 3.12(a)-(b) also depict the predicted C_Q of the mixed defect electrodes at 300 K. We additionally plot σ as a function of ϕ_G in the insets. Similar to the individual defect cases, while σ tends to be larger than that of pristine graphene, the predicted enhancement will vary between the positive and negative terminal. In fact in both cases, a larger σ is favored at the positive electrode. This suggests that graphene electrodes can be individually tailored for operation as either the positive or negative electrode; the use of asymmetric electrodes for supercapacitors has the potential to significantly increase performance and deserves further investigation.
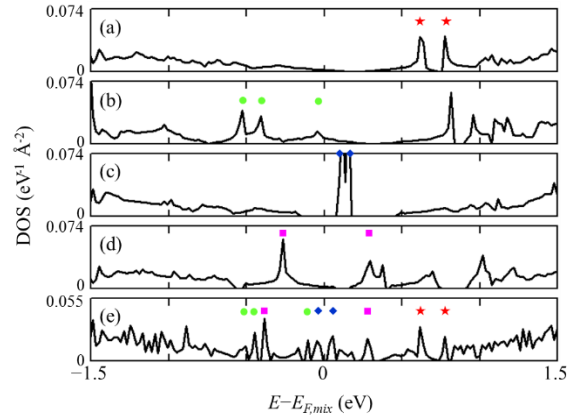
Figure 3.13 Comparison of the density of states (DOS) of (a) SW, (b) V_2(555-777), (c) I_2(555-6-777), (d) I_2(5555-66-7777), and (e) SW/V_2(555-777)/I_2(555-6-777)/I_2(5555-66-7777) graphene sheets shifted relative to the E_F of the mixed defect case. The symbols show the positions of resonant defect states.
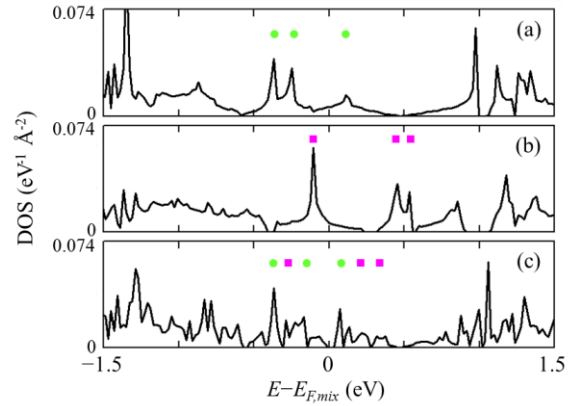
Figure 3.14 Comparison of the density of states (DOS) of (a) V_2(555-777), (b) I_2(5555-66-7777), and (c) V_2(555-777)/I_2(5555-66-7777) [3:1 ratio] graphene sheets shifted relative to the E_F of the mixed defect case. The symbols show the positions of resonant defect states.

38

3.8 CONCLUSIONS

We have investigated the impact of topological defects on the electronic structure and quantum capacitance of graphene using density functional theory. In this study, we considered small point-like defects such as Stone-Wales, di-vacancies, and di-interstitials. The presence of these defects disrupts the π system of graphene, which gives rise to quasi-localized states of varying degrees near the Fermi level. As a result, each of these defective graphene electrodes tends to have enhanced quantum capacitance compared to pristine graphene. Interestingly, their charging behavior is found to be asymmetric around the neutrality point such that some defective graphene sheets are more effective as either the positive or negative electrode. Our analysis also suggests that the double layer capacitance remains virtually unaffected by the presence of these defects. These findings indicate that graphene electrodes with topological defects may be used to enhance the overall capacitance of supercapacitors by virtue of the increased quantum capacitance. Furthermore, our study suggests that graphene-based electrodes can be specifically tailored as separate positive and negative electrodes, which could significantly enhance the performance of supercapacitors and warrants further study.

Chapter 4: Transition Metal Dopant-Vacancy Complexes

4.1 INTRODUCTION TO TRANSITION METAL DOPANTS

Chemical doping is a widely used technique to modify and tailor the electronic structure of graphene.[90,91] Nitrogen-doping of graphene, for example, has been explored for a variety of applications, including high-sensitivity sensors[92], catalysis[93], and supercapacitors[94,95]. One of the practical challenges of doping is the ability to control the concentration and selectivity of desired dopant types. Recent theoretical[96-98] and experimental[93,99,100] work has shown that transition metal (M) atoms can be selectively bound to vacancy (V) defects along the graphene lattice. Using this approach, it may be possible to tailor the dispersion of M-V complexes to atomic precision. In addition, unlike traditional nitrogen dopants, M dopants include d orbitals which can hybridize with C $2p$ orbitals. To date, however, the relative influence of M-V complexes on both C_Q and C_D, and therefore C_T, remains largely unexplored.

In this chapter, the influence of metal incorporation into graphene vacancies on C_T is investigated based on a model system of M-V graphene complexes in [BMIM][PF$_6$] IL using a combined classical molecular dynamics (MD) and density functional theory (DFT) approach. The impact of M-V complexes on C_Q and C_D is of particular interest. Using DFT, the electronic structure and C_Q of $3d$ M atoms bound to mono- and di-vacancy sites in

graphene are studied. MD simulations are then employed to investigate the microstructure and C_D at the electrode-electrolyte interface. Based on the relative contributions of C_Q and C_D to C_T, the potential benefit of M-V complexes in graphene for enhanced supercapacitor performance is discussed.

4.2 COMPUTATIONAL METHODS
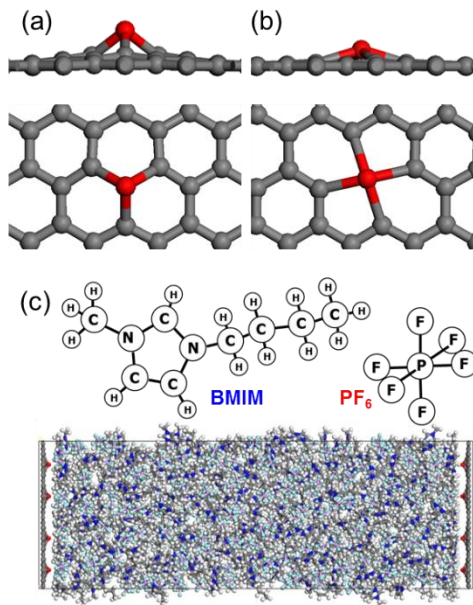
Figure 4.1   Top- and side-view schematics of a metal atom bound to the (a) mono-vacancy and (b) di-vacancy site, as well as schematics for (c) BMIM, PF_6, and the simulation box. White, blue and gray balls indicate H, N, and C atoms in BMIM while pink and cyan balls indicate P and F atoms in PF_6. Red and gray balls represent the metal and C atoms of the electrode.

The atomic and electronic structures of each M-V complex were calculated using DFT within the Perdew-Berke-Ernzerhof generalized gradient approximation[43] (GGA-PBE), as implemented in the Vienna Ab initio Simulation Package[42] (VASP). The projector

augmented wave (PAW) method[69] is used to describe the interaction between core and valence electrons based on a planewave basis set with a kinetic energy cutoff of 400 eV. The pristine and M-doped graphene sheets were modeled using a 5×5 hexagonal supercell with the GGA-optimized lattice constant of 2.466 Å (which is slightly larger than the experimental value of 2.461 Å); each supercell had one metal atom and 49 (48) C atoms in the M-MV (M-DV) cases, corresponding to a defect density of 7.6×10^{13} cm^{-2}. Periodic boundary conditions were employed in all three directions with a vacuum gap of 10 Å in the vertical direction to separate the graphene system from its periodic images. For the Brillouin zone integration, a (12×12×1) Monkhorst-Pack (MP) k-point mesh[70] was used for geometry optimization and energy calculations while a (15×15×1) MP k-point mesh was used to ensure convergence for electronic structure calculations. Metal-doping induced charge redistributions were determined using grid-based Bader analysis.[61]

The microstructure of [BMIM][PF$_6$] near selected electrodes and the electric potential profile were determined using MD simulations based on the OPLS-AA force field[50,101] when $\sigma = 0$, ±2.38, ±4.75, and ±9.50 µC/cm^2. The Lennard-Jones parameters for Ti and Ni were adopted from previous work by Heinz and co-workers[102] and Minonishi and co-workers[103]; details on other force field parameters can be found in Ref. 13. As illustrated in Figure 4.1, the simulation domain consists of 356 [BMIM][PF$_6$] IL pairs sandwiched between two electrodes (34.18×39.46 Å^2) separated by 100 Å in the z-direction with periodic boundary conditions in the x- and y-directions. Here, the structure and charge distribution of the electrodes were determined from DFT calculations (additional details are described later). Note that the domain is set to be large enough such

that the electrolyte maintains a bulk density of 1.33 g/cm^3, which is close to experimental values.[104] Each MD simulation was annealed and quenched initially at 1000 K for 1 ns followed by 1 ns at 300 K for two cycles, and then further equilibrated for 3 ns at 300 K using a timestep of 1 fs. Production runs were carried out for 4 ns with atomic positions recorded every 5 ps. All runs were in the NVT ensemble with the target temperature controlled by a Nose-Hoover thermostat[60] with a 100 fs damping parameter. All MD simulations were performed with the Large-scale Atomic/Molecular Massively Parallel Simulator (LAMMPS) program.[105] MD results reported herein were obtained from the average of five independent simulations with different initial atomic configurations.

4.3 GEOMETRY OF METAL DOPANT-VACANCY COMPLEXES
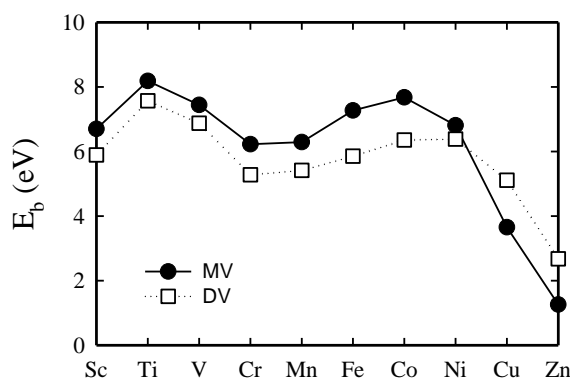
Figure 4.2   Binding energies (E$_b$) for each transition metal atom bound to a mono- (MV) and di- (DV) vacancy site on graphene.

In this work, we investigate transition metals bound to two different graphene defect sites with a defect density (n_d) of 7.6×10^{13} cm^{-2}, as illustrated in Figure 1. To the

left, a single metal (M) atom is bound to a mono-vacancy (MV) site of graphene, which

hereafter will be referred to as the M-MV complex; the M is bonded to the three nearest C

atoms while also tending to lie out-of-plane. On the right, the M is bound to a di-vacancy

(DV) site, which we call the M-DV complex; the M is now coordinated to the four nearest

C atoms. While each of the M-C bond lengths for the M-DV complexes are larger than that

of the M-MV complex, the M elevation is also smaller. In fact, Ni, Cu and Zn tend to be

planar with the graphene lattice. All binding energies and details of the geometry (bond

length and M elevation) can be found in Figure 4.2 and 4.3, respectively. In addition, the

calculated magnetic moments were found to be in good agreement with previous

studies.[97,98]
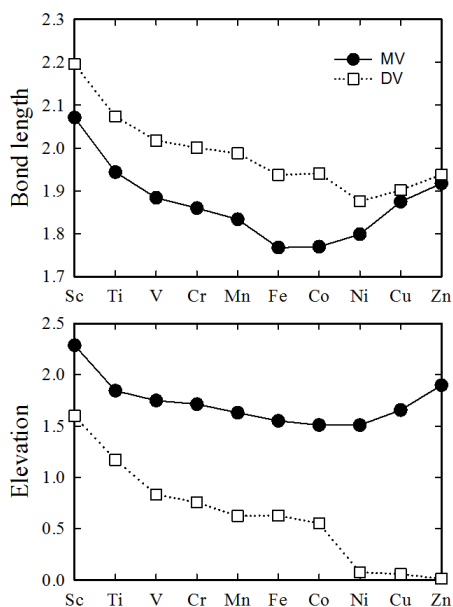
Figure 4.3   Bond lengths (in Å) and elevations (in Å) of each metal atom relative to
adjacent C atoms in the mono- (MV) and di- (DV) vacancy cases.

4.4 HYBRIDIZATION BETWEEN METAL DOPANT AND GRAPHENE VACANCY STATES
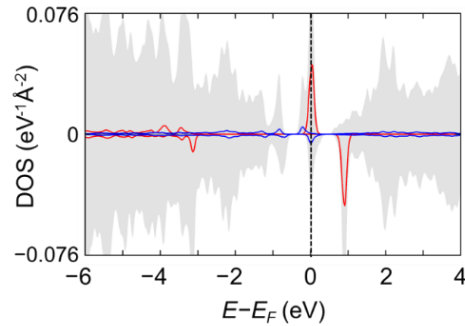
Figure 4.4   Total density of states (shaded) and the projected $2sp^2$ (red) and $2p_z$ (blue) orbitals of the under-coordinated C atoms at the mono-vacancy site. Positive (negative) values refer to the spin-majority (-minority) case. The Fermi level is indicated by the dashed line.
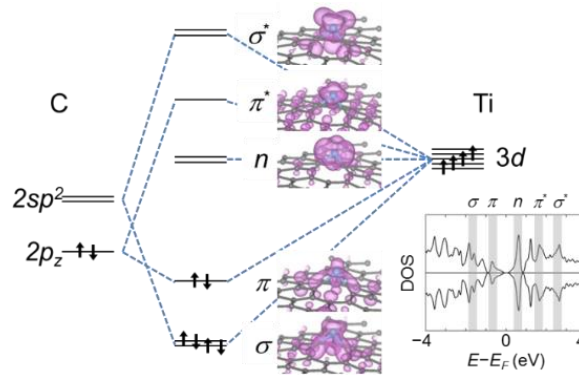
Figure 4.5   Schematic of the hybridization between the $3d$ orbitals of Ti and the $2sp^2$ and $2p_z$ orbitals of the C atoms at the mono-vacancy site, showing direct- (σ), indirect- (π), and non- (n) bonding states. The depicted band-decomposed charge density isosurfaces (isosurface values of 0.005 e/bohr^3 for σ, n, σ^* and 0.002 e/bohr^3 for π and π^*) were calculated from the shaded regions shown in the total density of states (DOS) (lower right).

The presence of M impurities and/or C vacancies can affect the electronic structure of graphene. But before analyzing the M-V complexes, we first examine the electronic density of states (DOS) of the unreconstructed MV defect; note that the unreconstructed MV defect has D_{3h} symmetry, unlike the fully relaxed MV defect which has C_{2v}

45

symmetry.[74] As shown in Figure 4.4, near the Fermi level (E_F), we observe the existence of both sp^2 dangling bond and p_z states arising from the three under-coordinated C atoms; here, the p_z peak appears to be 1 eV below the sp^2 peak (which is doubly degenerate). Having identified these quasi-localized p_z and sp^2 states around the vacancy site, we now explore their hybridization with the M $3d$ states.
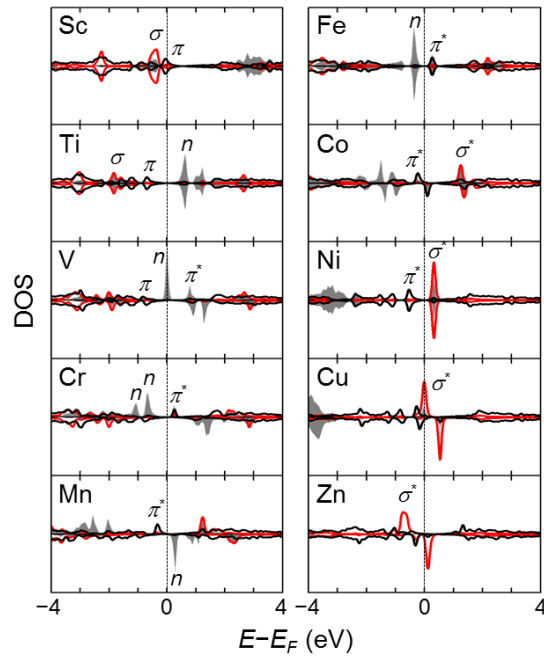
Figure 4.6   Spin-polarized density of states (DOS) projected onto the metal $3d$ orbitals (shaded) and $2sp^2$ (red) and $2p_z$ (black) orbitals of the C atoms at the mono-vacancy site; positive (negative) values refer to the spin-majority (-minority) state. The $2sp^2$ and $2p_z$ curves have been amplified by a factor of 2 and 5, respectively, for emphasis. The dashed line indicates the position of the Fermi level. The peaks near the Fermi level have been labeled to indicate the corresponding metal-carbon hybridization, as described in the text.

Figure 4.5 depicts a molecular orbital model[98] near E_F for the Ti case which serves as an example for the M-MV complexes; note that the M-C interaction is dictated by the orbital overlap between C $2sp^2$ and $2p_z$ and M $3d$ states, while the emptied M $3s$ states are

46

found well above E_F.[98] The overlap between the C sp^2 and out-of-plane M d_{xz} and d_{yz} orbitals can result in σ-σ^* states as shown in the band-decomposed charge density isosurfaces; this is possible since the M atom is elevated with respect to the graphene lattice. In addition, π-π^* states arise from the hybridization of C p_z and M d_{z^2} orbitals, as also seen from the band-decomposed charge density isosurfaces; the $\pi(\pi^*)$ state is expected to have a majority fraction of p_z (d_{z^2}) character. The in-plane d_{xy} and $d_{x^2-y^2}$ orbitals, which are elevated with respect to the graphene lattice, remain largely non-bonding.

Figure 4.6 shows the PDOS of the M d and the three neighboring C sp^2 and p_z orbitals for each M-MV complex. We find that the predicted relative positions of the PDOS peaks are in good agreement with the model shown in Figure 4.5; as the number of valence d electrons increases from the Sc to Zn cases, the previously identified M-C states are progressively filled. As an example, consider the Sc and Ti cases which have occupied σ and π states within $-1 < E-E_F < 0.5$ eV and $-2 < E-E_F < -1$ eV, respectively. In the former case, the π state is partially filled (with zero magnetic moment), which suggests that Sc tends to accept an electron from the π system of graphene. In addition when compared to the Sc case, the Ti case exhibits increased hybridization between the sp^2 and d_{xz} and d_{yz} orbitals, as suggested by the broadened features of the corresponding peak (indicated by σ) located around $-2 < E-E_F < -1.5$ eV; this is consistent with the fact that Ti has the larger binding energy [Figure 4.2]. The non-bonding states are occupied next as demonstrated by the V, Cr, Mn, and Fe cases; these states are indicated by the sharp d PDOS peaks, reflecting the localization of the d_{xy} and $d_{x^2-y^2}$ states, which tend to appear within $-1 <$

$E-E_F < 1$ eV. Note that in the V, Cr, and Mn cases, the spin-majority non-bonding and π^* states are filled sequentially since a high-spin configuration is favored. Subsequently, the π^* and σ^* states are successively filled in the Co, Ni, Cu, and Zn cases, which is also well demonstrated by the decreased binding affinity of Cu and Zn compared to the other M atoms [Figure 4.3].
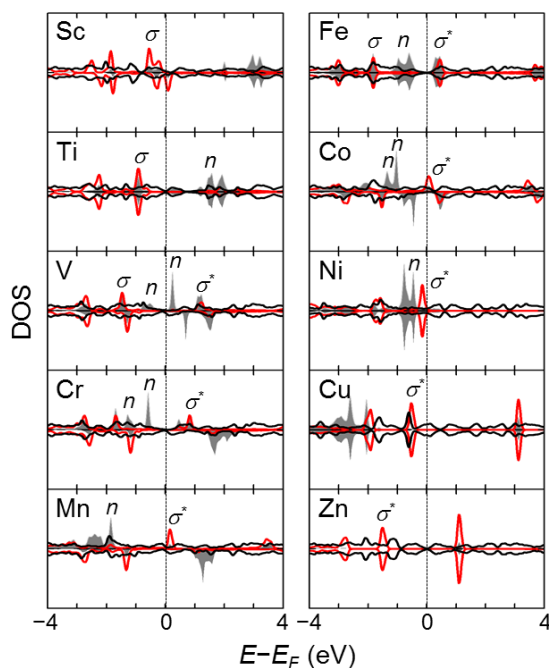
Figure 4.7   Spin-polarized density of states (DOS) projected onto the metal $3d$ orbitals (shaded) and $2sp^2$ (red) and $2p_z$ (black) orbitals of the C atoms at the di-vacancy site; positive (negative) values refer to the spin-majority (-minority) state. The $2sp^2$ and $2p_z$ curves have been amplified by a factor of 2 and 5, respectively, for emphasis. The dashed line indicates the position of the Fermi level. The peaks near the Fermi level have been labeled to indicate the corresponding metal-carbon hybridization, as described in the text.

We next similarly analyze the electronic structure of the M-DV complexes; the PDOS plots for the M-DV cases are depicted in Figure 4.7. Here, the bonding nature of the M to the DV site differs from that of the MV site in several distinct ways. First, the C sp^2

orbitals and in-plane M $d_{x^2-y^2}$ orbitals overlap to form σ-σ^* states, as demonstrated by the band-decomposed charge density isosurfaces [Figure 4.8]; the $d_{x^2-y^2}$ orbitals tend to hybridize with the out-of-plane d_{xz} and d_{yz} orbitals. Note that in the Sc case, the σ state is partially filled (with magnetic moment 0.4 μ_B), which suggests that Sc accepts an electron from the π system of graphene (yet to a lesser extent than in the M-MV case). The second major difference is the absence of π-π^* states (between C p_z and M d_{z^2}) due to the extended separation between M and C atoms [Figure 4.2]. As a result, the M d_{z^2} and d_{xy} orbitals remain non-bonding (as seen in the band-decomposed charge density isosurfaces in Figure 4.8) and appear as sharp d PDOS peaks within $-1 < E-E_F < 1$ eV in the V through Ni cases; here we should note that particularly in the Mn case, the calculation may require further refinement since conventional DFT is well-known to underestimate the electron localization.[106] In addition, the PDOS of p_z tends to be broadened within the depicted window, suggesting that the p_z orbitals remain well-coupled to the extended π system. The final distinction is observed in the Cu and Zn cases in which the π^* states are filled; note that the binding energy of Cu and Zn in the DV case is predicted to be larger than that of the MV case [Figure 4.3].

From the band-decomposed charge density isosurfaces, we also observe that the aforementioned M-C hybrid states can be partially coupled to the extended π system of graphene. Therefore, we can expect the majority fraction of injected charge carriers to spread over the graphene lattice with some accumulation near the M atom. In addition, upon binding to the vacancy site, we also expect charge to be transferred from the M atom

to graphene, which we can quantify using Bader analysis[61] (shown later); in the next

section, we explore the impact of this charge redistribution on how these M-V complexes

interact with [BMIM][PF$_6$] IL at the electrode-electrolyte interface.
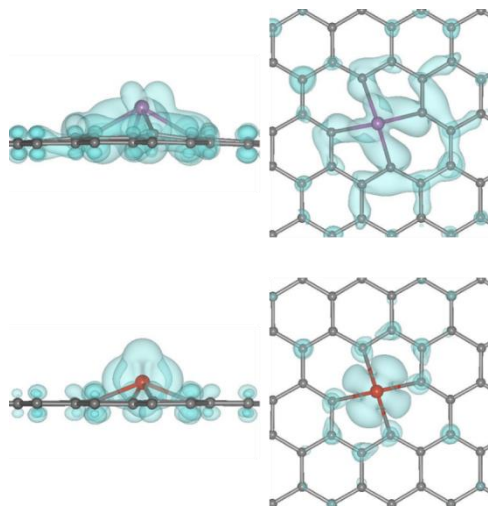
Figure 4.8   Band-decomposed charge density isosurfaces (0.003 e/bohr^3) for metal atoms
bound to the di-vacancy (DV) site of graphene. The upper panels depict side-
and top-views of the Sc-DV case from $-0.5 < E\text{-}E_F < 0$ eV, showing the
directional bonds between C sp^2 and Sc $d_{x^2-y^2}$, d_{xz}, and d_{yz} orbitals. The lower
panels depict side- and top-views of the V-DV case from $0 < E\text{-}E_F < 0.5$ eV,
showing the non-bonding d_z^2 and d_{xy} orbitals.

4.5 METAL-INDUCED ENHANCEMENT OF THE QUANTUM CAPACITANCE

In order to analyze the charging behavior of the electrode, we next compute the

excess surface charge density (σ) as a function of ϕ_G in Figure 4.9 and compare it to that

of pristine graphene; note that $\sigma = \int_0^{\phi_G} C_Q d\phi$. From Figure 4.9, it is abundantly clear that

each of the M-MV and M-DV complexes store significantly more charge than pristine

graphene [shaded] within a 2 V window. Note that in several M-MV cases (most notably

in the Sc case but also in the V, Cr, and Mn cases), σ profile exhibits plateaus due to the lack of available electron states. In comparison, the monotonic increase in the σ profiles for the M-DV cases remains quite agnostic of metal dopant type. These plateau-like features are consistent with the fact that the impurity states tend to be more localized in the M-MV cases.
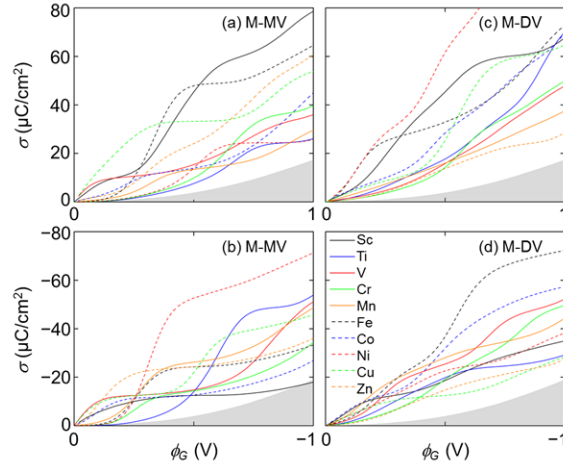
Figure 4.9　Excess electrode charge density (σ) as a function of local electrode potential (ϕ_G) for graphene with a metal atom bound to a mono-vacancy (M-MV) [(a)-(b)] and di-vacancy (M-DV) [(c)-(d)] site. The upper (lower) panels refer to the cathode (anode). The shaded region represents pristine graphene.

4.6 METAL DOPANT EFFECT ON THE DOUBLE LAYER STRUCTURE AND CAPACITANCE

We next investigate the impact of the M-MV and M-DV graphene electrodes with $n_d = 7.6 \times 10^{13}$ cm^{-2} immersed in [BMIM][PF$_6$] IL on the electric double layer (EDL) microstructure and subsequently, the (integral) EDL capacitance (C_D). Specifically, we use MD simulations to examine how the doping-induced charge redistribution and the elevation of the M atom influence the EDL. We have chosen to study Ti-MV, Ti-DV, Ni-

51

MV, and Ni-DV complexes in order to study a wide range of M atom elevations and partial charges; for example, the elevation of the M atom in Ni-MV and Ni-DV complexes varies by 1.35 Å (with similar partial charges) and the partial charge of the M atom in the Ti-DV and Ni-MV cases varies by around 1 e (with similar elevation). Table 4.1 summarizes the elevation and partial charge of the M atom used in the MD simulations for each M-V complex when neutral; note that a rectangular cell was used in these calculations
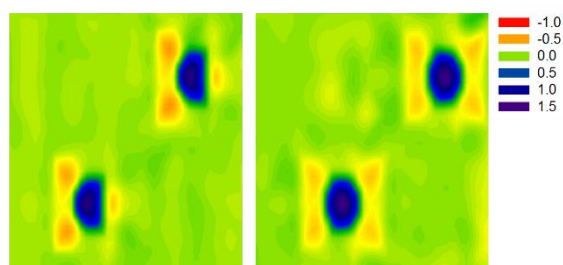
Figure 4.10   Color maps of the electrode charge redistributions for the Ti-MV (left) and Ti-DV (right) cases as calculated from grid-based Bader analysis.

Table 4.1   Summary of the metal atom elevation and partial charge at varying σ ($\mu C/cm^2$) calculated from density functional theory and used in the classical molecular dynamics simulations.

	Elevation	Partial Charge ($\sigma = 0$)	Partial Charge ($\sigma = -4.7$)	Partial Charge ($\sigma = +4.7$)
	Å	e	e	e
Ti-MV	1.8	1.37	1.33	1.39
Ti-DV	1.0	1.52	1.49	1.54
Ni-MV	1.35	0.50	0.47	0.53
Ni-DV	0.0	0.63	0.62	0.65

A. Near Uncharged Electrodes
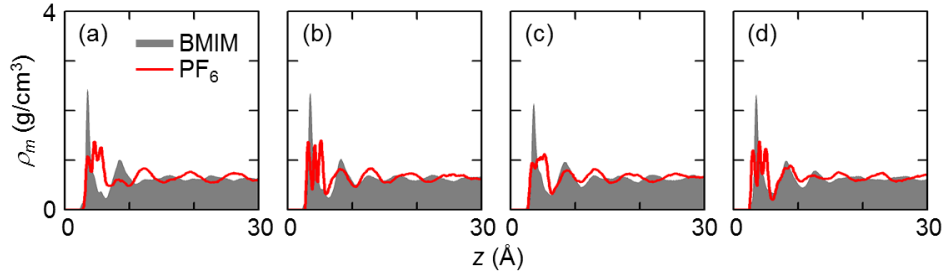
Figure 4.11 Mass density (ρ_m) profiles for BMIM and PF$_6$ as a function of distance from the electrode (z) for the (a) Ti-MV, (b)Ti-DV, (c) Ni-MV, and (d) Ni-DV cases when $\sigma = 0$ µC/cm^2.

In Figure 4.11(a)-(d), we compare the mass density (ρ_m) profiles of BMIM and PF$_6$ near (a) Ti-MV, (b) Ti-DV, (c) Ni-MV, and (d) Ni-DV graphene electrodes as a function of distance from the electrode (z). All four cases exhibit oscillatory profiles that dampen away from the electrode, which is indicative of IL layering[14,15,85] and become bulk-like after 3 nm. In every case, the first BMIM peak is quite pronounced, which demonstrates that the BMIM ring and tail retain the well-known parallel alignment with the graphene sheet, similarly to the pristine graphene case.[13,14] However, the three PF$_6$ peaks in the first layer ($z \approx$ 3-5 Å) become noticeably less pronounced when the M atom elevation exceeds 1 Å, indicating that the PF$_6$ ions lose the well-known distinct orientation of parallel planes of F, P, and F atoms observed near planar electrodes.[13] For both PF$_6$ and BMIM, the preferential orientation of the first IL layer near pristine graphene is due to the electrode-electrolyte van der Waals (vdW) interactions. The charge redistribution due to the M-V complexes, however, introduces electrostatic interactions which can dominate over vdW interactions. As a result, PF$_6$ ions are electrostatically attracted toward the electropositive

M atom; when the M atom is sufficiently elevated (> 1 Å), PF_6 also rotates to more efficiently screen the M atom, thereby losing its previous orientation. BMIM ions, on the other hand, remain flat due to a combination of vdW and electrostatic attraction to the slightly electronegative graphene lattice. To clarify this behavior, we depict a snapshot of the Ti-MV electrode with adjacent IL ions in Figure 4.12.
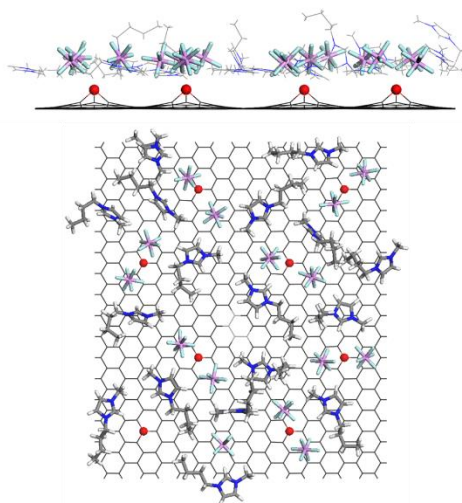
Figure 4.12 Side- and top-view snapshots of the first IL layer near neutral Ti-MV electrodes. The red balls and black lines represent Ti and graphene, respectively. The purple and cyan sticks represent PF_6 while the white, blue, and grey sticks represent BMIM.

In the case of pristine graphene, the number density of BMIM and PF_6 (and ρ_m given the similarity of their molecular weights) in each layer tends to be nearly equal in order to maintain charge neutrality.[13] This is also observed to be true in the Ni-DV case despite the large fluctuation of charge along the lattice (the partial charge of Ni is 0.63 e in this case) since Ni remains within the graphene plane. However, in the other three metal-doped cases, the spatial number density balance between BMIM and PF_6 is no longer maintained. For example, the second IL layer ($z \approx 9$ Å) exhibits an increasingly broadened

PF_6 peak as the displacement of the M atom increases while the BMIM peak remains nearly the same. This suggests that due to the presence of the M atoms, ions segregate within the EDL to varying degrees. We can quantify this behavior using χ (the mixing parameter) as a function of z:

$$\chi_i(z) = \frac{\int_0^z \frac{\rho_{m,i}(z')}{MW_i} dz'}{\int_0^z \sum_j \frac{\rho_{m,j}(z')}{MW_j} dz'} \tag{4.1}$$

where i refers to the ion species of interest, j refers to each ion species present, and MW is the molecular weight. In this case when $\chi_i = 0.5$, the cumulative number of ion i is perfectly balanced by the other ion species. Figure 4.13 depicts χ_{BMIM} for each case studied; around $2 < z < 5$ Å, it is evident that χ_{BMIM} increases as the elevation of the M atom increases, which is consistent with the aforementioned competition (synergism) of electrostatic and vdW interactions between the electrode and PF_6 (BMIM).
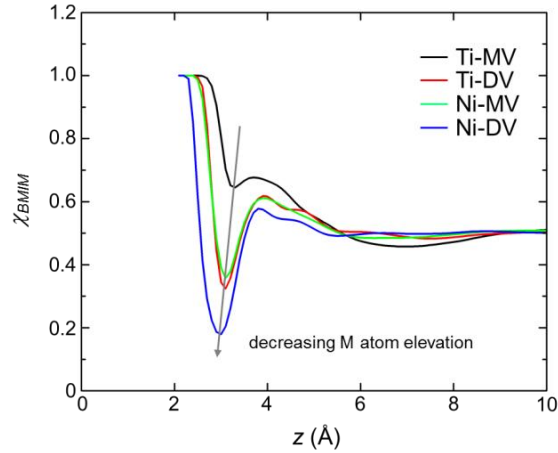
Figure 4.13 Mixing parameter (χ_{BMIM}) profiles for BMIM near uncharged electrodes as a function of distance from the electrode (z).
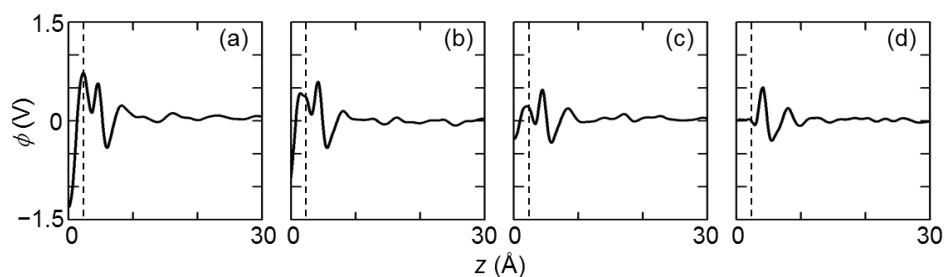
Figure 4.14 Potential (ϕ) profiles as a function of distance from the electrode (z) for the (a) Ti-MV, (b) Ti-DV, (c) Ni-MV, (d) Ni-DV cases when $\sigma = 0$ μC/cm². The dashed lines indicate the position of the vacuum-IL interface adjacent to the electrode.

From the distribution of electrode and IL atoms with fixed atomic charges, we can also compute the space charge variation and therefore, the spatial potential variation (ϕ) by solving Poisson's equation (see Chapter 2). In Figure 4.14, we show ϕ as a function of z for (a) Ti-MV, (b) Ti-DV, (c) Ni-MV, and (d) Ni-DV; the ϕ of the bulk electrolyte is taken as reference ($\phi = 0$ V). To interpret the ϕ profiles, it is helpful to separately examine their variation in the IL region and the near-electrode region between the electrode and first IL layer. First, we study how the microstructure of the IL ions affects ϕ close to the electrode ($2 < z < 5$ Å) as this is where discrepancies in the IL region between the different cases noticeably appear. In accordance with an increasing degree of BMIM segregation (Ni-DV $<$ Ti-DV $\approx$ Ni-MV $<$ Ti-MV cases), ϕ at the IL region interface ($z \approx 5$ Å) also increases; the accumulation of net positive charge close to the interface leads to a proportional increase in ϕ. Between the electrode and the IL region interface, however, ϕ rapidly drops if the M atom is elevated due to the local electric field generated from the charge redistribution within the electrode; the extent of the drop in ϕ therefore increases as either

the M atom elevation and/or the charge differential between the M atom and graphene

lattice increases. As a result of both of these factors, the surface potential relative to the

bulk potential, otherwise known as the potential of zero charge (ϕ_Z), varies as $0.01 > -0.31$

$> -0.89 > -1.35$ V for the Ni-DV > Ni-MV > Ti-DV > Ti-MV cases. We should note that

in the pristine graphene case, ϕ_Z is predicted to be essentially zero.[13,107]

B. Near Charged Electrodes
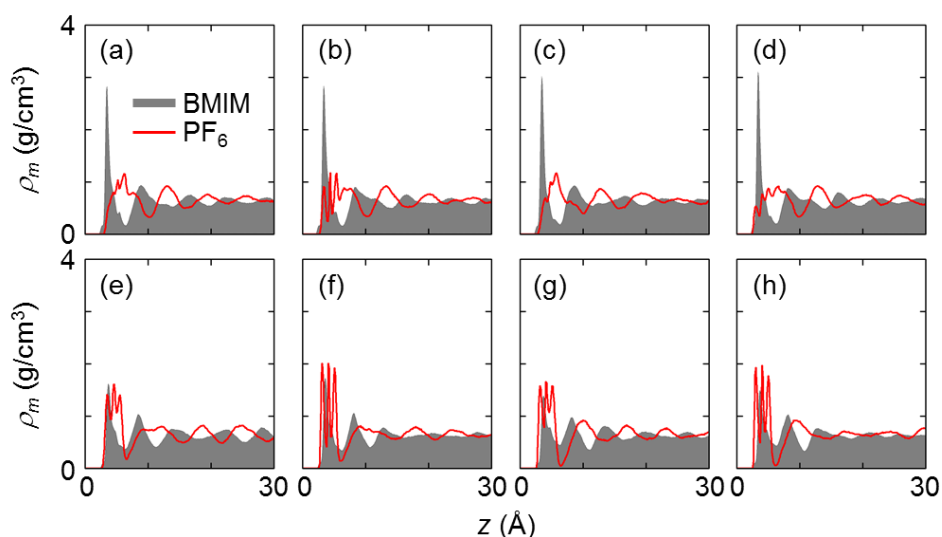
Figure 4.15   Mass density (ρ_m) profiles for BMIM and PF$_6$ as a function of distance from the electrode (z) for the (a) Ti-MV, (b) Ti-DV, (c) Ni-MV, and (d) Ni-DV cases when $\sigma = -4.75$ µC/cm^2 and for the (e) Ti-MV, (f) Ti-DV, (g) Ni-MV, (h) Ni-DV cases when $\sigma = 4.75$ µC/cm^2.

Figure 4.15 shows the ρ_m profiles for BMIM and PF$_6$ for the Ti-MV, Ti-DV, Ni-

MV, and Ni-DV cases, respectively when $\sigma = -4.75$ µC/cm^2 (a)-(d) and $\sigma = 4.75$ µC/cm^2

(e)-(h). Near each charged electrode, the ρ_m profiles exhibit alternating counterion/coion

layering that dampens away from the electrode and extends around 3 nm before showing bulk-like characteristics; this layering behavior is consistent with previous experimental studies near charged surfaces.[108-110] Near the negative electrode, the first BMIM peak tends to be very pronounced, indicating the well-known preference for the positively charged BMIM rings to align parallel to the electronegative graphene lattice due to electrostatic attraction.[13,15] At the same time, the presence of PF_6 is shifted away from the electrode and loses its preferential orientation due to electrostatic repulsion; note that the PF_6 profile retains those initial three peaks in the Ti-DV case which suggests the preservation of some order. Near the positive electrode, the three PF_6 peaks in the first layer (representing F, P, and F atoms, respectively) are also pronounced. Yet similarly to when the electrodes are neutral, the rigidity of the PF_6 orientation is diminished when the M atom elevation exceeds 1 Å.
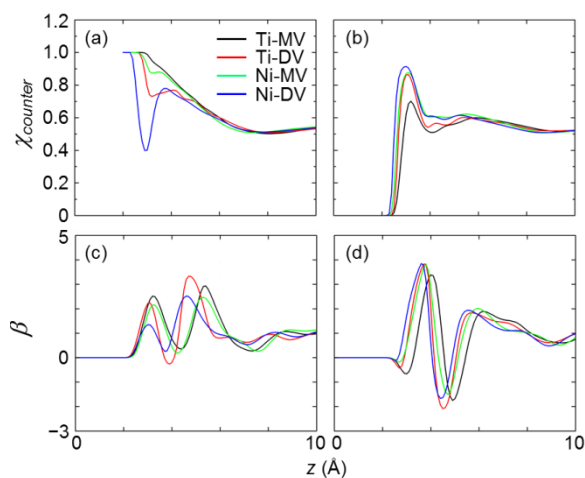
Figure 4.16 Mixing parameter ($\chi_{counter}$) profiles for the counterion and screening parameter (β) profiles as a function of distance from the electrode (z) when $\sigma = -4.75$ µC/cm^2 [(a),(c)] and $\sigma = 4.75$ µC/cm^2 [(b),(d)].

58

To further clarify the nature of the microstructure, we calculate χ for the counterion near each electrode, as shown in Figure 4.16(a)-(b). Near the negative electrode, it is apparent that the degree of BMIM segregation decreases directly with the M atom elevation. In contrast, the degree of PF_6 segregation increases inversely with the M atom elevation. Both of these observations are consistent with the previously described interaction of the M atom with PF_6 and BMIM, which is predominately electrostatic in nature.

By affecting the ion segregation near the electrode, the M-V complexes also alter the screening efficiency which can be quantified with β (the screening parameter) as a function of z:

$$\beta = -\frac{\int_0^z \rho_q(z')dz'}{\sigma} \tag{4.2}$$

where $\beta = 1$ indicates perfect screening of the electrode charge. Our results, shown in Figure 4.16(c)-(d), show that the IL ions in the first layer overscreen the near-surface electric field, which is typical at small voltages.[111] Here, the impact of ion segregation on the IL screening becomes immediately obvious – the increased counterion segregation expectedly increases the overscreening as demonstrated by the comparative intensities of the first β peaks. Also note that the location of the β peaks shifts away from the electrode in accordance with the M atom elevation, further supporting the ion segregation behavior.

Figure 4.17 shows the predicted variation in ϕ near the negative [(a)-(d)] and positive [(e)-(h)] electrodes for each defect case. Near the negative (positive) electrode, the overall increase (decrease) in ϕ in the IL region ($2 < z < 5$ Å) becomes greater in proportion

to the degree of counterion segregation (or by analogy, the extent of overscreening). From the IL region interface to the electrode surface, ϕ expectedly drops (rises) near the negative (positive) electrode due to the applied electric field. Here, ϕ is further influenced if the M atom is elevated due to the local electric field generated from the charge redistribution of the electrode. As the M atom elevation and/or partial charge increases, the drop (rise) in ϕ is enhanced (mitigated) near the negative (positive) electrode.
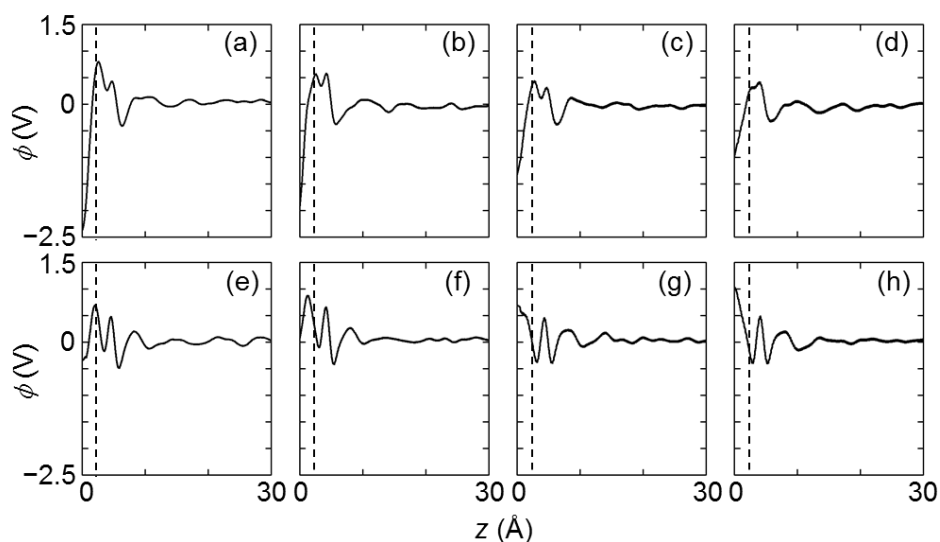
Figure 4.17   Potential (ϕ) profiles as a function of distance from the electrode (z) when the $\sigma = -4.75 \ \mu C/cm^2$ for (a) Ti-MV, (b) Ti-DV, (c) Ni-MV, and (d) Ni-DV and when $\sigma = 4.75 \ \mu C/cm^2$ for (e) Ti-MV, (f) Ti-DV, (g) Ni-MV, and (h) Ni-DV. The dashed line indicates the position of the vacuum-IL interface adjacent to the electrode.

From the predicted electrode surface potentials relative to the bulk potential (ϕ_D), we calculate the overall change in potential as the difference between ϕ_D and ϕ_Z. We can therefore evaluate the (integral) double layer capacitances $C_D = \sigma/(\phi_D - \phi_Z)$, which we extend to include $\sigma = \pm 2.38$ and $\pm 9.5 \ \mu C/cm^2$, and compare them in Figure 4.18. Although ϕ_Z

widely varies, it is evident that the variation in C_D (and ϕ_D-ϕ_Z) is only as much as 20%; this suggests that the observed perturbations to the microstructure due to differences in M atom elevation and partial charge only weakly influence C_D. Furthermore, our results indicate that the presence of these M-V complexes consistently enhances C_D near the cathode (by as much as 20%) when compared to the pristine graphene case with $\sigma = 4.75$ (-4.75) μC/cm^2 (extrapolated from Ref. 13). However, near the anode, the C_D of the metal-doped cases tend to fluctuate around that of pristine graphene.
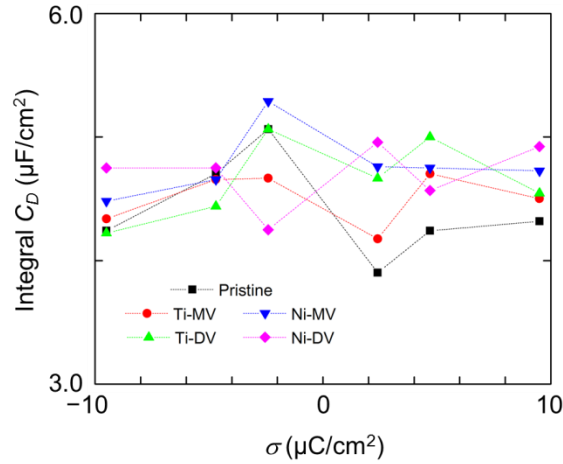
Figure 4.18 Integral double layer capacitance (C_D) as a function of excess surface charge density (σ) for Ti-MV, Ti-DV, Ni-MV, Ni-DV and pristine graphene cases. Results for pristine graphene were extrapolated from Ref. 13. The dashed lines are to guide the reader's eye.

4.7 METAL DOPING EFFECT ON THE TOTAL INTERFACIAL CAPACITANCE

We estimate the total interfacial capacitance (C_T) as a function of applied potential ($\phi_a = \phi_G + \phi_D - \phi_Z$) when $\sigma = \pm 2.38$, ± 4.75, and ± 9.50 μC/cm^2 based on the series

capacitance of C_D and C_Q, *i.e.* $1/C_T = 1/C_D + 1/C_Q$; note that the integral $C_Q (= \sigma/\phi_G)$ is used here. As seen in Figure 4.19, the C_T of the metal-doped cases are predicted to consistently outperform that of pristine graphene at both the anode and cathode; the Ni-DV case is particularly noteworthy with an enhancement of around 1−2 µF/cm² within ±1 V. We can attribute this improvement to the increased C_Q of the M-V complexes studied (the integral C_Q tend to vary significantly between 8 and 92 µF/cm²) since the influence of metal-doping on C_D is marginal. These results suggest that metal-doping can be an effective strategy to mitigate the C_Q limitation of sp^2-bonded carbon electrodes, thereby allowing further improvements in C_D (whether through structural or other modifications) to manifest in the overall performance of supercapacitors.
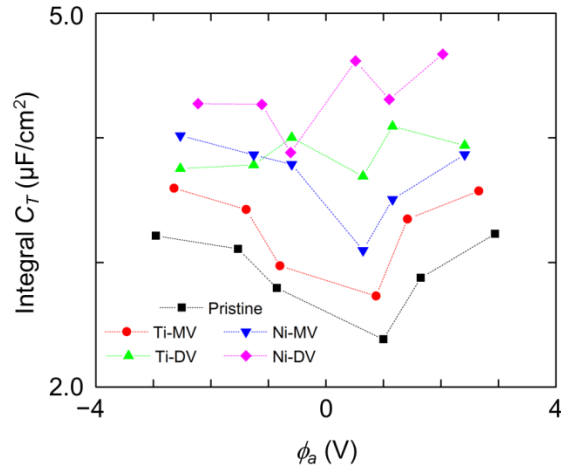
Figure 4.19 Predicted total interfacial capacitance (C_T) values for each metal-doped graphene case as a function of applied potential (ϕ_a). For reference, the C_T of pristine graphene in [BMIM][PF₆] IL is also included. The dashed line is to guide the reader's eye.

We should point out that our quantitative prediction for C_T is based on several assumptions; the following factors should be considered in future investigations to improve

accuracy. For instance, we have ignored the possible polarization at the electrode-electrolyte interface, which can affect the electrode charge redistribution, the EDL microstructure, and ultimately, C_D (which is likely underestimated).[87,88] In addition, we recognize that conventional DFT can introduce self-interaction errors; the resultant erroneous description of charge localization can be mitigated using hybrid functional methods.[112] We also omit the possible influence of IL interactions with the electrode on its electronic structure, which may alter C_Q to a certain extent. Nonetheless, our study clearly shows that the inclusion of M impurities in sp^2-bonded carbon nanomaterials can significantly enhance EDLC performance primarily by dramatically improving C_Q.

4.8 CONCLUSIONS

We examined the influence of metal-doped graphene in [BMIM][PF$_6$] ionic liquid on the electrode and electric double layer (EDL) capacitances using a combination of DFT and classical MD simulations. We considered $3d$ transition metals (M) bound to mono- (MV) and di- (DV) vacancy sites in graphene. Our electronic structure analysis demonstrated that the introduction of these M-V complexes induces quasi-localized states. From the predicted electronic density of states, we evaluated the quantum capacitance (C_Q) of each M-doped electrode and compared them to pristine graphene. Due to the augmented availability of states, the charge storage capacities of each M-doped electrode were generally found to exceed that of pristine graphene, and in some cases, by as much as 500% (at a local potential of 1 V). We also studied the influence of these M-V complexes on the

EDL microstructure using a few selected cases as model systems. We found that the microstructure can be perturbed; in particular, PF_6 (BMIM) ions can accumulate near (spread away from) the M atom. When the electrodes are charged, counterion segregation becomes more (less) apparent near the cathode (anode) as the M atom elevation increases. Despite these perturbations to the EDL, the estimated double layer capacitance (C_D) was found to be mostly within 20% of the pristine graphene case (while the potential of zero charge was predicted to vary on the order of 1 V depending on the type of M-V complex). Based on C_Q and C_D, we evaluated the total interfacial capacitances ($C_T = [1/C_D + 1/C_Q]^{-1}$) and found that the M-doped cases were consistently enhanced by as much as 125% (within ± 1 V) when compared to pristine graphene. Our study clearly demonstrates that M-doping of graphene-like electrodes can effectively mitigate the C_Q limitation, thereby significantly enhancing EDLC performance.

Chapter 5: Extended Edge Defects

Work in this chapter was published and reprinted with permission from J. Phys. Chem. C, Vol. 118, A. J. Pak, E. Paek, and G. S. Hwang, Impact of Graphene Edges on Enhancing the Performance of Electrochemical Double Layer Capacitors, pg. 21770−7. Copyright (2014) American Chemical Society.

5.1 INTRODUCTION TO EDGE DEFECTS IN GRAPHENE

Up to this point, the scope of this dissertation has been limited to phenomena near the basal plane of graphene where ion accumulation mostly occurs. But given the revealed sensitivity of C_T to C_Q and C_D, it would be valuable to explore similar phenomena near the edges of graphene for several reasons. First, it is well-known that the presence of edges can alter the electronic structure of graphene, which has been successfully utilized in many electrochemical applications.[113-115] Such modifications to the electronic structure may subsequently affect C_Q. It is also possible that the electric double layer (EDL) microstructure, and therefore C_D, can be noticeably perturbed near the edge sites, similarly to the case of prismatic graphite electrodes with different degrees of corrugation.[86] Furthermore, research into potential applications for graphene edges seems timely given recent advances in the fabrication of high-quality graphene edges.[116] One example of this is a recent demonstration by Zhang and coworkers in which the splitting of vertically aligned carbon nanotubes into graphene nanoribbons exhibited a four-fold increase in specific capacitance.[117] However to the best of our knowledge, a fundamental study on the impact of edge defects on both C_Q and C_D has never been reported.

In this chapter, the effect of edge defects on C_T is investigated using edge-passivated graphene nanoribbons (GNRs) as model systems; only zigzag GNRs (ZGNRs) are considered since they can be metallic while armchair GNRs are neglected as they are always semiconducting. The relative impacts of these edge defects on C_Q and C_D are studied using a first principles-based computational approach. First, density functional theory (DFT) is employed to study the electronic structure and C_Q of two types of edge-passivated ZGNRs at varying widths. Using classical molecular dynamics (MD), the microstructure and C_D of a ZGNR immersed in [BMIM][PF$_6$] ionic liquid is investigated. Finally, the potential benefit of edge defects with regard to the overall C_T is discussed.

5.2 COMPUTATIONAL METHODS

The atomic and electronic structures of each investigated ZGNR were calculated using DFT within the spin-polarized Perdew-Wang 91 generalized gradient approximation[68] (GGA-PW91), as implemented in the Vienna Ab initio Simulation Package[42] (VASP); the Vosko-Wilk-Nusair interpolation was used for the correlation part of the exchange correlation functional.[118] The projector augmented wave (PAW) method[69] was used to describe the interaction between ion core and valence electrons with a planewave basis set using a kinetic energy cutoff of 400 eV.

Two different types of edge-passivated ZGNRs at two different widths are initially investigated: (i) single hydrogen (H) termination (herein called H-18ZGNR and H-60ZGNR) and (ii) alternating termination by a hydroxyl (OH) and single H (herein called

OH-18ZGNR and OH-60ZGNR). The OH group is considered one of the most stable oxidation groups and is known to prefer a parallel orientation with respect to the plane of the GNR.[119,120] The ZGNRs were modeled using rectangular 2×9 (as shown in Figure 5.1) and 2×30 supercells (corresponding to 72 and 240 C atoms, respectively) with a GGA-optimized lattice constant of 2.466 Å. Periodic boundary conditions were employed in all three directions but vacuum spaces of 10 and 20 Å were included in the z and y directions, respectively, to remove interactions with adjacent images. For the Brillouin zone integration, a $(6 \times 1 \times 1)$ Monkhorst-Pack mesh[70] of k-points was used to determine the optimal geometries and total energies while an increased mesh size of $(14 \times 1 \times 1)$ was used for electronic structure calculations. To make comparisons to the pristine graphene case, similar electronic structure calculations were performed using a 4-atom rectangular cell with dimensions of 4.272×2.466 Å^2; here, a $(21 \times 21 \times 1)$ k-point mesh was used for Brillouin zone sampling.

To study the atomic charge distribution of ZGNRs at different widths, additional rectangular 2×5 and 2×13 supercells for both H-ZGNR and OH-ZGNR cases using the same lattice constant, vacuum spacing, and k-point mesh were modeled. The atomic charges were evaluated using grid-based Bader analysis[61] under neutral and charged (± 1 e per supercell) conditions; the latter case was used to study the excess charge redistribution. The calculated Bader charges for OH-18ZGNR were subsequently used in the MD calculations.

The microstructure of [BMIM][PF$_6$] near OH-18ZGNR electrodes was studied from MD simulations based on the OPLS-AA force field[50,101] using the Large-scale Atomic/Molecular Massively Parallel Simulator (LAMMPS) program[105]. As illustrated in Figure 5.1, the simulation consisted of 3036 pairs of [BMIM][PF$_6$] surrounding two electrodes (39.46 × 39.2 Å^2) separated by 100 Å in both the y and z directions, which was large enough such that the electrolyte maintained a bulk density in the regions between electrodes. The inter- and intra-molecular force field parameters for BMIM, PF$_6$ and graphitic C are described in Ref. 13. The generalized OPLS force field parameters for OH and H moieties were used.[101] During the simulations, the electrode atoms were fixed in position.
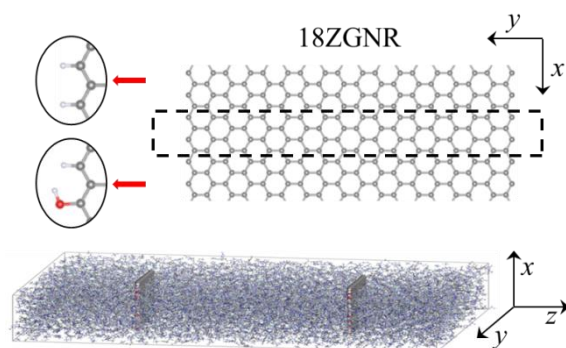
Figure 5.1   (Top) Schematic of the zigzag graphene nanoribbon supercell (bound by the dashed lines) used in electronic structure calculations. The edges were passivated by either H or H/OH atoms where H and O are indicated by the white and red balls, respectively. (Bottom) Schematic of the simulation box used in classical molecular dynamics simulations. The white, red, and grey balls indicate H, O, and C electrode atoms, respectively. The white, grey, and blue lines indicate the H, C, and N atoms in BMIM while the pink and cyan lines indicate the P and F atoms in PF$_6$. Periodic boundary conditions were applied in all three directions.

Electrodes with excess surface charge density $\sigma = 0$, 80.4 and -80.4 C g^{-1} were studied using the predicted atomic charges from Bader analysis. Each MD simulation were run initially at 1000 K for 1 ns followed by 1 ns at 300 K for three cycles to equilibrate the system using a timestep of 1 fs. Production runs were carried out for 2 ns with atomic positions recorded every 5 ps. All runs were in the NVT ensemble with the temperature controlled by a Nose-Hoover thermostat[60] with a 100 fs damping parameter. MD results reported herein were obtained from the average of five independent simulations with different initial atomic configurations. Further details about the MD simulations are described in Ref. 13.

5.3 GRAPHENE NANORIBBON ELECTRONIC STRUCTURE AND QUANTUM CAPACITANCE

In this section, we present the band structures and density of states (DOS) of the investigated ZGNRs, considering both the anti-ferromagnetic (AF) and ferromagnetic (FM) spin states. Based on the electronic structure, we then predict and analyze the quantum capacitance (C_Q) of the ZGNRs.

Figure 5.2(a) shows the DOS for H-18ZGNR [left] and H-60ZGNR [right] in the AF state (the insets show the FM state). According to our GGA-PW91 calculations for H-18ZGNR, the AF state is marginally more stable (≈ 0.6 meV Å^{-1}) than the FM state; other functionals including LDA (≈ 0.2 meV Å^{-1}) and GGA-PBE (≈ 1.0 meV Å^{-1}) predict similar results. In the AF case, a band gap of 0.3 eV is estimated to arise due to the differences in AF exchange interaction between sublattices.[120-122] In the FM case, the spin-majority and

spin–minority states are both partially filled at the Fermi level (E_F). However in the H-60ZGNR case, both the AF band gap (0.16 eV) and difference in energy between the AF and FM state ($\approx$ 0.0 meV Å^{-1}) is reduced, which is expected to occur as the GNR width increases.[121]
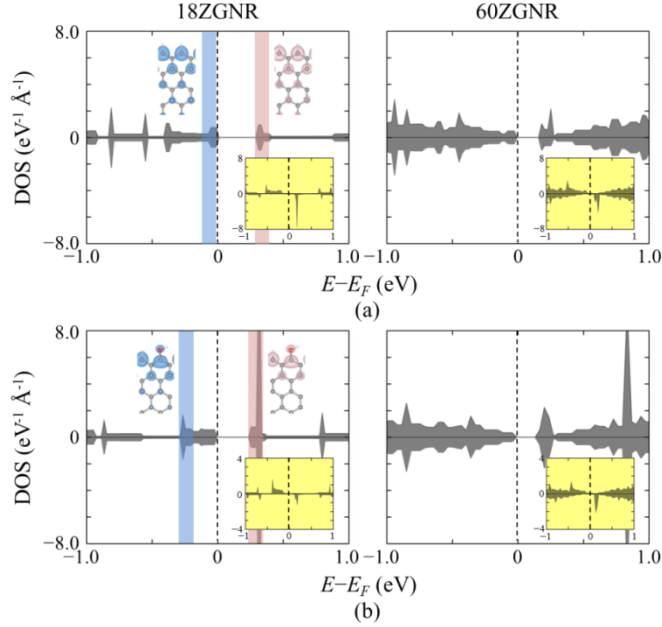
Figure 5.2   Spin-polarized total density of states (DOS) of (a) H-passivated and (b) alternating H-/OH-passivated zigzag graphene nanoribbons (ZGNR) at different widths in the anti-ferromagnetic state.   The insets depict the corresponding DOS of the ferromagnetic state. Positive (negative) values of the DOS indicate the spin-majority (-minority) states. The Fermi level (E_F) is marked by the dashed line.   The band-decomposed charge density isosurfaces (0.001 e bohr^{-3}) were obtained from the highlighted energy ranges.

In both the AF and FM cases, the DOS exhibits peaks close to E_F (such as in the highlighted regions). It is well-known that these are primarily attributed to the quasi-localized p_z states at the edge sites[119-122], which is also depicted by the band-decomposed charge density isosurfaces; H passivation removes the dangling sp^2 bonds that are

70

characteristic of bare ZGNRs while the disrupted π bonds remain. Furthermore, these peaks tend to be more broadened in the H-60ZGNR case, which suggests that the degree of coupling between the edge p_z states and the π network increases as the ZGNR width increases.
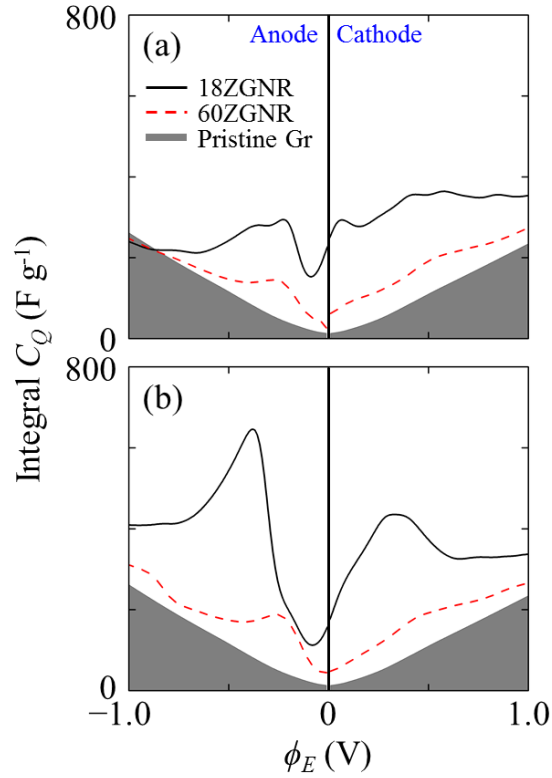
Figure 5.3   Integral quantum capacitances (C_Q) as a function of local electrode potential (ϕ_E) for the (a) H-passivated and (b) alternating H-/OH-passivated zigzag graphene nanoribbons (ZGNR) at different widths as compared to that of pristine graphene. The depicted C_Q of the ZGNR electrodes was computed from the average C_Q of the anti-ferromagnetic and ferromagnetic states. The middle line indicates the neutrality point.

Figure 5.2(b) shows the DOS for OH-18ZGNR [left] and OH-60ZGNR [right] in the AF state (the insets show the FM state). Similar to the H-18ZGNR case, the AF state of OH-18ZGNR is also marginally more stable (≈ 0.4 meV Å^{-1}) than the FM state, although

71

the addition of OH functional groups appears to reduce the spin order-induced stabilization. Consequently, the band gap in the AF state is reduced to 0.23 and 0.13 eV for OH-18ZGNR and OH-60ZGNR, respectively, while the FM state remains metallic. Comparing the OH-18ZGNR case to the H-18ZGNR case, we observe that in the former case, the DOS peaks within $-0.5 < E-E_F < 0.5$ eV are narrowed toward E_F; the quasi-localized C p_z orbitals tend to slightly overlap with the O $2p$ antibonding orbitals, as also seen in the band-decomposed charge density isosurfaces. However, the addition of OH in the 60ZGNR case does not noticeably affect the extent of localization, suggesting that the extent of coupling between the edge p_z states and π system is strong enough to be insensitive to the edge moieties when the ZGNR width is sufficiently large.

Using the procedure described in Chapter 2, we calculate the differential quantum capacitances ($C_{Q,diff} = \mathrm{d}\sigma/\mathrm{d}\phi_E$) for all four cases, where $\mathrm{d}\sigma$ and $\mathrm{d}\phi_E$ refer to the variations of excess surface charge density and local potential in the electrode, respectively. Since both the AF and FM states are likely to appear, the $C_{Q,diff}$ is computed from the average of the two cases. As shown in Figure 5.3, we then predict the integral C_Q (= σ/ϕ_E where $\sigma = \int C_{Q,diff} \mathrm{d}\phi_E$) which is the preferred metric to evaluate the total charge storage capability at a given ϕ_E. In comparison to the pristine graphene case, the C_Q of the ZGNRs tends to be increasingly enhanced as the ZGNR width decreases, which is especially apparent when $|\phi_E| < 0.5$ V (due to the additional availability of states). Our calculations further demonstrate that the addition of OH greatly improves C_Q in the 18ZGNR case but only marginally in the 60ZGNR case. We should also note that unlike pristine graphene

electrodes, the ZGNR electrodes have intrinsically different C_Q profiles at the anode and cathode.
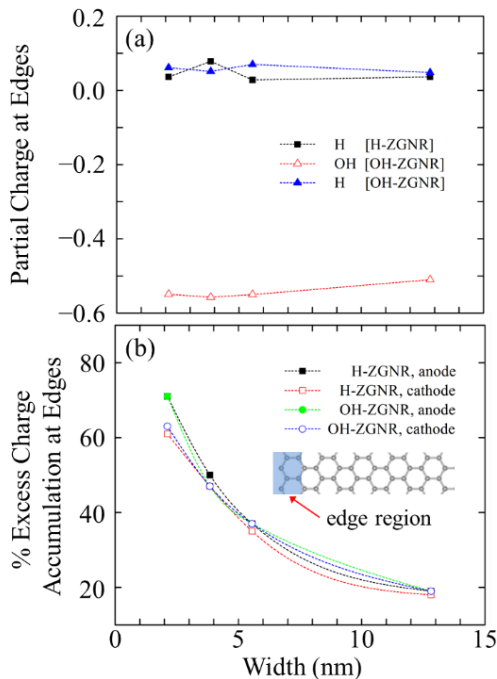
Figure 5.4   Estimated (a) partial charges of edge-passivating groups and (b) degree of excess charge accumulation at the edges of zigzag graphene nanoribbons (ZGNR) with varying width and edge-passivation. The partial charges were computed from grid-based Bader analysis. The excess charge accumulation was calculated from the fractional amount of excess charge found at the edges (defined by the shaded region) after one charge carrier was injected into each ZGNR.

Beyond the C_Q, we also explore the local charge redistribution at the edges of ZGNRs at varying widths; the charge redistribution is particularly important as it can affect the electrostatic interactions at the electrode-electrolyte interface. To quantify this behavior, we use grid-based Bader analysis to compute the atomic charges.[61] In Figure 5.4(a), we first present the atomic charges of the edge-passivating moieties of both H- and OH-ZGNRs. Here, the H and OH groups are expectedly positively and negatively charged,

which will affect the microstructure of the interface as discussed below. Yet also note that the partial charges seem insensitive to the width of the ZGNR. We then estimate the degree of excess charge accumulation at the edges in Figure 5.4(b); one electron or hole is injected into each system, after which the fraction of excess charge stored at the edges (defined up to a depth of 3.7 Å) is calculated. Both the H- and OH-ZGNR cases clearly demonstrate that the excess charge accumulation at the edges becomes more pronounced superlinearly as the GNR width becomes smaller. In the next section, we will discuss the implications of this behavior on the EDL microstructure and C_D.

5.4 DOUBLE LAYER MICROSTRUCTURE AND CAPACITANCE NEAR EDGES

A. Near Uncharged Electrodes

We study the EDL microstructure and C_D of OH-18ZGNR immersed in [BMIM][PF$_6$] IL, which serves as a model system to understand how the presence of edges can affect the interfacial structure and C_D. We begin with a thorough analysis of the IL microstructure near uncharged electrodes. Figure 5.5(a) shows the two-dimensional (2D) mass density (ρ_m) profiles of BMIM [left] and PF$_6$ [right] when $\sigma = 0$ C g^{-1}. First, we draw attention to the ion segregation and ordering near the edges. The PF$_6$ profile exhibits distinct high-intensity (color range from yellow to dark red) spots directly above/below the edges whereas BMIM exhibits low-intensity shades (color range from purple to blue). This indicates that PF$_6$ (BMIM) tends to be clustered (deficient) directly at the edge, which is primarily attributed to the strong electrostatic attraction (repulsion) between the PF$_6$ anion

(BMIM cation) and the positively charged H atoms. We also observe BMIM accumulation (PF$_6$ depletion) around the rims of the edges (adjacent to the negatively charged O atoms) and subsequent PF$_6$ accumulation (BMIM depletion) directly normal to the edge C atoms (which are positively charged). This alternating cascade of segregated anions and cations surrounding the edges results from the combined influence of electrostatic interactions between (i) anions/cations with the charged electrode atoms at the edges and (ii) IL ions with adjacent counterions. However, the degree of anion-cation segregation around the electrode tends to diminish near the basal region, as demonstrated by the mingled presence of high-intensity spots in both BMIM and PF$_6$ profiles. In Figure 5.6, we provide a snapshot of the IL ions adjacent to the electrode to visually demonstrate the decaying anion-cation cascade surrounding the electrode.

Next, we explore the variation in ρ_m as a function of distance from the electrode for BMIM and PF$_6$. The average ρ_m estimated along the edge direction ($48 < z < 52$ Å) [Figure 5.5(b)] shows a distinct (reduced) peak associated with PF$_6$ (BMIM) which can be expected based on Figure 5.5(a). Interestingly, the ρ_m profiles reveal alternating layering of anions and cations. Such behavior is typical of ILs near charged surfaces[108,110], indicating that the aforementioned charge redistribution toward the electrode edges is strong enough to trigger a similar response. In contrast, the average ρ_m estimated normal to the basal plane ($60 < y < 80$ Å) [Figure 5.5(c)] displays cation and anion profiles with spatial similarity (the ions maintain charge neutrality), which is consistent with previous studies near uncharged pristine graphene electrodes.[13-15] This suggests that although the basal plane is slightly positively charged due to the redistribution of electrons in the basal plane toward the edges

(σ_{basal} = 6.7 C g^{-1} or 0.5 μC cm^{-2}), the electrostatic interactions are not significant enough to induce anion/cation segregation in the normal direction.
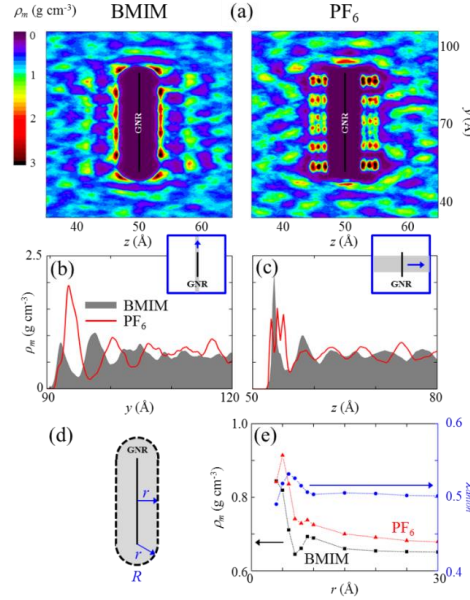
Figure 5.5 (a) Two-dimensional color map of mass density (ρ_m) profiles for BMIM and PF$_6$ near uncharged zigzag graphene nanoribbon electrodes alternatingly passivated by H and OH (OH-18ZGNR). The position of the electrode is indicated by the black line in the center of the color maps. (b) Average ρ_m along the edge direction (over the shaded region shown in the inset). (c) Average ρ_m along the basal plane (over the shaded region shown in the inset). (d) Schematic of region (R) used to calculate the average ρ_m surrounding the electrode as a function of distance (r). (e) Average ρ_m surrounding the electrode [left axis] and mixing parameter (χ_{anion}) of PF$_6$ [right axis].

It would also be interesting to quantify the extent of PF$_6$ segregation from BMIM in order to evaluate the net ionic charge accumulation surrounding the electrode due to the presence of edges. We compute a mixing parameter (χ) which is calculated within the region (R) defined with radial extension r as shown in Figure 5.5(d):

$$\chi = \frac{\int_R \rho_{m,anion}/MW_{anion} dR}{\int_R (\rho_{m,anion}/MW_{anion} + \rho_{m,cation}/MW_{cation}) dR} \tag{5.1}$$

where MW_i is the molecular weight of species i. The ρ_m averaged in R and χ_{anion} in R are presented in Figure 5.5(e), which shows a maximum $\chi_{anion} = 0.53$ at $r = 6$ Å that quickly tapers to $\chi_{anion} \approx 0.50$ when $r > 10$ Å. In other words, charge neutrality is essentially maintained despite the slight amassment of PF_6 anions. This suggests that the presence of edges primarily influences the ordering and segregation of ions surrounding the electrodes while the net ionic charge accumulation is only marginally affected.
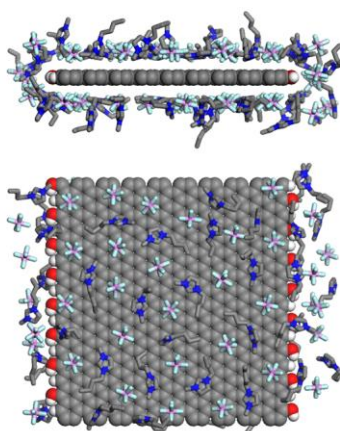
Figure 5.6   Snapshot of BMIM cations and PF_6 anions near uncharged OH-18ZGNR electrodes.   The grey/blue lines indicate BMIM while the pink/cyan lines indicate PF_6.   The grey, red, and white balls indicate the C, O, and H electrode atoms.
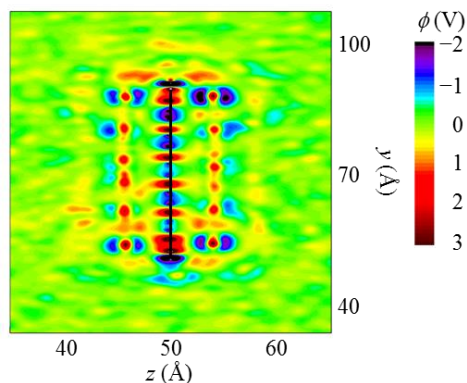
Figure 5.7   Two-dimensional color map of the potential (ϕ) profile near uncharged zigzag graphene nanoribbon electrodes alternatingly passivated by H and OH (OH-18ZGNR). The position of the electrode is indicated by the black line in the color map. The ϕ in the bulk region of the electrolyte is taken as reference (ϕ = 0 V).

To determine the C_D from the microstructure, we first estimate the potential of zero charge (ϕ_Z) under the current neutral conditions. From the computed space charge variation (ρ_q), which is determined from the distribution of electrode and IL atoms with fixed atomic charges, the two-dimensional Poisson's equation is solved (see Chapter 2) to calculate the potential variation (ϕ). In Figure 5.7, the 2D ϕ profiles are depicted where the ϕ in the bulk IL region is taken as reference (ϕ = 0 V). The ϕ_Z, then, is determined from the average surface ϕ of the electrode, which we find to be 0.22 V; note that $\phi_Z > 0$ V is consistent with the observed accumulation of PF_6 anions. For comparison, pristine graphene (at $\sigma_{basal} = 6.7$ C g^{-1}) is estimated to have a similar potential drop of 0.19 V (with $\phi_Z \approx 0$ V).

B. Near Charged Electrodes

Our analysis now extends to the case when the electrodes are charged. Figure 5.8(a)-(d) shows ρ_m near OH-18ZGNR electrodes when $\sigma = \pm 80.4$ C g^{-1} (± 6.2 μC cm^{-2}). Near the edges of both the cathode and anode, the profiles of each counterion (coion) increase (decrease) in both intensity and distinction as compared to the neutral case. This suggests that the alternating cascade of anions/cations surrounding the edges exhibits greater ion segregation than the uncharged case, which is expected since the majority fraction of injected charge carriers accumulate at the edges and thereby enhance the

electrostatic attraction (repulsion) with counterions (coions). Furthermore, the alternating cascade seems to extend further into the basal plane region when the electrode is positively charged rather than negatively charged. We postulate that this behavior manifests more strongly near the cathode since PF_6 anions are more compact and symmetric than BMIM cations, which therefore facilitates the layering along the electrode width.
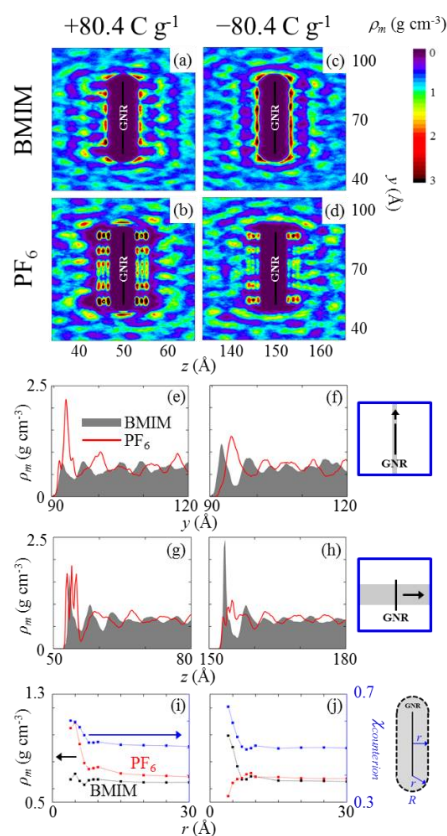
Figure 5.8   Mass density (ρ_m) profiles for BMIM and PF_6 near charged zigzag graphene nanoribbon electrodes alternatingly passivated by H and OH (OH-18ZGNR): (a-d) Two-dimensional color map of ρ_m for BMIM and PF_6 (the electrode position is indicated by the black line), (e-f) Average ρ_m along the basal plane (over the shaded region shown in the right panel), (g-h) Average ρ_m along the edge direction (over the shaded region shown in the right panel), (i-j) Average ρ_m surrounding the electrode and mixing parameter $\chi_{counterion}$) of the counterion as a function of distance (r) within the shaded region shown in the right panel.

We next examine the variation in ρ_m along the edge direction and normal to the basal plane. Figures 5.8(e)-(f) depict the average ρ_m in the edge direction near the cathode and anode, respectively. Here, the first peak in the PF$_6$ profile is noticeably enhanced (diminished) at the cathode (anode) edge. The first peak in the BMIM profile, on the other hand, is only marginally suppressed (augmented) at the cathode (anode) edge. In addition, the alternating layering behavior, as also seen in the uncharged case [Figure 5.5(b)], is maintained (suppressed) at the cathode (anode) edge. These observations suggest that the electrostatic interaction with the positively charged H atom still tends to dominate ion accumulation and segregation behavior directly at the edges since the injected charge carriers merely strengthen (reduce) the partial charge of H at the cathode (anode). In direct contrast, the average ρ_m profiles near the basal plane [Figure 5.8(g)-(h)] do not display distinct alternation between PF$_6$ and BMIM peaks, indicating that the ions are less noticeably segregated in the direction normal to the basal plane. In other words, the electrostatic interactions from the basal plane ($\sigma_{basal} \approx \pm 54.1$ C g^{-1}) are not strong enough to induce such layering behavior.

To quantify the overall counterion accumulation surrounding the electrode, we calculate $\chi_{counterion}$ and the corresponding R-averaged ρ_m profiles near the cathode and anode in Figure 5.8(i)-(j). Although it is readily apparent that the average ρ_m of counterions near the cathode tends to exceed that of the anode when $r < 6$ Å, the net ratio of counterions to coions remains similar for both cathode and anode. Therefore, the overall charge stored at the electrode-electrolyte interface is expected to be comparable near the cathode and

anode, despite differences in the edge-induced perturbations to their respective microstructures.
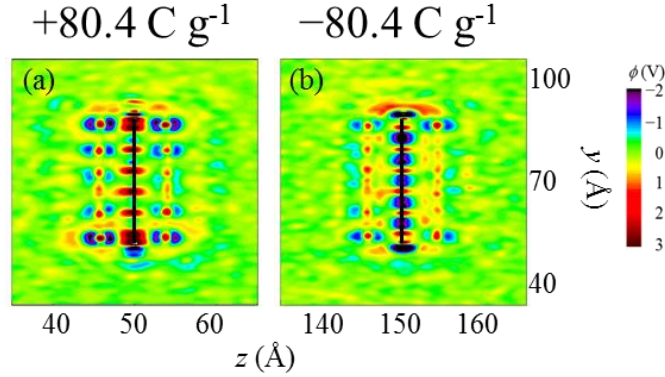
Figure 5.9   Two-dimensional color map of potential (ϕ) profiles near charged zigzag graphene nanoribbon electrodes alternatingly passivated by H and OH (OH-18ZGNR). The position of the electrode is indicated by the black line. The ϕ in the bulk region of the electrolyte is taken as reference ($\phi = 0$ V).

Figure 5.9 shows the predicted 2D ϕ profiles near the charged OH-18ZGNR electrodes. Using the same approach from the uncharged case, we estimated the average surface ϕ. Then taking the difference between the surface ϕ and ϕ_Z, we find that the potential drop in the EDL (ϕ_D) is 0.79 and -0.78 V for the cathode and anode, respectively. For comparison, the respective ϕ_D at $\sigma = \pm 80.4$ C g^{-1} in the pristine graphene case are 1.45 and -1.38 V. The reduction in ϕ_D should be unsurprising since most of the excess charge accumulates at the edges where it can be easily screened, thereby lowering the overall overscreening of counterions near the majority of the electrode. Correspondingly, the integral C_D using the OH-18ZGNR electrodes is 101.8 (103.1) F g^{-1} when $\sigma = 80.4$ (-80.4) C g^{-1}, which is nearly a factor of two greater than that of the respective C_D using pristine graphene. Given that the excess charge accumulation at the edges increases with the narrowing of the ZGNR, we may also expect the enhancement in C_D to increase in turn.

81

5.5 TOTAL INTERFACIAL CAPACITANCE

As summarized in Table 5.1, we have predicted the C_T and the applied potential (ϕ_a) when $\sigma = \pm 80.4$ C g^{-1} using OH-18ZGNR electrodes based on the combination of the integral C_Q and C_D ($1/C_T = 1/C_Q + 1/C_D$). We find that C_T is 80.2 (76.8) F g^{-1} at the cathode (anode), which is nearly twice that of the predicted C_T near pristine graphene. Based on our analysis of C_Q and C_D, it is clear that this enhancement can be attributed to significant gains in both C_Q and C_D. We therefore anticipate that the nano-engineering of carbon-based electrodes to incorporate a high-density of edges (such as from aligned GNRs[117], graphene quantum dots[123], or even large-scale vacancy defects[124]) could greatly benefit supercapacitors and deserves ample investigation.

Table 5.1 Summary of predicted capacitances for charged OH-18ZGNR electrodes in [BMIM][PF$_6$]. For comparison, the capacitance values for the pristine graphene case are also shown in parentheses.

σ	C_Q	C_D	C_T	ϕ_E	ϕ_D	ϕ_a
C g^{-1}		F g^{-1}			V	
+80.4	378.1 (134.7)	101.8 (55.4)	80.2 (39.3)	0.21	0.79	1.00
−80.4	300.6 (138.5)	103.1 (58.3)	76.8 (41.0)	−0.26	−0.78	−1.04

Throughout this assessment, we also contemplated the impact of several factors that were outside the scope of this work, but may be of interest in future research. For instance, it would be interesting to explore the influence of different edge-passivating functional groups on both the electronic structure and the EDL microstructure. In particular, the edge-induced perturbations to the EDL microstructure may be sensitive to the configuration and

size of the functional group as well as the relative strength of electrostatic interactions with the constituent atoms. Here, we should also note that stricter quantitative predictions using our method may require additional considerations. For example, we did not model charge polarization at the electrode-electrolyte interface for simplicity, which may affect the EDL microstructure as well as the electronic structure of the electrode. In addition, conventional DFT can introduce self-interaction errors which may underestimate charge localization, but can be mitigated using hybrid functional methods.[112] We also neglected charge transfer between [BMIM][PF$_6$] and the electrode since it appears to be unlikely.[125] Nevertheless, our computational approach is sufficient to demonstrate that the presence of edges can enhance the performance of supercapacitors by virtue of increasing both C_Q and C_D.

5.6 CONCLUSIONS

We investigated the impact of ZGNRs in [BMIM][PF$_6$] ionic liquid on the quantum and EDL capacitances (and therefore, the interfacial capacitance) using a combined DFT and classical MD approach. In our electronic structure analysis, we considered two different widths of H-passivated (H-18ZGNR and H-60ZGNR) and alternatingly H-/OH-passivated ZGNR (OH-18ZGNR/OH-60ZGNR) electrodes. Our results demonstrate that the electronic states are quasi-localized in the vicinity of the edges, although the degree of localization tends to decrease with increasing width. We then calculated the quantum capacitances (C_Q) from the electronic density of states. Comparisons with that of pristine graphene reveal that the ZGNR electrodes have significantly larger C_Q which are further

enhanced as the ZGNR width decreases. Furthermore, our results show that the degree of excess charge accumulation at the edges increases super-linearly as the ZGNR width decreases. We also studied the influence of edge defects on the EDL microstructure using the OH-18ZGNR as a model system when the excess surface charge density $\sigma = 0$ and ± 80.4 C g^{-1}. We find that the presence of edges induces an alternating cascade of PF$_6$ and BMIM ions in which the segregation is greatest near the edges. Upon charging, the microstructure of the EDL exhibits a greater response near the edges due to the preferential accumulation of excess charge carriers toward the edges. As a result, the EDL capacitance (C_D) of the OH-18ZGNR case is also predicted to be greatly enhanced when compared to the pristine graphene case. Finally, the total interfacial capacitance ($C_T = [1/C_D + 1/C_Q]^{-1}$) of the OH-18ZGNR case is found to experience a two-fold increase in comparison to the pristine graphene case when $\sigma = 80.4$ (-80.4) C g^{-1}. Our findings clearly highlight that the inclusion of a large density of edge defects in graphene-like electrodes can dramatically improve both C_Q and C_D, and therefore the overall performance of supercapacitors.

Chapter 6: Basal-Plane Oxidation

6.1 INTRODUCTION TO GRAPHENE OXIDE

In recent years, reduced graphene oxide (rGO) has gained popularity as an alternative graphene-based material. Part of the attraction is the cost-effective means of producing rGO from the wet exfoliation of graphene oxide and subsequent chemical, thermal, or electrochemical reduction.[126-128] While rGO has traditionally been used as a precursor for graphene sheets[128], rGO is also an interesting and important material in its own right. For instance, the oxygen moieties serve as electrochemically active sites which have been utilized for enhanced catalytic activity of oxygen reduction[129] and pseudo-capacitive benefits[130-132] in aqueous EDLCs. Naturally, rGO has also been explored for its use as an electrode material in supercapacitors using organic or ionic-liquid electrolytes which are electrochemically stable. To date, however, experimental results probing the advantages of rGO for EDLC applications have been widely scattered. While rGO electrodes have been shown to outperform graphene electrodes[133,134], reported capacitances have exhibited contradictory sensitivities to the ratio of oxygen to carbon atoms (O:C) and the reduction process[135,136]. This underscores the need to understand the influence of the extent of reduction on the capacitance.

To evaluate the impact of rGO reduction on EDLC performance, it is important to recognize that the total interfacial capacitance (C_T) strongly depends upon the contributions from the electrode quantum capacitance (C_Q) and electric double layer (EDL) capacitance (C_D). [13,34,35] While the latter property primarily depends upon the accumulation of ions at the interface, the former quantifies the ease in which excess charge carriers populate the electronic states of the electrode. To decouple these contributions, theoretical simulations can provide valuable insights. For example, molecular dynamics simulations have shown that regularly dispersed coverage of the basal plane of graphene with hydroxyl (OH) or epoxide functional groups tends to monotonically decrease C_D with increasing moiety content. [137-139] Quantum mechanical calculations have also shown that C_Q can be dramatically enhanced through OH functionalization of edge sites[140] as well as chemical modification[33,141] of basal sites, although the basal-plane coverage by OH has yet to be studied in this context. However, one challenge in undertaking such a fundamental investigation is a proper account of the rGO structure. Experimental characterizations using NMR spectroscopy and X-ray photo-electron spectrometry have identified the presence of several oxygen moieties such as OH, epoxide, carboxyl, and carbonyl groups, although the first two (OH and epoxide) are generally identified as the most common species along the basal surface. [142,143] Furthermore, recent experimental[144,145] and theoretical[146,147] work have shown that oxygen moieties tend to aggregate along the basal surface, forming distinct graphitic and oxidized regions. Therefore, careful attention should be applied in theoretical studies to account for such structures. To this end, one possible method is a lattice-based Monte Carlo scheme such as the one used by Zhou and Bongiorno.[146]

In this chapter, the effect of varying the O:C of rGO electrodes on C_T is investigated and compared to that of pristine graphene. Here, the OH functionalization of the basal surface of graphene is considered for simplicity while possible OH agglomeration is accounted using lattice-based Monte Carlo simulations. First, density functional theory (DFT) and density functional tight binding (DFTB) theory are employed in order to study the electronic structure, C_Q, and electrochemical stability of the rGO sheets. Then, classical molecular dynamics (MD) simulations are used in order to study the microstructure and C_D of the electrodes immersed in 1-ethyl-3-methylimidazolium bis(fluorosulfonyl)imide ([EMIM][FSI]) ionic liquid. Finally, the competition between C_Q and C_D is discussed in relation to the potential enhancement in rGO-based supercapacitor performance compared to that of pristine graphene electrodes.

6.2 COMPUTATIONAL METHODS

The electronic structure of each rGO sheet was calculated using DFT within the Perdew-Berke-Ernzerhof generalized gradient approximation[43] (GGA-PBE), as implemented in the Vienna Ab initio Simulation Package[42] (VASP). The projector augmented wave (PAW) method[69] was employed to describe the interaction between core and valence electrons with a planewave basis set using a kinetic energy cutoff of 400 eV. The rGO sheet was modeled using a 7×4 rectangular supercell (17.2648×17.0877 Å^2) with the PBE-optimized lattice constant of 2.466 Å for graphene. For all O:C cases, *trans* pairs of OH groups were added to the graphene lattice according to the Metropolis Monte Carlo

(MMC) scheme described later. As an example of the agglomeration, 68 OH groups (34 *trans* pairs) and 680 C atoms (O:C = 0.1) formed five domains on average with the largest domain covering 20% of the lattice. Periodic boundary conditions were employed in all three directions with a vacuum spacing of 20 Å in the vertical direction to separate the rGO sheet from its periodic images. For the Brillouin zone integration, a (6×6×1) Monkhorst-Pack (MP) *k*-point mesh[70] was used for geometry optimization and energy calculations, while a (8×8×1) MP *k*-point mesh was used to ensure convergence for electronic structure calculations; all energy (force) calculations were converged to within 1×10^{-6} eV (0.02 eV/Å). For comparison, third-order self-consistent charge DFTB calculations were performed using Slater-Koster parameters from Ref. 148 as implemented in the DFTB+ program.[149,150] For these calculations, a (13×13×1) MP *k*-point mesh was used for geometry optimization and electronic structure calculations with the same convergence tolerance.

The calculated C_Q values were based on larger rGO sheets (17×10 rectangular supercells corresponding to 41.9288×42.7193 $Å^2$) which were prepared using the same MMC scheme with 9, 34, and 102 *trans* pairs of OH groups added to the lattice, yielding an O:C = 0.026, 0.1, and 0.3, respectively. Here, a (5×5×1) MP *k*-point mesh was used for geometry optimization and electronic structure calculations. Partial atomic charges were computed using Mulliken population analysis[151] for excess charge density σ = 0, ±2.24, ±4.47 $\mu C/cm^2$ (0, ±5, and ±10 *e* per sheet); these charges were used in the MD simulations which are described below. All reported results were obtained from averages over five independent samples at each O:C.
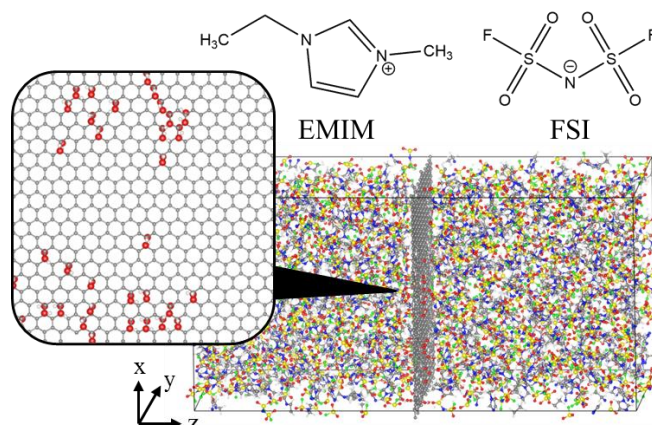
Figure 6.1. Schematic of EMIM/FSI ionic liquid (top) and the simulation domain used in classical molecular dynamics (bottom). The gray sheet in the middle corresponds to graphene oxide which is shown in the magnified inset; gray, red, and white balls indicate C, O, and H atoms, respectively. Throughout the electrolyte, the gray, blue, and white balls correspond to the respective C, N, and H atoms in EMIM while the blue, yellow, red, and green balls correspond to the respective N, S, O, and F atoms in FSI.

The MD simulations employed the OPLS-AA force field[50,101] and were used to determine the microstructure of [EMIM][FSI] and potential variation near pristine and selected rGO electrodes when $\sigma = 0$, ± 2.24, and ± 4.47 $\mu C/cm^2$. As illustrated in Figure 6.1, the simulation domain consists of 434 [EMIM][FSI] IL pairs surrounding an electrode (41.9288×42.7193 Å^2) with a depth of 86 Å in the z-direction and periodic boundary conditions in all three directions; in the charged simulations, co-ions were removed from the domain to maintain charge neutrality. Note that the domain is large enough to obtain a bulk density of 1.43 g/cm^3 far from the electrode, which is in agreement with previous simulation work[152]. The structure and charge distribution of the electrodes were determined from DFTB calculations, as described above. The force field parameters for EMIM and FSI were adopted from Refs. 153 and 154, respectively. The Lennard-Jones (LJ)

parameters for graphene and for the OH moieties were adopted from Refs. 155 and 101, respectively. Spherical cutoffs of 10 Å and 12 Å were used for the LJ and Coulomb interactions, respectively. Electrostatic interactions beyond the cutoff were calculated using the Particle-Particle Particle-Mesh solver.[54]

While keeping the electrodes fixed, each MD simulation was annealed and quenched initially at 700 K for 3 ns followed by 2 ns at 350 K for two cycles (*i.e.*, 10 ns total), and then further equilibrated for 3 ns at 300 K using a 1 fs time step. Production runs were carried out for 4 ns with atomic positions recorded every 5 ps. All simulations were in the NVT ensemble with the temperature controlled by a Nose-Hoover thermostat[60] with a 200 fs damping parameter. All MD simulations were performed with the Large-scale Atomic/Molecular Massively Parallel Simulator (LAMMPS) program.[105] MD results reported herein were obtained from the average of five independent simulations with different initial atomic configurations.

6.3 HYDROXYL AGGLOMERATION ON BASAL PLANE

To determine the rGO structure, we use lattice-based Metropolis Monte Carlo simulations using a pair-wise potential model developed based on GGA-PBE energetics from DFT calculations. First, we approximate the pair-wise interaction energy per OH moiety ($E_{p,OH}$) when homogeneously dispersed on the basal surface of graphene at different concentrations:

$$E_{p,OH} = \frac{E_{system} - E_{Gr} - nE_{OH}}{n} \tag{6.1}$$

90

where E_{system} is the total energy of the system, E_{Gr}/E_{OH} are the reference energies of pristine graphene and OH, and n is the number of OH groups; here we used $E_{OH} = \frac{1}{2} E_{O2} + \frac{1}{2} E_{H2}$. A summary of the calculated $E_{p,OH}$ at varying concentrations (quantified by the average nearest neighbor distance D_{OH}) can be found in Table 6.1. An expression for $E_{p,OH}$ is then interpolated, yielding the following equation which reflects the tendency of OH moieties to aggregate:

$$E_{p,OH} = -\frac{3.0816}{D_{OH}} - 0.2906 \tag{6.2}$$

Using this expression for $E_{p,OH}$, the energy of graphene decorated with OH moieties ($E_{Gr/OH}$) can be approximated as:

$$E_{Gr/OH} = \Sigma_i E_{p,OH,i} \tag{6.3}$$

summed over every OH group i. To prepare each MMC simulations for graphene oxide sheets with n OH groups, we first randomly covered a graphene lattice with $n/2$ trans pairs of OH moieties; for simplicity, we only allowed one trans pair in each graphene unit cell. Then, a trial configuration was created by shifting one trans OH pair to a random unoccupied lattice point. The probability (P) of accepting this configuration was then computed as follows:

$$P = min\left[1, exp\left(-\frac{\Delta E}{k_B T}\right)\right] \tag{6.4}$$

where ΔE is the energy difference between the trial and current state. Next, a random number $R = [0,1)$ is generated to determine if this configuration is selected (*i.e.*, if $R < P$). This process is repeated for 15000 trials with the Boltzmann factor ($k_B T$) ramping down from 0.086 ($T = 1000$ K) to 0.026 ($T = 300$ K).

Table 6.1   Summary of the average nearest neighbor distance between O atoms (D_{OH}) and pair-wise interaction energy per OH moiety ($E_{p,OH}$) for the listed supercell systems.

System	D_{OH} (Å)	$E_{p,OH}$ (eV)
$C_{32}(OH)_2$	9.23	-0.68
$C_{32}(OH)_8$	4.61	-0.82
$C_{32}(OH)_{16}$	3.42	-1.28
$C_{32}(OH)_{24}$	2.64	-1.41
$C_{32}(OH)_{32}$	2.62	-1.51

Averaging over 5 independent cases for O:C ranging from 0.026 to 0.3, we calculate the number of OH domains and the fractional size of the largest domain as shown in Figure 6.2. Here, lattice points containing OH groups are considered a part of a contiguous domain if within one nearest neighbor distance. From Figure 6.2, it is evident that our MMC scheme predicts that most of the OH groups aggregate into one large domain as O:C increases. Furthermore, for this supercell size (41.9288×42.7193 Å^2), the fragmentation of domains limits itself to around 4 distinct groups (of widely varying size).
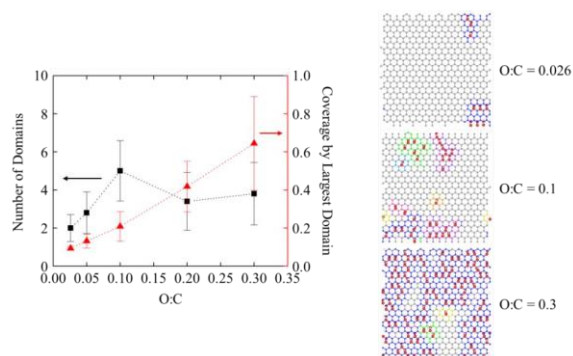
Figure 6.2   (left) Number of OH domains and fractional coverage by largest OH domain for reduced graphene oxide (rGO) sheets with the listed oxygen to carbon ratio (O:C) generated from Metropolis Monte Carlo simulations. (right) Snapshots of rGO cases at the listed O:C with the domains colored in blue, green, purple, orange, or yellow. Red/white balls represent O/H atoms while gray balls represent C atoms.

92

6.4 COVERAGE EFFECT ON ELECTRONIC STRUCTURE AND QUANTUM CAPACITANCE

In this section, the electronic structure of rGO is reported at different OH contents (*i.e.*, O:C). First, the electronic density of states (DOS) of rGO at O:C = 0.054 and O:C = 0.268 are analyzed using DFT-GGA. Next, the viability of using the DFTB approach in place of DFT-GGA is demonstrated. Using DFTB, we then proceed to calculate the influence of O:C on the integral C_Q of rGO.
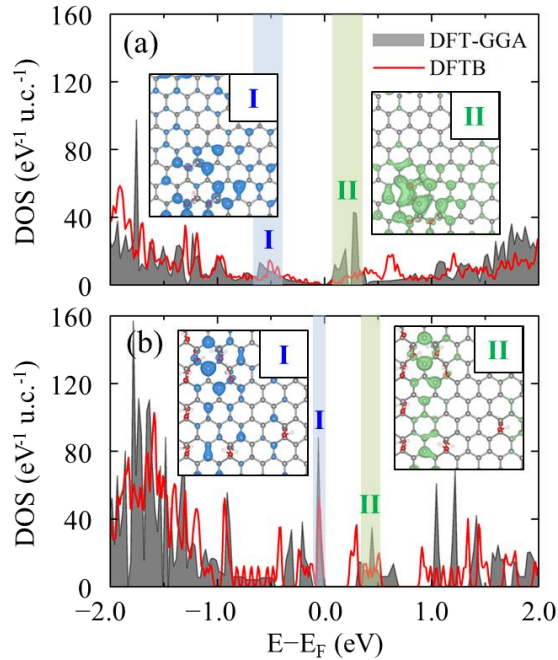
Figure 6.3   The density of states (DOS) of reduced graphene oxide with respect to the Fermi level (E_F) when (a) O:C = 0.054 and (b) O:C = 0.268, as calculated using the listed quantum mechanical methods. The insets show the band-decomposed charge density isosurfaces (0.001 *e*/bohr^3) for the highlighted regions I and II, in which blue and green isosurfaces correspond to electrons and holes, respectively.

Figure 6.3(a) depicts the total DOS of a rGO sheet with O:C = 0.054. The sharp peaks seen above the Fermi level (E_F) [0 < E−E_F < 0.4 eV] are indicative of quasi-

localization of states arising from the presence of OH groups, similarly present in the cases of graphene with chemical dopants[33,141] and topological defects[156,157]. As seen from the band-decomposed charge density isosurfaces of regions I and II, the quasi-localized states near E_F are primarily associated with the p_z states of C atoms nearby OH moieties where the π system is most distorted; note that we find the O 2p states to be 1.8 eV below E_F. In the O:C = 0.268 case [Figure 6.3(b)], the density of quasi-localized states near E_F is found to increase since the distortion to the π system intensifies with the addition of more OH groups; here, a gap of 0.28 eV is also predicted to appear.
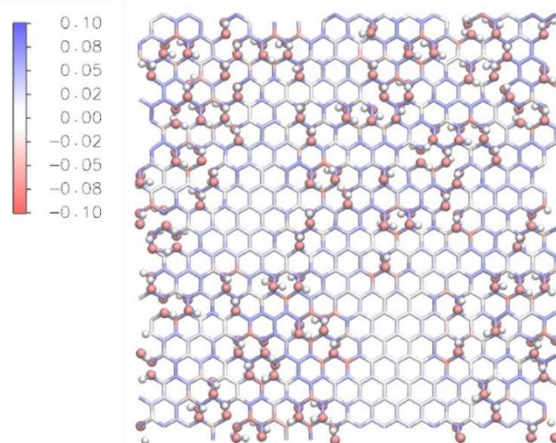
Figure 6.4   Color map of atomic charges calculated from Mulliken population analysis for rGO with O:C = 0.3 and excess surface charge density $\sigma = 0$ $\mu C/cm^2$. Blue and red colors along the carbon lattice represent positive and negative charge, respectively; note that the electropositive C atoms are within the vicinity of the OH moieties which are depicted by red and white balls. All calculations were performed using DFTB+ for a 17x10 rectangular supercell.

The presence of OH moieties consequently influences the charge distribution along the rGO sheet. The OH moieties expectedly withdraw electrons from the π system and thereby act as a p-type dopant; hence, the adjacent C atoms are electropositive (as depicted

94

in the charge distribution map in Figure 6.4). We can also expect excess charge carriers to primarily fill the π system with slight accumulation near the OH sites where the degree of quasi-localization is largest. Later, we will discuss the implications of the resultant charge redistribution on the electrode-electrolyte interactions at the interface.

As our goal is to investigate the electronic structure of large and disordered sheets of rGO with as many as thousands of atoms in a unit cell, we now consider the efficacy of an alternative and less-expensive computational method. In Figure 6.3(a)-(b), we compare the DOS predicted by DFT-GGA to that of DFTB and find that the latter sufficiently approximates the former. However, it is clear that the DFTB method systematically underestimates the electronic localization relative to DFT-GGA. For example, in the case of O:C = 0.054, the empty states in the DFTB DOS are broadened such that the peak appears around 0.3 eV above its relative position predicted using DFT-GGA. Furthermore, the band gap in the O:C = 0.268 case is predicted to be 0.06 eV smaller from the DFTB calculation. Nonetheless, DFTB captures the general availability of states near E_F, which ultimately determines C_Q. Herein, we will use the DFTB method to estimate the DOS of rGO with varying O:C.

Figure 6.5 shows the integral C_Q as a function of local electrode potential (ϕ_G) calculated for larger rGO sheets (41.9288×42.7193 Å^2) with O:C = 0.026, 0.1, and 0.3 and for pristine graphene. Based on DFTB calculations, C_Q was computed using procedure described in Chapter 2 from the DOS averaged over all samples [inset of Figure 6.5]. In comparison to pristine graphene, the overall C_Q of the rGO sheets tends to increase as O:C increases, especially close to the charge neutrality point, which reflects the additional

95

availability of states resulting from the disruption of the π system by OH groups; note that C_Q can vary as much as ± 125 F/g due to different configurations of OH moieties. Furthermore, it is evident that the OH-induced enhancement in C_Q tends to be more dramatic with positive polarity. Interestingly, our calculations predict that rGO remains metallic when O:C = 0.3. In the absence of structural defects, this may be reasonable as the percolation threshold of thermally-reduced GO was found to be around O:C = 0.2.[158] Yet recall that when O:C = 0.268 in the above calculation, we observe a band gap of 0.22−0.28 eV. These conflicting results suggest that the band gap in the latter case may be induced by a super-lattice effect, owing to the smaller supercell size.
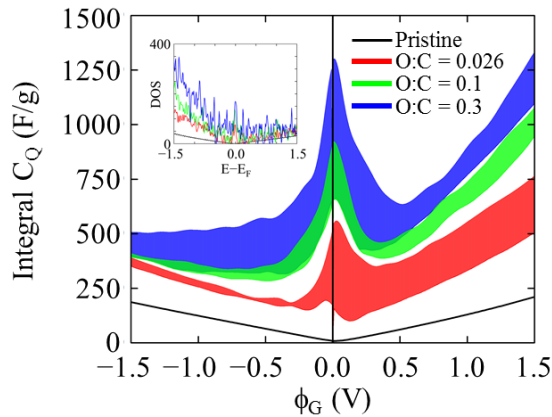
Figure 6.5   Comparison of the integral quantum capacitance (C_Q) for pristine graphene and reduced graphene oxide (rGO) with the listed OH to carbon ratios (O:C) at varying local electrode potential (ϕ_G). The width of the profiles corresponds to the standard deviation of the mean sampled over five different rGO configurations. The inset shows the corresponding density of states (DOS in $eV^{-1}u.c.^{-1}$) with respect to E-E_F (in eV).

To test the super-lattice effect, we calculate the electronic structure of rGO with homogeneously dispersed OH moieties across the basal surface and predict a band gap of 0.45 eV (Figure 6.6). This opening of a band gap is akin to the Robertson and O'Reilly

model in which the optical gap of amorphous carbon varies inversely with the size of homogeneous sp^2 clusters.[159] Hence, we can attribute the emergence of the large band gap to the regularity of the disruption and subsequent confinement of aromatic regions by OH moieties. In the aforementioned rGO sheets constructed with a smaller supercell size, favorable OH moiety configurations can accommodate less agglomeration (*i.e.*, more homogeneous dispersion) due to the periodic images and therefore result in a band gap. In contrast, the agglomeration of OH moieties in the larger supercell results in separate and contiguous functionalized and graphitic domains, in which the π system remains well-coupled and metallic (refer to Figure 6.1). These results indicate that the electronic structure of rGO sheets can be quite sensitive to the spatial distribution of O species, in addition to their concentrations.
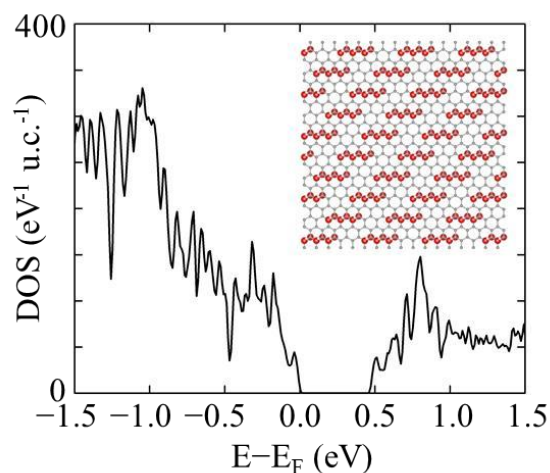
Figure 6.6   Density of states (DOS) with respect to the Fermi level (E_F) of rGO with O:C = 0.3 and nearly homogeneous coverage (using a 17x10 rectangular supercell); the inset shows a snapshot of the rGO structure where red/white represent O/H atoms while gray atoms represent C atoms. A band gap of 0.45 eV is predicted.

6.5 ELECTROCHEMICAL STABILITY OF HYDROXYL FUNCTIONALIZED GRAPHENE

In this section, we discuss the possible irreversible loss of OH moieties from the basal surface upon cycling. In ILs (and other non-aqueous electrolytes), we propose that OH can be reduced to form an OH^- anion, which subsequently extracts a H^+ from adjacent OH groups to form H_2O in the following 1 e^- process:

1. $rGO\text{-}OH + 1e^- \rightarrow rGO + OH^-$

2. $OH^- + rGO\text{-}OH \rightarrow rGO\text{-}O^- + H_2O$

Unlike buffer solutions, which are traditionally used during electrochemical reduction[128,160], the H^+ source is limited by the availability of surface OH groups; conceivably, nearby H_2O may also contribute H^+ but we do not consider this case here. Based on this mechanism, the energy of H_2O evolution (ΔE_{evo}) can be computed from the energy difference of the final and initial states ($\Delta E_{evo} = E_{H2O/O-} - E_{GO}$).
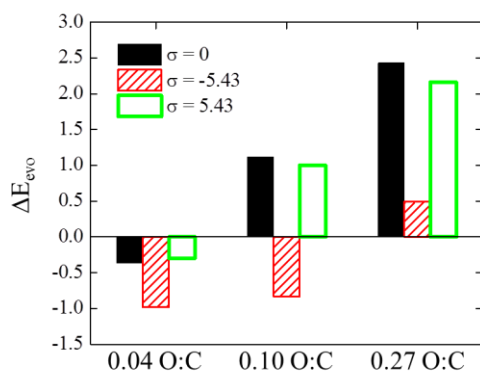
Figure 6.7   The predicted energy of H_2O evolution (ΔE_{evo}) with varying O:C at the listed excess surface charge density (σ in $\mu C/cm^2$). The evolution of two H_2O molecules (one on each side of graphene) is considered in all cases.

Our interest is in evaluating ΔE_{evo} at varying O:C using DFT. We consider the previously used 7×4 rectangular supercells and allow one H_2O to evolve on each side of the rGO sheet; for completeness, the ΔE_{evo} for the neutral, anodic, and cathodic cases are calculated and shown in Figure 6.7. First, it is evident that at low O:C ratios (= 0.04), H_2O evolution is favorable and expectedly more so under cathodic potential ($\sigma = -5.43$ $\mu C/cm^2$). However, we find that the evolution becomes increasingly unfavorable as O:C increases. Therefore, within a fixed operating potential, our results suggest that a critical O:C exists, beyond which the loss of OH moieties can be mitigated.

To understand the origins of this behavior, we refer to our previous electronic structure analysis. Recall that an increase in O:C is commensurate with greater quasi-localization of π states near E_F. Hence, the preferential filling of excess charge carriers in these π states should increase with O:C and consequently it is less likely for electrons to localize on an OH site to form OH^-. Note that this behavior should be sensitive to the types of oxygen moieties (such as basal-plane epoxides and edge-plane carboxyls, carbonyls, and lactols) as well as their relative concentrations, which could be a subject of further study. Nonetheless, this analysis demonstrates that the increased disruption of the π system at increased O:C ratios may enhance both the C_Q and cycling stability of rGO electrodes.

6.6 COVERAGE EFFECT ON DOUBLE LAYER MICROSTRUCTURE AND CAPACITANCE

To evaluate the integral C_D, the microstructure of [EMIM][FSI] near rGO electrodes (O:C = 0.1 and 0.3) is investigated and compared to that of pristine graphene

electrodes. Here, MD simulations are used to examine how the presence and distribution of OH moieties influence the EDL microstructure across the basal plane as well as perpendicular to it. Due to the wide electrochemical window of [EMIM][FSI], it is assumed that non-bonding vdW and Coulomb interactions sufficiently model the interfacial behavior. First, we present the packing behavior of IL ions under neutral conditions. Next, the screening capabilities of the ILs upon electrode charging are discussed. Lastly, we estimate the variation of C_D as a function of O:C.
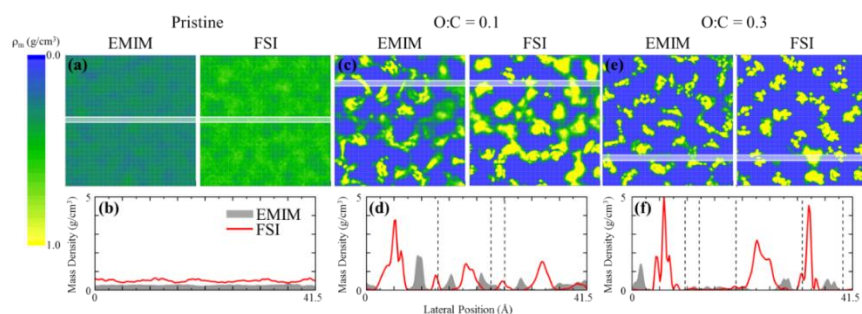
Figure 6.8   Average two-dimensional mass density (ρ_m) profiles of EMIM and FSI in the first ionic liquid layer for the (a) pristine, (c) O:C = 0.1, and (e) O:C = 0.3 graphene cases, which are shown as color maps. The respective line profiles of the segments along the highlighted region are shown in (b), (d), and (f), respectively.

Figure 6.8 depicts the two-dimensional (2D) mass density (ρ_m) color map of the first IL layer (thickness $\approx$ 3.4 Å) under neutral conditions. Near pristine graphene [Figure 6.8(a)], the EMIM and FSI ions expectedly pack uniformly across the basal plane. This is further demonstrated in the line profile [Figure 6.8(b)] which is nearly flat; note that although FSI has a greater ρ_m due to its larger molecular weight, the number densities of FSI and EMIM are comparable in order to maintain charge neutrality. On the other hand, the EDL exhibits markedly different behavior near the rGO electrodes. The first EDL layer

100

by the rGO sheet with O:C = 0.1 [Figure 6.8(c)], for example, displays distinct spatial

aggregation between EMIM cations and FSI anions. The line profile in Figure 6.8(d)

further demonstrates that the anions and cations tend to segregate within the 2D plane; this

is mainly driven by the aforementioned charge redistribution (Figure 6.4) such that cations

(anions) prefer to aggregate close to the exposed negatively-charged O (positively-charged

H) atoms, which triggers successive alternating packing across the unmodified basal

region. As the oxygen surface coverage increases [O:C = 0.3 in Figure 6.8(e)-(f)], the 2D

segregation becomes noticeably more distinct. We should note that similar 2D structural

ordering has also been theoretically demonstrated due to atomically rough substrate

surfaces[161] and polarization-induced charge puddles[162].
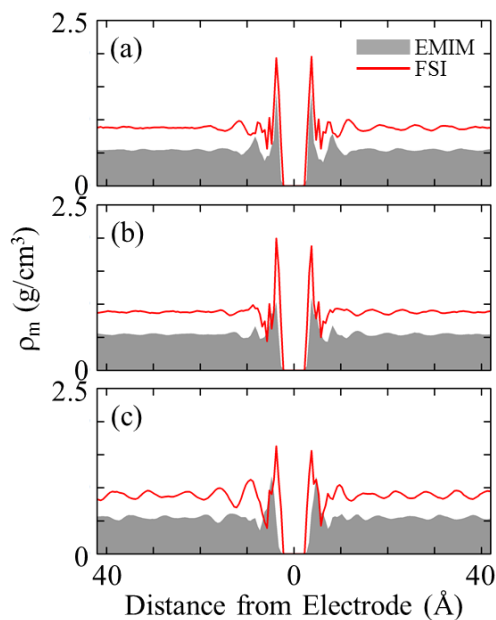
Figure 6.9   One-dimensional mass density (ρ_m) profiles of EMIM and FSI in the direction
perpendicular to the neutral electrode for the (a) pristine, (b) O:C = 0.1, and
(c) O:C = 0.3 graphene cases.

The one-dimensional (1D) microstructure perpendicular to the basal plane also displays some differences as O:C changes. Figure 6.9(a) shows the average ρ_m as a function of distance from an uncharged pristine graphene electrode, which exhibits the well-known oscillatory packing behavior for ILs that dampens away from the electrode[13-15]; the sharp first peak reflects the tendency of both the EMIM and FSI ions to flatten at the interface due to the vdW interaction with the electrode. Similar oscillatory behavior is observed when O:C = 0.1 [Figure 6.9(b)] and O:C = 0.3 [Figure 6.9(c)], although the first peaks tend to broaden; this suggests that some of the ions re-orient in order to screen the charge from the out-of-plane OH groups. In addition, the FSI anions tend to be segregated from the EMIM cations as indicated by the down-shifted position of the EMIM peak with respect to the FSI peak. We can expect a slight preferential accumulation of FSI anions near the basal plane to screen the slightly electropositive C atoms while EMIM prefer to screen the out-of-plane electronegative O atoms.

When the electrodes are charged, it can prove useful to analyze the screening behavior of the IL ions. Based on the charge density variation (ρ_q), which is proportional to ρ_m, we can compute the relative screening factor β_{rel},

$$\beta_{rel} = -\frac{\int_0^z \rho_{q,\sigma}\,dz - \int_0^z \rho_{q,0}\,dz}{\sigma} \tag{6.5}$$

where $\rho_{q,\sigma}$ and $\rho_{q,0}$ are the charge density distributions at $|\sigma| > 0$ and $\sigma = 0$ $\mu C/cm^2$, respectively; since the electrode is screened from both sides, β_{rel} should saturate to a value of 0.5 far away from the electrode.
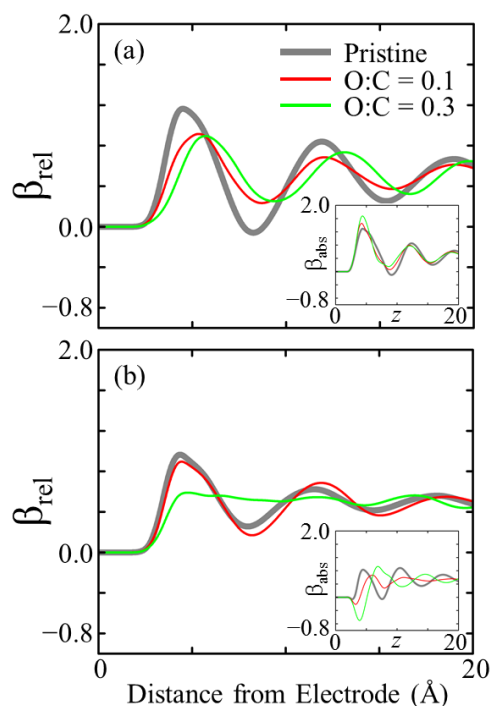
Figure 6.10 The average relative screening factor (β_{rel}) in the direction perpendicular to the listed electrodes when the excess surface charge density (a) $\sigma = 2.24$ $\mu C/cm^2$ and (b) $\sigma = -2.24$ $\mu C/cm^2$. The insets depict the absolute screening factor (β_{abs}) as described in the manuscript.

As seen in Figure 6.10(a), the compact first IL layer near pristine graphene has a peak $\beta_{rel} = 1.2$ around 4.5 Å when $\sigma = 2.24$ $\mu C/cm^2$. In contrast, the first β_{rel} peak for the O:C = 0.1 and 0.3 cases are respectively broadened and shifted away from the electrode, indicating that the relative screening capability of the IL ions are increasingly impeded as O:C increases. When $\sigma = -2.24$ $\mu C/cm^2$ [Figure 6.10(b)], similar behavior is observed in which the peak β_{rel} broadens and diminishes as O:C increases; note, however, that the peak β_{rel} is around 1.0 (0.6) in the pristine (O:C = 0.3) graphene case, which is comparably smaller than the peak β by the positive terminal. These results suggest that the accumulation of counterions at the electrode-electrolyte interface is increasingly unfavorable as O:C

increases; in other words, the electrostatic attraction from the excess electrode charge is insufficient to induce the exchange of coions for counterions within the 2D segregated microstructure in the first IL layer [Figure 6.8].

While β_{rel} offers an intuitive means of quantifying the ease of additional counterion accumulation at the charged electrode interface, it does not reflect the absolute screening capabilities of the IL ions. Instead, we can compute the absolute β (β_{abs}) which is simply the equivalent of β_{rel} without the reference (*i.e.*, second) term. As depicted in the inset of Figure 6.10(a), the β_{abs} peak is largest in the O:C = 0.3 case near the positive terminal, which naturally follows the previously demonstrated accumulation of FSI counterions at the rGO interface [Figure 6.9]. The β_{abs} profile near the negative terminal [Figure 6.10(b)] also exhibits a valley due to the presence of FSI coions. Hence, the decrease in screening capability near negative polarity as compared to positive polarity is likely driven by the tendency of the first IL layer to be depleted of EMIM counterions due to FSI accumulation.

Next, the integral C_D is determined from the ratio between σ and the difference between the potential drops across the EDL when charged (ϕ_D) and uncharged (ϕ_Z, *i.e.*, PZC) [$C_D = \sigma/(\phi_D-\phi_Z)$]; the potential profiles are calculated by numerically solving Poisson's equation in 3D Fourier space. Figure 6.11 summarizes the behavior in C_D as O:C and σ vary. In the pristine graphene cases, it is evident that C_D tends to be around 125−135 F/g. However as the O:C of the electrode increases, C_D is predicted to diminish. Additionally, the suppression in C_D tends to be larger at the negative terminal, which exhibits as much as a 42% decrease in C_D as compared to the 35% decrease on the positive

terminal side. Both of these observations are consistent with the aforementioned screening

behavior which tends to decrease as O:C increases, and more so near the negative electrode.
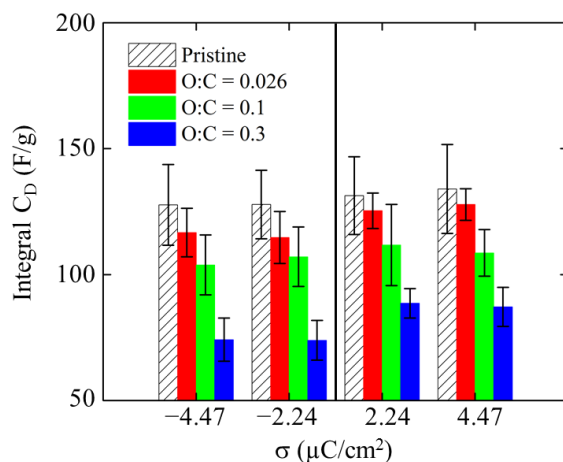
Figure 6.11 Comparison of the integral electric double layer capacitances (C_D) for pristine
graphene and three graphene oxide sheets with varying O:C at the listed
excess surface charge densities (σ).

6.7 TOTAL INTERFACIAL CAPACITANCE

Having estimated the C_Q and C_D, we now compute the interfacial capacitance (C_T

$= (1/C_Q + 1/C_D)^{-1}$). Figure 6.12 summarizes our results and shows that the C_T is enhanced

by as much as 41% (33%) for positive (negative) polarity when using OH-functionalized

electrodes with O:C = 0.1 as compared to that of pristine graphene; note that when σ =

± 4.47 $\mu C/cm^2$, the predicted operating voltage (ΔV) is 2.44 V in the C:O = 0.1 case, which

is much smaller than the 3.74 V predicted for the pristine graphene case. Despite the

diminished C_D upon OH functionalization, we find that the C_T can be dramatically improved by virtue of the enhanced C_Q.
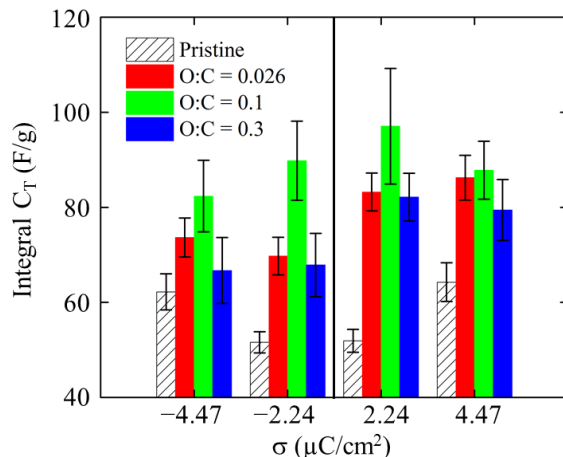
Figure 6.12   Comparison of the integral interfacial capacitances (C_T) for pristine graphene and three graphene oxide sheets with varying O:C at the listed excess surface charge densities (σ).

In addition, our results do suggest that there may be an optimal O:C in which the benefit from the C_Q most effectively mitigates the loss in C_D. However, there are several limitations in our simulations that prevent us from quantifying such a point. First, we did not take into account the charge smearing at the electrode-electrolyte interface which may have underestimated our prediction of the C_D.[88] More importantly, the C_Q can be altered in the presence of other types of oxygen moieties, as well as their concentrations and distributions across the basal plane. In particular, we should be wary of rGO sheets with band gaps that have been predicted to be as large as 3.0 eV which can occur when O:C > 0.5 for certain combinations and configurations of oxygen-containing functional groups.[147,163] Furthermore, the presence of additional topological defects that may be created through the rGO reduction process[164] can also strongly influence the electronic

structure as well as their electrochemical stability. It is possible that the highly scattered performance of GO-based supercapacitors reported in the literature may be partially due to the structurally-sensitive C_Q. Moreover, the possible suppression of electrical conductivity in rGO sheets with increased oxygen functionalization is another factor to consider.[131] Therefore, it will be important to improve both the experimental characterization and control of oxygen functionalization on rGO in order to fully utilize these materials for supercapacitor electrodes. Nonetheless, our study reveals that rGO materials, which are particularly attractive due to their ease in processing and scalability, can serve as a superior alternative to graphene electrodes for EDLC applications.

6.8 CONCLUSIONS

We investigated the influence of reduced graphene oxide (rGO) electrodes immersed in [EMIM][FSI] ionic liquid on both the quantum (C_Q) and electric double layer (C_D) capacitances using a combined DFT and classical MD approach. As a model system, we only considered OH moieties along the basal plane, while accounting for their preferential spatial agglomeration, and vary the ratio of OH to C (O:C). Our three primary conclusions are:

- Increasing O:C (computed up to the O:C = 0.3 case) induces increasing quasi-localization of C p_z states, which subsequently enhances the C_Q and electrochemical stability of OH on the basal surface.

- The C_D can be repressed as O:C increases, which we attribute to the unfavorable exchange of counterions with coions adjacent to the electrode surface due to the preferred two-dimensionally ordering of cations and anions.

- The total interfacial capacitance ($C_T = [1/C_Q + 1/C_D]^{-1}$) using OH-functionalized electrodes is predicted to outperform pristine graphene electrodes owing to the mitigation of the suppressed C_D by improved C_Q; for example when $\sigma = 4.47$ (-4.47) $\mu C/cm^2$, C_T is predicted to improve by 41% (33%).

Interestingly, our analysis suggests that the intended benefit from rGO electrodes strongly depends upon both the concentration and arrangement of oxygen species. This may help explain some inconsistencies reported in experimental results while advocating the need for careful control, characterization, and optimization of oxygen functionalization. Nonetheless, our findings clearly demonstrate that the use of rGO materials can significantly improve C_T as compared to pristine graphene and therefore offer a promising alternative for supercapacitor devices.

PART II: NANOPOROUS CARBON MATERIALS

Extending on the concepts identified in Part I, Part II aims to develop materials design principles for the use of nanoporous carbon in supercapacitors. Nanoporous carbon materials consist of graphene-like sheets that are contorted into three-dimensional single-atom-thick networks consisting of both negative- and positive-curvature surfaces (due to the presence of topological defects). In addition to the inherently large surface area of these materials, recent studies have purported that ion confinement within nanopores may enhance capacitance. However, the exact nature of this enhancement and the factors that contribute to it remain unclear.

The fundamental charge storage mechanisms using nanoporous carbon electrodes are systematically explored by means of theoretical simulations. First, the influence of positive curvature on the ionic liquid microstructure with an external potential is explored. Then, the confinement of ions within charged subnanometer pores are investigated. Finally, realistic nanoporous carbon electrodes filled with ionic liquid are studied. In all of these cases, the intent is to probe the relationship between the electrode structure and both the static and dynamic accumulation of electrode charge and ions.

Chapter 7: Influence of Carbon Nanotube Curvature on Capacitance

7.1 INTRODUCTION TO CARBON NANOTUBES

Carbon nanotubes (CNTs) have generated significant interest for use in a variety of applications, including field-effect transistors, chemical sensors, energy conversion devices, and energy storage devices.[165,166] In particular, the incorporation of carbon nanotube-based electrodes in EDLCs have demonstrated superior performance compared to conventional activated carbon electrodes.[167-171] Recent experimental work by Honda and coworkers has demonstrated that the electrode topology, specifically different CNT curvatures, can significantly impact the EDLC capacitance.[168,172] While these studies can begin to elucidate the behavior of EDLCs with various electrode topologies, our understanding of the phenomena at the electrode-electrolyte interface is still limited due largely to difficulties in experimental characterization at the molecular scale.

The majority of theoretical studies[173,174] have focused on how inner pore sizes influence the double layer capacitance (C_D), yet few have investigated the role of the positive (or outer) pore curvature. Huang and coworkers developed a model based on a classical geometric capacitor and suggested that C_D increases with decreasing CNT radius.[175] From classical molecular dynamics (MD) simulations, Feng and coworkers also showed that a (5,5) CNT electrode results in at least a 30% enhancement in capacitance

compared to planar graphene electrodes with 1-butyl-3-methyl-imidazolium hexafluorophosphate ([BMIM][PF$_6$]) and [BMIM][Cl] ILs.[85] A recent study from the same group also predicted that the C_D increases nonlinearly with CNT curvature in [EMIM][TFSI] IL, with symmetric behavior at the anode and cathode due to the similarity in cation/anion size.[176] A detailed analysis of the impact of both different CNT curvatures and cation/anion asymmetry on the EDL microstructure and C_D, however, is still lacking.

Based on the work presented in Part I, it is evident that the total interfacial capacitance (C_T) of low-dimensional carbon electrodes – of which CNTs should be included – strongly depends on the relative contributions of C_D and the electrode quantum capacitance (C_Q). Therefore, in addition to C_D, the CNT curvature can also influence C_Q. Yet, the relative roles of both C_Q and C_D in CNT-based EDLCs have yet to be reported.

In this chapter, the effect of electrode curvature on the interfacial capacitance is investigated. Specifically, three different metallic CNTs [(6,6), (10,10), and (16,16)] electrodes in [BMIM][PF$_6$] IL are studied using combined density functional theory (DFT) and classical MD simulations. The presented analysis aims to understand the relative contributions of C_D and C_Q as compared to pristine graphene electrodes. First, the microstructure of [BMIM][PF$_6$] near the CNT electrodes is investigated by varying the electrode surface charge density using MD simulations, from which the calculated IL distribution is used to evaluate the potential variation and EDL integral capacitance. Then, DFT calculations are employed to estimate the C_Q of the CNTs. Based on the calculation results, the impact of electrode curvature on the capacitive performance, especially the curvature effect on C_D and C_Q in terms of applied voltage, is discussed.

111

7.2 COMPUTATIONAL METHODS
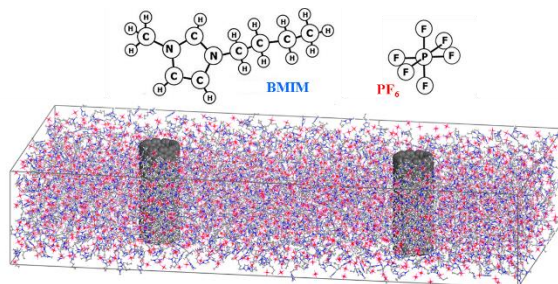
Figure 7.1   Schematic of BMIM, PF_6, and the simulation domain. Two CNTs of the same radius are placed in the simulation domain such that the IL maintains its bulk density in the middle and edges of the domain. White, blue, and grey lines indicate H, N, and C atoms in BMIM while red and pink lines indicate F and P atoms in PF_6, respectively. Periodic boundary conditions are applied in the *x*, *y*, and *z* directions.

MD simulations with the OPLS-AA force field[50,101] were employed to determine the microstructure of [BMIM][PF_6] near the (6,6), (10,10), (16,16) CNTs and graphene electrodes; details on the force field parameters can be found in Ref. 13. As illustrated in Figure 7.1, the CNT/IL simulation domain consists of [BMIM][PF_6] IL pairs surrounding two CNTs with periodic boundary conditions in all three directions; each CNT represents one positive and negative electrode to maintain charge neutrality. Additional details about the simulations (*e.g.*, radius and length of the CNTs, size of the simulation domain, and number of ion pairs) are shown in the Table 7.1. Note that the domain is large enough such that the electrolyte maintains bulk properties at the middle and edges of the domain. For σ = ±6.3 and $\pm12.7\ \mu C/cm^2$, the C atoms of each CNT were assigned uniform atomic charges. The graphene/IL system consists of 312 [BMIM][PF_6] pairs between two graphene

electrodes (34.18×34.53 Å^2) separated by 100 Å. For $\sigma = \pm6.33$ and ±12.67 µC/cm^2, the

C atoms in graphene were also assigned uniform atomic charges.

Table 7.1   Summary of simulation details used in this work.

	Graphene	(16,16) CNT	(10,10) CNT	(6,6) CNT
CNT Radius (Å)	∞	10.88	6.80	4.08
(x, y, z) Simulation Box Dimensions (Å)†	34.18, 34.53, 100	228, 114	212, 106	200, 100
Number of C Atoms in Each Electrode	448	1024	640	384
Number of [BMIM][PF$_6$] Ion Pairs	312	2756	2432	2190
Minimum Distance Between two Electrode Surfaces	100	92.2	92.4	91.8

$\dagger$ All z-dimensions of CNTs are 39.46Å

Each MD simulation was annealed and quenched initially at 1000 K for 0.5 ns

followed by 0.5 ns at 300 K for two cycles, and then further equilibrated for 3 ns at 300 K

using a timestep of 1 fs. Production runs were carried out for 4 ns with atomic positions

recorded every 5 ps. All runs were in the NVT ensemble with the target temperature

controlled by a Nose-Hoover thermostat[60] with a 100 fs damping parameter. All MD

simulations were performed with the Large-scale Atomic/Molecular Massively Parallel

Simulator (LAMMPS) program.[105] MD results reported herein were obtained from the

average of four independent simulations with different initial atomic configurations.

The atomic and electronic structures of pristine graphene and each of the CNTs

were calculated using DFT within the Perdew-Wang 91 generalized gradient

approximation[68] (GGA-PW91), as implemented in the Vienna Ab initio Simulation Package[42] (VASP). The projector augmented wave (PAW) method[69] was employed to describe the interaction between core and valence electrons using a planewave basis set with a kinetic energy cutoff of 400 eV. The CNT structures were modeled using periodic boundary conditions in all three directions; each of the supercells contained 5 unit cells corresponding to 12.33 Å in length and a vacuum space of at least 12 Å (in the radial direction to avoid interactions with the periodic image). For the Brillouin zone integration, a $(1 \times 1 \times 12)$ Monkhorst-Pack k-point mesh[70] was used for geometry optimization and energy calculations while an increased number of k-points was used to ensure convergence for electronic structure calculations. Details on the calculations for pristine graphene can be found in Ref. 13.

7.3 CURVATURE INFLUENCE ON DOUBLE LAYER MICROSTRUCTURE AND CAPACITANCE

The integral EDL capacitance can be obtained from the relationship between excess surface charge density (σ) and potential drop within the EDL (ϕ_D); that is, $C_D = \sigma/(\phi_D-\phi_Z)$, where ϕ_Z is known as the potential of zero charge (PZC). To obtain C_D, we first evaluated the [BMIM][PF$_6$] IL microstructure near (6,6), (10,10), (16,16) CNTs and graphene using MD simulations, as described below.

Figure 7.2 shows the mass density (ρ_m) profiles of cationic BMIM and anionic PF$_6$ near graphene [(a),(d)], the (16,16) CNT [(b),(e)], and the (6,6) CNT [(c),(f)] along the direction normal to the electrode surface with excess surface charge density $\sigma = \pm 12.7$

$\mu C/cm^2$. Each profile exhibits alternating cation/anion layering that dampens away from the electrode, which tends to extend about 2-3 nm before showing bulk-like characteristics. This layering behavior is consistent with previous studies near planar[14,15,107] and cylindrical[85,176] surfaces. We also find that the orientations of IL ions at the interface show a similar behavior near the graphene and CNT electrodes; detailed analysis of the IL orientation near graphene can be found in Ref. 13. Near the positive electrodes [(a)-(c)], PF_6 exhibits three peaks which correspond to F, P, and F atoms, respectively; the electrostatic attraction between the positive electrode and the negatively charged F atoms causes these atoms to orient parallel (concentric in the CNT cases) to the electrode surface. Similarly, the BMIM peak near the negative electrode [(d)-(f)] indicates the tendency of the BMIM ring to align parallel (concentric) to the electrode surface.
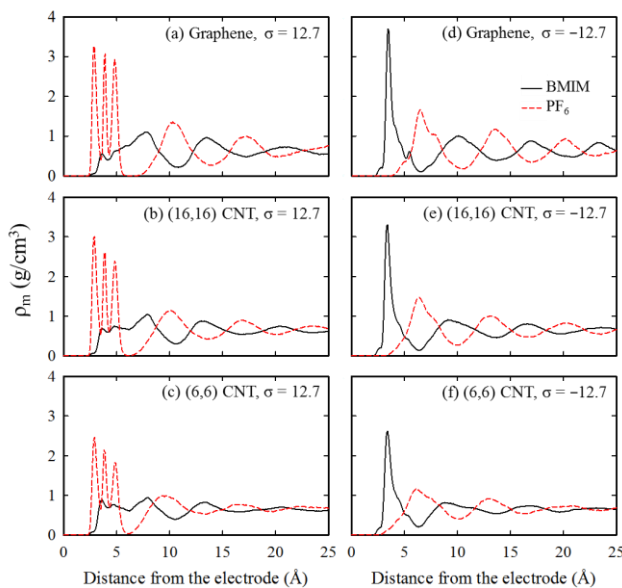
Figure 7.2   Calculated mass density (ρ_m) profiles for BMIM and PF_6 near graphene, (16,16) CNTs, and (6,6) CNTs at the listed σ (in $\mu C/cm^2$) as a function of distance from the electrode surface.
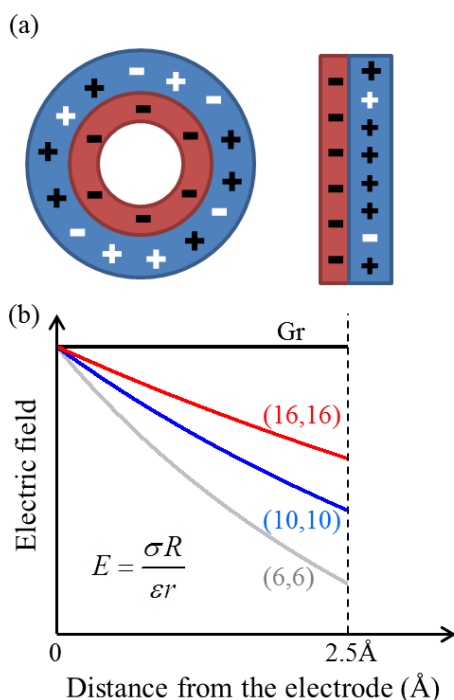
Figure 7.3   (a) Schematic of IL accumulation near a CNT [left] and graphene [right] with the electrodes shown in red. The electrode surface charge is balanced by the counterions represented in black. Excess IL ions in the EDL are represented in white. (b) Schematic of the electric field strength as a function of distance from the electrode for varying electrode curvatures.

As the curvature of the electrode increases [graphene < (16,16) CNT < (6,6) CNT], the oscillations in the mass density profiles appear to dampen. In particular, the counterion mass density peaks become increasingly smaller and more broadened. The peak (average) density of PF_6 in the first layer is 1.52 (3.23) > 1.43 (3.01) > 1.31 (2.46) g/cm^3 near the positively charged graphene > (16,16) CNT > (6,6) CNT. Similarly, near the negatively charged electrodes, the peak (average) density of BMIM in the first layer is 1.15 (3.69) > 1.05 (3.30) > 0.98 (2.62) g/cm^3 for graphene > (16,16) CNT > (6,6) CNT. These observations indicate that the packing density of counterions varies inversely with respect to electrode curvature. In addition, the density of coions is also noticeably influenced by

116

the electrode curvature. Near the positively charged electrodes, the first BMIM coion peak tends to increase from $0.56 < 0.70 < 0.89$ as curvature increases from graphene $<$ (16,16) CNT $<$ (6,6) CNT. Similarly, near the negative electrode, the onset of the PF_6 coion mass density approaches closer to the electrode surface. Both of these observations are indicative of the fact that the segregation of counterions and coions are strongly coupled to, and in fact, diminish with increasing electrode curvature.

The origins of this reduction in ρ_m can depend on a complex combination of factors at the electrode-electrolyte interface. Here, we identify two such factors that may influence the curvature effect on ρ_m: (1) a geometric factor by virtue of the increased volume near curved surfaces and (2) an electrostatic factor by virtue of the reduced electric field strength near curved surfaces. Recall that $\rho_m = m/V$ such that any decrease in mass (m) and/or increase in volume ($V = rA_{cnt}dr/R_{cnt}$ where r is the radius, A_{cnt} is the CNT surface area, and R_{cnt} is the CNT radius) will result in a lower ρ_m. We can expect that V (relative to the electrode surface area) increases with curvature (*i.e.*, decreasing R_{cnt}), and in fact increases linearly with r. Now consider the ideal scenario in which the excess surface charge is perfectly balanced by counterions such that m is independent of curvature [as indicated by the black charges in Figure 7.3(a)] – the reduction in ρ_m, then, is simply due to V increasing. In reality, however, we can expect that additional counterions (and coions) may populate that V, leading to so-called overscreening [as indicated by the white charges in Figure 7.3(a)]. The extent to which these counterions are added, however, is limited by the balance between the electrostatic attraction between the electrode and counterions and the electrostatic repulsion between counterions; stronger electrostatic attraction promotes

117

higher packing densities of counterions by overcoming the electrostatic repulsion. Near curved surfaces, the increase in m due to the increase in V may therefore be mitigated as a result of the reduced electrostatic attraction between the electrode and counterions; according to Gauss's law ($E = -\nabla\phi = \sigma R_{cnt}/\varepsilon_0 r$), at a given σ, the electric field strength E decays more readily at larger curvature [Figure 7.3(b)]. Next, we analyze the space charge variation (ρ_q), mixing parameter (χ), and screening parameter (β) to understand the formation of the EDL in terms of these competing phenomena.
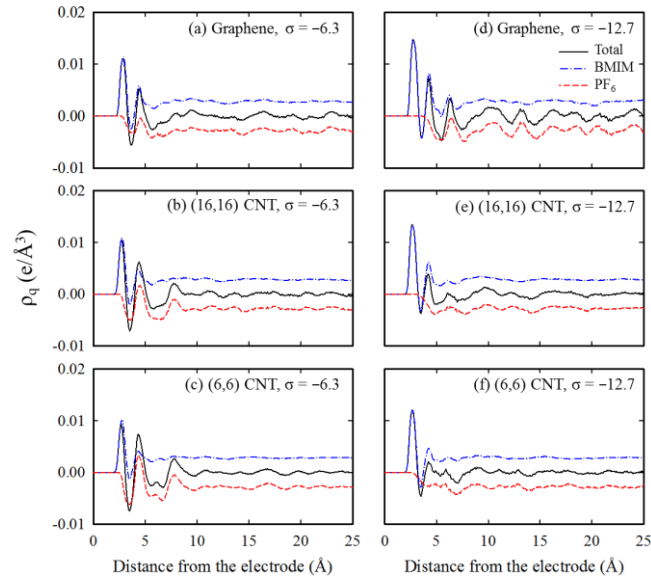
Figure 7.4   Space charge density profiles (ρ_q) for BMIM, PF$_6$, and their sum near graphene, (16,16) CNTs, and (6,6) CNTs at the listed σ (in μC/cm^2) as a function of distance from the electrode surface.

Figure 7.4 shows ρ_q in the IL electrolyte near the negatively charged electrodes at $\sigma = -6.3$ and -12.7 μC/cm^2 (the positively charged electrodes display comparable behavior); ρ_q was calculated based on the distribution of IL atoms, each with fixed atomic charges. When $\sigma = -6.3$ μC/cm^2 [(a)-(c)], the first peak which is associated with BMIM ($\approx$

2.8 Å) has a small tendency to diminish with increasing curvature, deviating from its peak

value of 0.011 $e/\text{Å}^3$ by only 15%. On the other hand, the first valley which is associated

with PF_6 (≈ 3.6 Å) deepens with increasing curvature; in fact, the minimum value decreases

from -0.0056 to -0.0074 $e/\text{Å}^3$. This suggests that the ratio of PF_6 coions to BMIM

counterions in the first layer increases with electrode curvature, which is consistent with

the mass density profiles [Figure 7.2]. However, this mixing behavior becomes less

apparent when $\sigma = -12.7$ $\mu\text{C/cm}^2$ [(d)-(f)]. In this case, the first BMIM peak is more

sensitive to curvature; the peak displays a maximum of 0.015 $e/\text{Å}^3$ in the graphene case

which reduces to 0.012 $e/\text{Å}^3$ in the (6,6) CNT case. This is indicative of the fact that the

BMIM rings, which are planar, can pack more efficiently in a plane than circumferentially.

Upon inspection of the PF_6 charge density, we also observe that the onset of the PF_6

contribution has been shifted to 3.8 Å in the graphene case, which increasingly approaches

the electrode as curvature increases. This suggests that at $\sigma = -12.7$ $\mu\text{C/cm}^2$, the segregation

of BMIM from PF_6 is more prominent, although this segregation is less distinct with

increased curvature.

To quantify this behavior, we calculated χ (the mixing parameter) as a function of

distance from the electrode as shown in Figure 8.5:

$$\chi = \int_0^z \frac{\rho_{\#,counter}(z\prime)}{\rho_{\#,counter}(z\prime) + \rho_{\#,co}(z\prime)} dz' \tag{7.1}$$

where z is the distance from the electrode surface and $\rho_{\#,counter}$ ($\rho_{\#,co}$) is the number density

of the counterion (coion) species. When $\chi = 0.5$, the cumulative number of counterions is

perfectly balanced by the number of coions; however, by integrating up to the bulk-like

region of the finite simulation domain, we expect χ to be slightly larger than 0.5 to account for the net accumulation of counterions in the EDL.
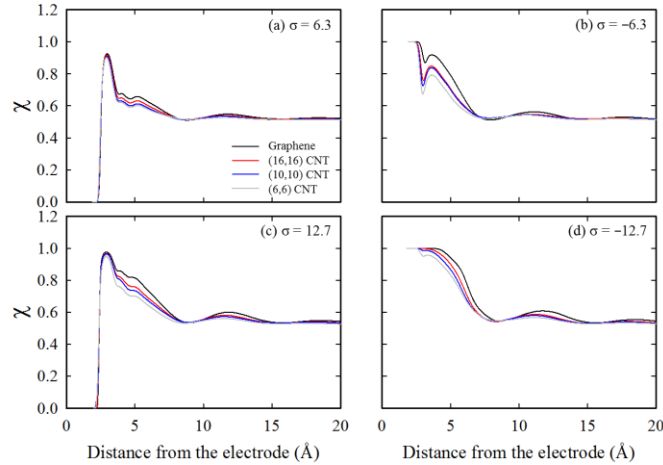
Figure 7.5. Calculated mixing parameter (χ) with varying electrodes at the listed σ (in $\mu C/cm^2$) as a function of distance from the electrode surface.

Near the positively charged electrode [Figure 7.5(a),(c)], the peak (≈ 3.0 Å) value of $\chi = 0.9$ but readily drops towards $\chi = 0.5$. Note, however, that when $\sigma = 6.3$ $\mu C/cm^2$, χ tends to decrease more rapidly than when $\sigma = 12.7$ $\mu C/cm^2$ (which displays better segregation, *i.e.*, larger χ). The negatively charged electrode [Figure 7.5(b),(d)] shows a similar trend, suggesting that in general, the counterions maintain greater segregation from coions as σ increases. In fact, the combination of stronger electrostatic attraction (repulsion) between the electrode and counterions (coions) as well as the finite space at the interface (limited by so-called lattice saturation) necessitates this behavior; that is, to effectively screen the increasing electric field, counterions will increasingly pack together and contribute to coion exclusion.

The influence of electrode curvature on χ seems to strongly depend on both σ and the counterion species. Near the positive electrode at $\sigma = 6.3$ (12.7) $\mu C/cm^2$ [Figure

7.5(a),(c)], the (6,6) CNT case shows a lower χ than the graphene case that deviates by at

most 0.06 (0.12). The negative electrode, on the other hand, displays strong sensitivity to

curvature when $\sigma = -6.3$ µC/cm^2 [Figure 7.5(b)] with χ near the (6,6) CNT deviating by at

most 0.19, indicating a noticeable presence of PF$_6$ coions which is consistent with the

charge density profiles [Figure 7.4(f)]. Interestingly, the curvature dependence of χ is

dramatically mitigated when $\sigma = -12.7$ µC/cm^2 [Figure 7.5(d)] and shows a sensitivity that

is similar to the positive electrode cases.
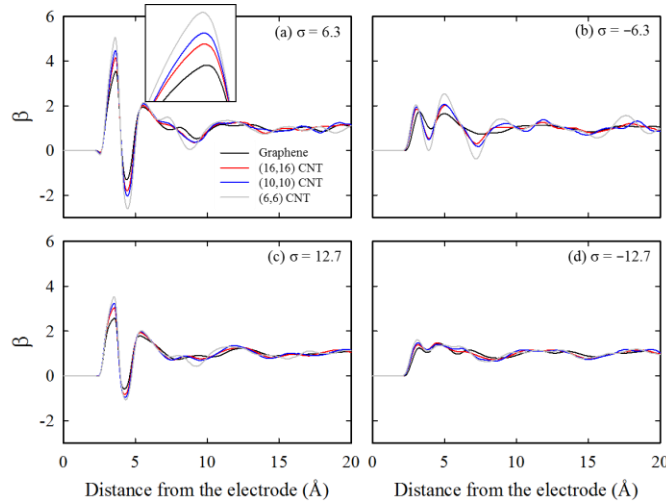
Figure 7.6   Calculated screening parameter (β) with varying electrodes at the listed σ (in
µC/cm^2) as a function of distance from the electrode surface. The inset in (a)
shows the first peak in (a) in greater detail.

Figure 7.6 shows β (the screening parameter) as a function of distance from the

electrode, which is an indication of how effectively the IL screens the electric field ($\beta = 1$

indicates perfect screening), and is calculated from

$$\beta = \begin{cases} -\dfrac{\int_R^r \rho_e(r')r'\,dr'}{\sigma R} & \text{CNT} \\ -\dfrac{\int_0^z \rho_e(z')\,dz'}{\sigma} & \text{Graphene} \end{cases}$$

121

where R is the CNT radius.

Our results show that ILs in the EDL typically overscreen the electric field, in good agreement with previous theoretical studies[13,111]. In fact, the ions near the positive electrode [Figure 7.6(a),(c)] generally tend to exhibit stronger overscreening than those near the negative electrodes. This is primarily due to differences in the size and charge distribution of BMIM and PF_6. Near the positive electrode, PF_6 can tightly pack together due to its "spherical" symmetric shape; the first sharp peak [in Figure 7.6(a),(c)] is attributed to the F atoms which are modeled here with a partial charge of $-0.39\ e$. In contrast, the positive charge in BMIM is spread somewhat broadly over its ring, which can partially account for the smaller peaks near the negative electrode [Figure 7.6(b),(d)]. The peak is also diminished since BMIM does not accumulate as readily as its PF_6 counterpart due to its bulky structure. As a result, PF_6 seems to be more effective at screening the electric field compared to BMIM. Furthermore, the peaks in β tend to diminish as σ increases since the packing density of ions approach an asymptote that is defined by steric limitations. As σ increases further beyond the so-called lattice saturation limit, the first IL layer is expected to have $\beta < 1$.

From Figure 7.6, we also observe that increasing the electrode curvature results in additional screening by the first IL layer. Note that the larger β near the CNTs is an indication of a greater net number of counterions (*i.e.*, those that are not paired with coions) relative to the electrode surface area. This suggests that the counterions prefer to overpopulate the first IL layer due to the increasing availability of space near curved electrodes. Yet despite their larger numbers, these counterions near curved electrodes pack

less efficiently in that space as observed from the mass density profiles [Figure 7.2]. This is due to the aforementioned reduced near-surface electric field strength which effectively weakens the ability of the electrode-counterion attraction to overcome the counterion-counterion repulsion. Because of the availability of space, the enhanced screening of the electrode charge by the counterions near the curved electrodes also facilitates the electrostatic attraction between counterions and coions, which promotes coion mixing at the interface that is consistent with our previous discussion on IL mixing. However, this behavior is also sensitive to the specific ability of the IL counterions to sterically exclude the coions as discussed previously.

From ρ_q (the charge density), the electric potential (ϕ) profiles along the electrode surface normal direction were calculated by solving Poisson's equation, such that ϕ is given by

$$\phi(z) = \begin{cases} -\frac{\sigma R}{\epsilon_0}\ln\frac{r}{R} - \frac{1}{\epsilon_0}\int_R^r \rho_q(r')r'\ln\frac{r}{r'}dr' & \text{CNT} \\ -\frac{\sigma z}{\epsilon_0} - \frac{1}{\epsilon_0}\int_0^z (z-z')\rho_q(z')dz' & \text{Graphene} \end{cases}$$

where ε_0 is the vacuum permittivity.

The calculated potential (ϕ) profiles for graphene and the three CNT cases are shown in Figure 7.7. In each panel, it is evident that the $|\phi|$ increases more rapidly near interfaces with decreasing electrode curvature; for instance, the $|\phi|$ in the graphene case at 2.5 Å from the surface is around 0.5 V (1.0 V) more than that of the (6,6) CNT case when $\sigma = \pm 6.3$ (± 12.7) μC/cm^2. This is primarily attributed to the fact that the electric field strength decays radially in the CNT cases while remaining constant in the graphene case [Figure 7.3].
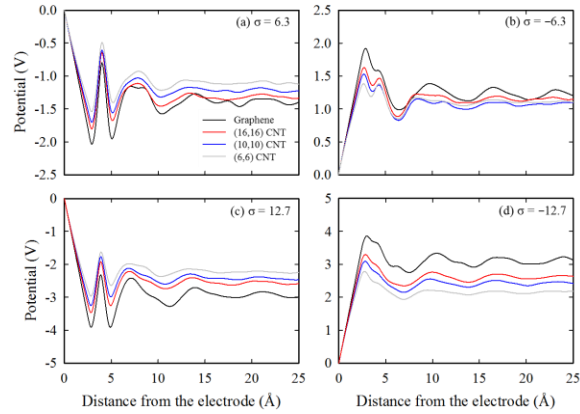
Figure 7.7   Potential (ϕ) profiles with varying electrodes at the listed σ (in μC/cm^2) as a function of distance from the electrode surface. The potential is taken in reference to the electrode surface potential.

Near the positive electrode at σ = 6.3 μC/cm^2 [Figure 7.7(a)], the potential drop across the EDL (ϕ_D = electrode surface potential - the bulk potential) is predicted to range between 1.40 and 1.14 V for the graphene through (6,6) CNT cases, respectively. When σ = 12.7 μC/cm^2 [Figure 7.7(c)], ϕ_D increases and ranges from 2.98 to 2.24 V for the graphene through (6,6) CNT cases. It seems that the differences in ϕ_D are primarily dominated by the deviation in $|\phi|$ in the region between the electrode and IL (due to the aforementioned curvature effect on the electric field strength). On the other hand, as demonstrated earlier [Figure 7.5(a),(c)], the counterion-coion segregation at the electrode-IL interface is minimally influenced by electrode curvature and therefore has little effect on ϕ_D.

Near the negative electrode at σ = −6.3 μC/cm^2 [Figure 7.7(b)], ϕ_D ranges from −1.18 and −1.07 V for the graphene through (6,6) CNT cases, respectively. In contrast to when σ = 6.3 μC/cm^2, the electrode curvature seems to have a reduced effect on ϕ_D, suggesting that the IL distribution in the EDL, and specifically the counterion-coion segregation, causes the curvature effect to be mitigated. This is apparent from the behavior

124

of the potential profiles around 3-4 Å away from the electrode [Figure 7.7(b)] which is the location of the first IL layer. As demonstrated by the graphene case, ϕ drops monotonically in highly rich regions of counterions. For each of the CNT cases, ϕ drops then rises as a small hump before dropping again. Recall that when $\sigma = -6.3$ $\mu C/cm^2$, the segregation between BMIM and PF_6 is reduced near curved surfaces [Figure 7.5(b)], which ultimately lowers the screening of the electric field and increases $|\phi_D|$ for each CNT case such that they are closer to the graphene case. However, the discrepancy in ϕ_D, which ranges from 3.08 to 2.16 for the graphene through (6,6) CNT cases, increases when $\sigma = -12.7$ $\mu C/cm^2$ [Figure 7.7(d)]. Note that the ϕ profiles no longer display a small hump around 3-4 Å away from the electrode, which is consistent with the fact that the curvature effect on χ is greatly mitigated when $\sigma = -12.7$ $\mu C/cm^2$ [Figure 7.5(d)] due to the increased packing density of BMIM while PF_6 is also increasingly excluded.

Figure 7.8 shows the predicted C_D near the positive [(a)] and negative [(b)] electrodes with varying curvature, which tends to have a direct linear relationship. Recall that $C_D = \sigma/(\phi_D-\phi_Z)$ where ϕ_Z is the potential at zero charge, which is nearly zero in all cases studied. Hence, C_D increases with curvature as a result of the decreasing ϕ_D. Near the positive electrode, the C_D at each electrode does not change significantly for both $\sigma = 6.3$ and 12.7 $\mu C/cm^2$. This is due to the ability of PF_6 to pack efficiently, thereby preventing lattice saturation. However, we can expect C_D to drop as σ continues to increase. The C_D is also suppressed when σ goes from -6.3 to -12.7 $\mu C/cm^2$, which results from the lattice saturation by BMIM. Interestingly, the drop in C_D seems to be increasingly mitigated with electrode curvature; the onset of lattice saturation, as discussed previously, is suppressed

near curved surfaces. Curved electrodes, then, can operate at higher ϕ_D before C_D suffers from IL overcrowding effects. However, the specific effect of curvature on C_D can change for different IL pairings; for example, CNT/[EMIM][TFSI] systems were previously predicted to have nearly flat C_D-ϕ_D profiles (over a range of −3 to 3 V).[176] Nonetheless, the enhanced capacitance that results from increasing the electrode curvature remains consistent.
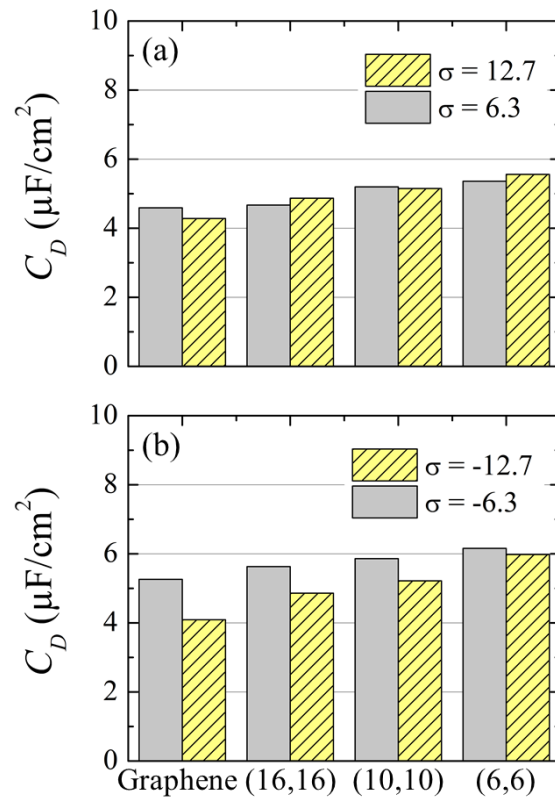
Figure 7.8   Estimated integral EDL capacitance (C_D) near the labeled (a) positive and (b) negative electrodes with the listed σ (in μ/cm^2).

7.4 ELECTRONIC STRUCTURE OF CARBON NANOTUBES
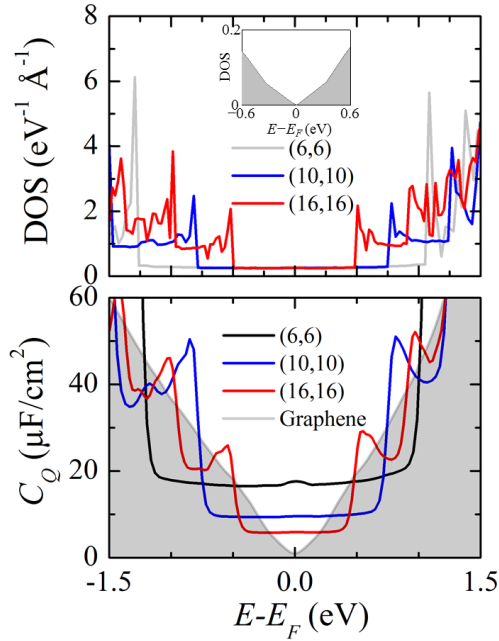
Figure 7.9   (a) The electronic density of states (DOS) and (b) the calculated quantum capacitance (C_Q) of various electrodes as a function of E. $E = 0$ indicates the position of the Fermi level. The inset of panel (a) shows the DOS of graphene.

The DOS of the metallic CNTs were calculated using DFT, as shown in Figure 7.9(a). Note that the DOS is nearly constant (≈ 0.3 eV^{-1} Å^{-1}) in all three cases when $|E| < |E_{vh}|$, where E_{vh} is the energy at the so-called Van Hove singularity (VHS). The E_{vh} also tends to reduce with increasing CNT radius.

Figure 7.9(b) shows the estimated C_Q. The C_Q of the CNTs ($C_{Q,CNT}$) tends to decrease with increasing radius in the flat region near the Fermi level, ranging from 18 to 6 µF/cm^2 in the (6,6) to (16,16) cases. The $C_{Q,CNT}$ profile increasingly converges towards the C_Q of graphene ($C_{Q,Gr}$) with increasing curvature, as expected. Here, we should point

out that the magnitude of $C_{Q,CNT}$ near the VHS peaks may be underestimated due to numerical errors and can exhibit larger variation.

7.5 INTERFACIAL CAPACITANCE OF [BMIM][PF6]/CNT SYSTEMS

The total capacitance (C_T) at the electrode-IL interface can be represented as a series of C_Q and C_D, *i.e.*, $1/C_T = 1/C_Q + 1/C_D$. With the C_Q and C_D values calculated above, we estimated C_T as a function of applied potential ϕ_a (with respect to the potential of the bulk electrolyte, *i.e.*, $\phi_a = \phi_E + \phi_D$) as shown in Table 7.2. The relationship between C_Q and C_D with ϕ_a was obtained through σ; recall that $C_Q/C_D \propto \sigma \propto \phi_E/\phi_D$ (see Chapter 2).

Table 7.2 shows a summary of the calculated $C_T (\phi_a)$ for each electrode case when $\sigma = \pm 6.3$ and ± 12.7 $\mu C/cm^2$. When $\sigma = \pm 6.3$ $\mu C/cm^2$, C_T tends to be sensitive to electrode curvature, yet does not increase directly with curvature. In fact, C_T for both the (16,16) and (6,6) CNT cases is predicted to be less than that of the graphene and (10,10), in contradiction with the trend observed for C_D. This is primarily due to the relatively larger C_Q for the graphene and (10,10) cases when $\sigma = \pm 6.3$ $\mu C/cm^2$. The values of C_Q for the graphene, (16,16), (10,10), and (6,6) CNTs are around 10.5, 10.6, 10.2, and 16.8 $\mu F/cm^2$, respectively; note that the C_Q for the (10,10) CNT is large because of the VHS. When $\sigma = \pm 12.7$ $\mu C/cm^2$, however, C_T follows the same trend observed for C_D; each of the C_Q values exceeds 19 $\mu F/cm^2$ ($>> C_D = 4 - 6$ $\mu F/cm^2$), making the C_D the dominating factor.

Our study clearly suggests that the influence of electrode curvature on the overall performance is strongly dependent on the relative contributions of C_Q and C_D which both

vary with ϕ_a. Here, we should clarify that the electrode curvature is but one important factor that can influence C_Q and C_D; other modifications to the electrode including impurities, functional groups, and structural defects can also alter both C_Q and C_D, which should be further investigated.

Table 7.2   The estimated interfacial capacitance (applied potential) for each electrode at the listed surface charge densities σ (in $\mu C/cm^2$).

	Graphene	(16,16) CNT	(10,10) CNT	(6,6) CNT
6.3	3.2 (2.0)	3.2 (2.0)	3.4 (1.9)	4.1 (1.6)
−6.3	3.5 (−1.8)	3.7 (−1.7)	3.7 (−1.7)	4.5 (−1.4)
12.7	3.3 (3.8)	3.6 (3.5)	3.8 (3.3)	4.2 (3.0)
−12.7	3.3 (−3.9)	3.7 (−3.4)	3.9 (−3.3)	4.5 (−2.9)

7.6 CONCLUSIONS

We investigated the influence of CNT electrode curvature in [BMIM][PF$_6$] IL on the interfacial capacitance (C_T) as a function of applied potential (ϕ_a). Here, C_T is evaluated as the double layer (C_D) and electrode quantum (C_Q) capacitances in series, $i.e.$, $1/C_T = 1/C_D + 1/C_Q$. Using classical MD simulations, we determined the electric double layer (EDL) microstructure of [BMIM][PF$_6$] near each electrode surface at excess surface charge densities $\sigma = 0, \pm6.3$, and ±12.7 $\mu C/cm^2$. We then calculated the potential variation (ϕ) and C_D. Using DFT, we also estimated C_Q from the electronic density of states (DOS) of each electrode.

Our analysis of the EDL microstructure reveals that general features near graphene electrodes, such as the multi-layering of anions/cations and the IL orientations, are consistent near CNT electrodes. However, increasing the electrode curvature tends to reduce the density of IL counterions closest to the electrode, which we find is a consequence of weakened electrostatic attraction between the electrode and counterions. Despite the reduced density, we also find that increasing the electrode curvature enhances the screening of the electrode charge and promotes counterion-coion mixing (*i.e.*, less segregation), although increasing σ abates both of these phenomena.

From the calculation results of ϕ, we observe that the potential drop in the EDL (ϕ_D) diminishes as electrode curvature increases. This reduction is primarily attributed to the fact that the electric field strength decays radially near the CNTs while remaining constant near graphene. When $\sigma = -6.3 \ \mu C/cm^2$, however, the curvature effect is mitigated and is ascribed to the increased mixing of counterions and coions near the CNTs; the reduced segregation effectively lowers the screening of the electric field such that ϕ_D is less sensitive to curvature.

The lower ϕ_D amounts to a larger C_D which tends to increase as electrode curvature increases. When $\sigma = \pm 6.3 \ \mu C/cm^2$, for example, an enhancement of around 18% using (6,6) CNT electrodes is predicted when compared to graphene. As σ increases, we expect C_D to drop due to overcrowding in the EDL, as is observed when $\sigma = -12.7 \ \mu C/cm^2$. Increasing the electrode curvature, however, also increases the available space for IL ions to pack. As a result, the potential window in which C_D does not suffer from lattice saturation effects will be larger near increasingly curved electrodes.

The calculated C_Q for the various CNTs shows a plateau near zero potential with a capacitance that decreases from 18 to 6 μF/cm^2 as curvature decreases from the (6,6) to (16,16) CNT cases. The potential window of the plateau also diminishes with increased curvature, beyond which C_Q is enhanced as a result of the so-called Van Hove singularities (VHS).

The predicted C_T is demonstrated to vary non-monotonically with electrode curvature when $\sigma = \pm 6.3$ μC/cm^2, in contrast with the predicted trend for C_D. This is primarily due to the influence of C_Q, which varies non-monotonically with curvature near the VHS. When $\sigma = \pm 12.7$ μC/cm^2, however, C_T follows the same trend as C_D; each of the C_Q values exceeds 19 μF/cm^2 ($\gg C_D = 4{-}6$ μF/cm^2), making the C_D the dominating factor. Our analysis therefore suggests that any benefit in C_T due to electrode curvature will in fact strongly depend upon the applied potential.

Chapter 8: Ion Confinement Effects in Charged Cylindrical Pores

8.1 INTRODUCTION TO PORE SIZE EFFECT

Conventionally, the search for electrode materials has been directed toward finding materials with good electrical conductivity and specific surface areas larger than commercially-used activated carbons.[25,24,177] For these reasons, carbon nanomaterials, including graphene, carbon nanotubes (CNTs), and carbide-derived carbons (CDCs), have all been recent subjects of interest. However, the work of Chmiola and coworkers[36], and later, Largeot and coworkers[37], used CDC electrodes to show that the areal C can exhibit dramatic improvement with nominal pore widths comparable to the size of the counter-ion. These studies suggest that beyond maximizing the surface area, controlling the pore width offers a new way of increasing C. Exploring this materials development route, however, requires that an atomistic understanding of charge storage when ions are confined in nanopores.

The mechanisms responsible for the enhancement in C has been the study of several theoretical studies; in these works, the electrode is commonly modeled as ideal slit nanopores. A simple phenomenological model theorized that polarizable electrode walls screen long-range electrostatics to allow tight packing of similar ions in the so-called superionic state.[178] Classical molecular simulations of charged nanopores demonstrated consistent behavior in which confined counter-ions were found to maintain elevated density while co-ions were expelled.[179] Several additional factors have been identified as possible ways of tuning C. For example, an oscillatory dependence of C based on the pore

size was revealed by both classical molecular dynamics (MD) simulations[173] and classical DFT simulations[180], which was attributed to interference from overlapping EDLs. In addition to the pore size dependence, classical MD simulations showed that C can be dependent on V and may be maximized when the co-ions were fully expelled before the need for additional counter-ion insertion.[181]

As the primary incentive for supercapacitor adoption is their excellent power capabilities, it is also important to understand the dynamics of ions confined in charged nanopores. This is particularly relevant for ionic liquid (IL) electrolytes, which are solvent-free ions with large electrochemical windows (up to 4 V). In the bulk liquid phase, ILs are known to have high viscosities, due to strong ion-ion interactions[182], which further increase under confinement[183]. Interestingly, molecular simulations suggest that ions can achieve diffusivities that exceed that of their bulk properties when confined in charged pores with both sufficiently narrow widths and large potentials.[184,185] In addition, ion charging behavior has been suggested to be governed by counter-ion electrokinetics, as demonstrated by both non-equilibrium MD simulations[186] and experiments using the electrochemical quartz crystal microbalance method[187].

Beyond slit-pore geometries, limited studies have investigated other pore types despite theoretical evidence of greater charge storage in increasingly confined regions[188]. Ions confined within cylindrical nanopores, such as CNTs, constitute one such extreme case. In the absence of external potential, several experimental studies have investigated the structure of ILs in CNTs with diameters less than 3 nm, which report an interesting adoption of a solid-like phase.[189,190] It may be worthwhile to explore the influence of such

extreme confinement on the capacitive and dynamic behavior of ILs in the presence of external charging.

In this chapter, the charge storage mechanisms of 1-ethyl-3-methylimidazolium (EMIM$^+$) tetrafluoroborate (BF$_4^-$) IL in charged cylindrical nanopores, modeled as CNTs, is investigated using both equilibrium and non-equilibrium molecular dynamics. Here, the capacitance and the dynamics of ion migration are studied based on three primary factors – the pore diameter (D_p), the applied full-cell potential ($\Delta\Phi$), and the charging rate (τ_{chg}).

8.2 COMPUTATIONAL METHODS
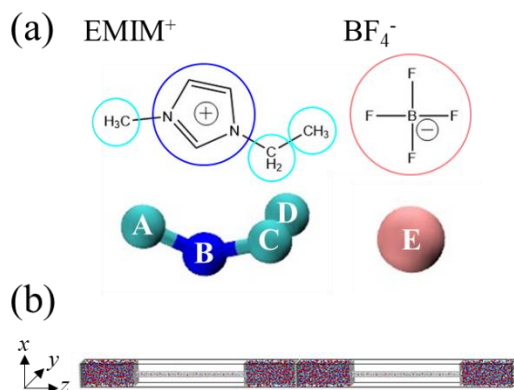
Figure 8.1   (a) Schematic of the EMIM$^+$/BF$_4^-$ ionic liquid studied in this work. Each ion is coarse-grained such that a group of atoms (circled) are modeled as a single interaction site. In particular, the EMIM$^+$ cation is modeled using four interaction centers (shown by the cyan and blue balls labeled A-D) while the BF$_4^-$ anion is modeled using a single interaction center (shown by the pink ball labeled E). (b) Schematic of the simulation domain (periodic in all three directions) consisting of two 16 nm CNT electrodes (shown by grey lines) immersed in ionic liquid (shown by the cyan, blue and pink balls). The length of the simulation domain is 64 nm in the z direction. The two walls of grey balls represent graphene sheets which separate the two electrode domains.

Classical MD simulations were employed using LAMMPS[105] to investigate the microstructure and capacitance of IL molecules confined within fixed CNT electrodes (depicted in Figure 8.1). The IL molecules were described using coarse-grain parameters (Table 8.1) with partitioning shown in Figure 8.1; EMIM$^+$ cations contained four interaction centers while BF$_4^-$ anions contained one interaction center. The LJ parameters were adapted from Ref. 191; the charges (q) were re-scaled following the fashion of Ref. 192 while the zero-energy pair-wise distance (σ) were re-optimized to reproduce experimental density (1.28 g/cm^3) and diffusivity (3.0-3.7×10^{-7} cm^2/s). The bond, angle, and dihedral parameters were adopted from Ref. 56 with the latter case adapted for the OPLS form. The LJ parameters for the electrode carbon atoms were taken from Ref. 193. All LJ and Coulomb energies were calculated using a spherical cutoff radius of 16 Å with the long-range Coulomb energies included by the particle-particle particle-mesh method[54].

While the positions of the electrode atoms were fixed, the charge of each atom was allowed to fluctuate to emulate constant potential surfaces (with $\Delta\Phi$). The charge equilibration (Qeq) scheme[194], which is commonly used in ReaxFF simulations[195], was adapted for this purpose. This method is based on equalization of the electronegativity. Here, the electronegativity of the positive (negative) electrode is rigidly shifted by $-\Delta\Phi/2$ ($+\Delta\Phi/2$); while the IL charges are fixed, the electrode charges are solved iteratively at every timestep with the sum of the total electrode charge constrained to zero. The short-range Coulomb interactions included shielding corrections[195] while the long-range

Coulomb interactions were solved using the fast multipole method[196]. The Qeq parameters

for carbon were extracted from Ref. 197.

Table 8.1   Coarse-grain parameters primarily from Ref. 191 and 56, with q re-scaled
            following the fashion of Ref. 192 and σ re-optimized to reproduce
            experimental density and diffusivity.

Site	ε (kcal/mol)	σ (Å)	q (e)
A	0.157	3.90	0.1733
B	0.643	4.32	0.3741
C	0.141	3.90	0.1647
D	0.157	3.90	0.0679
E	0.339	4.10	-0.7800

The simulation domain consisted of two 16 nm CNT electrodes (grafted onto

graphene) separated by 16 nm of IL for a total size of $3.45 \times 3.42 \times 64$ nm^3 with periodic

boundary conditions in all three directions. When D_p = 0.81 (1.22) nm, 1540 (1640) IL

pairs were included such that the bulk-like IL regions maintained a density of 1.3 g/cm^3.

Two graphene sheets were also included as a physical barrier between the positive and

negative half-cells. The simulations were initially sparse with a length of 80 nm. Initial

equilibration was run for 10 ns under the NVT ensemble with the temperature set to 700 K

as controlled by the Nosé-Hoover thermostat[60] with a 1 ps damping factor and 2 fs time

step; here, electrode charges were kept fixed at zero while the simulation domain was

gradually deformed to its final size. The temperature was then reduced to 300 K and the

system was allowed to equilibrate for another 2 ns. The final equilibration and production

steps followed the procedure described in the manuscript. All reported results were

obtained from the average of four independent simulations with different initial atomic configurations.

8.3 IONIC LIQUID MICROSTRUCTURE CONFINED WITHIN CNTS

A. Neutral CNT electrodes

We first investigate the electrode excess surface charge density (σ_{CNT}) distribution and ionic liquid (IL) microstructure under zero applied bias ($\Delta\Phi = 0$ V). Two CNT electrodes with $D_p = 0.81$ and 1.22 nm are considered with a length (L_p) of 16 nm to maintain large aspect ratios ($L_p \gg D_p$).

Figure 8.2(a) depicts a snapshot of the ions confined within the positive electrode. When $D_p = 0.81$ nm, the ions are observed to form a molecular wire structure with highly partitioned cations and anions. As such, distinct peaks are seen to alternate between cations and anions in the number density (ρ_{ion}) plots shown in Figure 8.2(b). Each ion is caged by its corresponding counter-ion to maintain charge neutrality. In addition, each ion also tends to distinctly polarize the surrounding electrode atoms, as seen by the large oscillations in the σ_{CNT} plot shown in Figure 8.2(d), which serves to screen the ion charge. In contrast when $D_p = 1.22$ nm, the larger internal volume allows the ions to mix axially (a spiral-like configuration); the removal of axial segregation is evident by the suppressed oscillations in the ρ_{ion} profile shown in Figure 8.2(c). The cations also tend to conform close to the electrode walls (Figure 8.2(a)) in order to maximize van der Waals and electrostatic ion-

wall interactions. In the absence of an axially distinct cation-anion segregation, the corresponding charge puddling along the CNT surface is also suppressed (Figure 8.2(d)). Note that in both cases, the average ρ_{ion} of each ion is nearly 2 ion/nm^3; for comparison, the ρ_{ion} in the bulk is around 4 ion/nm^3.
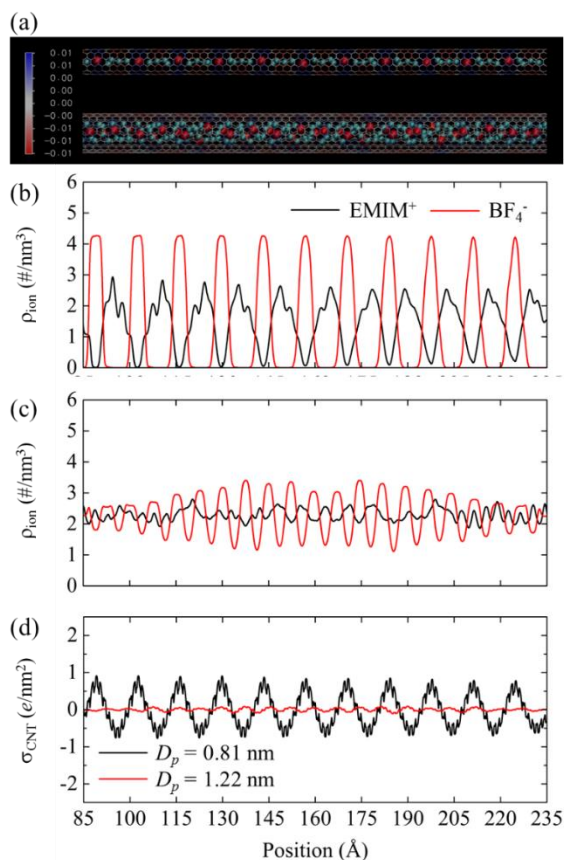
Figure 8.2   (a) Snapshot of the ions confined within the neutral CNT electrodes with the charge per carbon atom (in e) represented as a color map; EMIM$^+$ cations are represented as four bonded cyan balls while BF$_4^-$ anions are represented as one red ball. Ion number density (ρ_{ion}) profiles as a function of distance from the neutral electrode center when (b) the pore diameter $D_p = 0.81$ nm and (c) $D_p = 1.22$ nm. (d) Electrode excess surface charge density (σ_{CNT}) in the axial direction of the electrode.

B. Charged CNT electrodes

Next, $\Delta\Phi = 3$ V is impulsively applied to the electrodes. Here, the electrodes tend to attain full charge after 40 ps but are allowed to equilibrate for 4 ns before statistics are extracted over additional 2 ns trajectories. Interestingly, as depicted in Figure 8.3(a), distinct differences in the IL microstructures appear when comparing the two electrode diameters. Most notably, the IL distribution along the axial direction of the positive electrode is heterogeneous when $D_p = 0.81$ nm and homogeneous when $D_p = 1.22$ nm. For simplicity, the negative electrode is not depicted but has qualitatively similar features as discussed below.

In the more confined case ($D_p = 0.81$ nm), a region containing both EMIM$^+$ co-ions and BF$_4^-$ counter-ions develops within the center of the positive electrode. As seen in Figure 8.3(b), the average ρ_{ion} of both counter-ions and co-ions tends to be around 4 ion/nm^3 which is comparable to bulk values. Beyond this central region, the electrode is completely populated by BF$_4^-$ counter-ions with an initially large ρ_{ion} around 16 ion/nm^3 that tapers down to around 6 ion/nm^3 near the entrances to the pore (Figure 8.3(b)). In comparison, the nominal packing of EMIM/BF$_4$ in its monoclinic crystal phase at 173 K is 8.6 ion/nm^3.[198] We therefore find that the anions can be driven into a higher density packed state in order to screen the surface charge despite the anion-anion repulsion. Note that the observed density should be related to the anion size and its compactness. The influence of the ion size can be highlighted by the behavior in the negative electrode; although similar IL packing behavior is observed, the maximum ρ_{ion} achieved by the EMIM$^+$ counter-ion is

139

smaller ($\cong 6$ ion/nm^3), likely due to the fact that the bulkiness of the cation facilitates the screening of the electrode charge compared to the compact and nearly spherical anion, while also restricting the ability to densely pack the ions together.
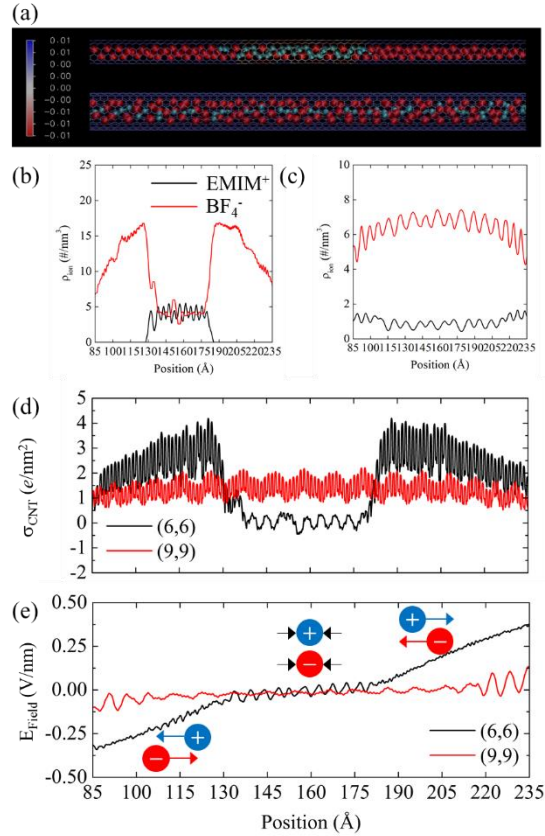
Figure 8.3 (a) Snapshot of the ions confined within the positive CNT electrodes when the applied full-cell potential is 3V with the charge per carbon atom (in e) represented as a color map; EMIM$^+$ cations represented as four bonded cyan balls while BF$_4^-$ anions represented as one red ball. Ion number density (ρ_{ion}) profiles as a function of distance from the positive electrode center when (b) the pore diameter $D_p = 0.81$ nm and (c) $D_p = 1.22$ nm. (d) The corresponding electrode excess surface charge density (σ_{CNT}) along the axial direction with (e) the computed total electric field (E$_{field}$) in the axial direction.

In the less confined case ($D_p = 1.22$ nm), the microstructure appears to be comparatively more homogeneous in the axial direction. Figure 8.3(a) shows that the BF$_4^-$

counter-ions form a sheath-like structure that both screens the electrode charge and shields the EMIM$^+$ co-ion molecular chain that forms along the axis of the pore. The counter-ion essentially forms a one to two molecule thick electric double layer which is possible due to its small Debye length of less than 2 Å. However, we should note that the center of the pore exhibits slight counter-ion accumulation (co-ion depletion), such that the ρ_{ion} of BF$_4^-$ (EMIM$^+$) tapers (rises) from 6 ion/nm^3 (1 ion/nm^3) in the center of the pore to 5 ion/nm^3 (1.5 ion/nm^3) toward the entrances of the pore. In addition, the influence of ion size once again manifests in the negative electrode. Namely, the compact BF$_4^-$ co-ions tend to remain trapped within the center of the pore. However, the EMIM$^+$ counter-ion still tends to sheath the co-ions, thereby shielding both the anions and the negatively charged surface.

Figure 8.3(d) compares the σ_{CNT} of the two different electrode cases when $\Delta\Phi = 3$ V. It is evident that the two profiles are consistent with their respective IL packing behavior in the axial direction. The $D_p = 1.22$ nm case, for example, exhibits an expectedly homogeneous profile in the axial direction with slight accumulation in the center of the pore. Similarly, the $D_p = 0.81$ nm case exhibits a heterogeneous profile with increasing σ_{CNT} from the pore entrance toward the center that is consistent with the aforementioned counter-ion concentration gradient. However, σ_{CNT} abruptly diminishes to neutral charge along the central IL region that contains zero net ionic charge. This suggests that injected charge carriers must be stored outside of this region, which henceforth will be called the depletion region; here, the length of the depletion region (L_d) is 4.1 nm when $D_p = 0.81$ nm as seen in Figure 8.3(d). Note that while the trans-axial electric field outside of the depletion region (Figure 8.3(e)) serves as an inward driving force for counter-ions, it

appears that a steric barrier prevents the counter-ions from penetrating into the depletion region.

The resultant double-layer capacitance ($C_{DL,cell}$) of the two-electrode cell, calculated from the ratio of the charge in one electrode to $\Delta\Phi$, is estimated to be 11.7 $\mu F/cm^2$ and 8.8 $\mu F/cm^2$ for $D_p = 0.81$ and 1.22 nm, respectively. We note that while our scheme does not control the half-cell potential, we can expect the potential drop between the positive electrode surface and the bulk electrolyte to be slightly larger than that of the negative electrode given the denser accumulation of counter-ions in the former case. Indeed, the calculated potential drops in the positive and negative half-cells are 1.9 and 1.1 V, respectively, based on the numerical solution to the three-dimensional Poisson equation with the additional of short-range Coulombic screening. Nonetheless, we report the full-cell capacitance to avoid any misunderstanding.

8.4 INFLUENCE OF APPLIED POTENTIAL ON CAPACITANCE

Next, we investigate the influence of different (impulsively applied) $\Delta\Phi$ on the computed $C_{DL,cell}$ of the two different electrodes. As seen in Figure 8.4(a), it is clear that the electrode with smaller diameter tends to have a larger $C_{DL,cell}$. This is consistent with both experimental[36,37] and theoretical[173,179,180] (based on slit pores) observations that suggest that the capacitance can be enhanced with sub-nanometer pores. In both cases, we find that $C_{DL,cell}$ diminishes with increasing $\Delta\Phi$, thereby mitigating the predicted enhancement at large $\Delta\Phi$. Previous simulations of graphene/IL interfaces reported a similar

dependence of $\Delta\Phi$ on C, which is attributed to the increasing saturation of ions in the EDL.[13] In these cases, the diminishment is gradual and continuous. However, an anomalously distinct reduction (nearly 40%) of $C_{DL,cell}$ is observed between $\Delta\Phi = 1$ and 2 V in the $D_p = 0.81$ nm case, in contrast to the expected behavior in the $D_p = 1.22$ nm case.
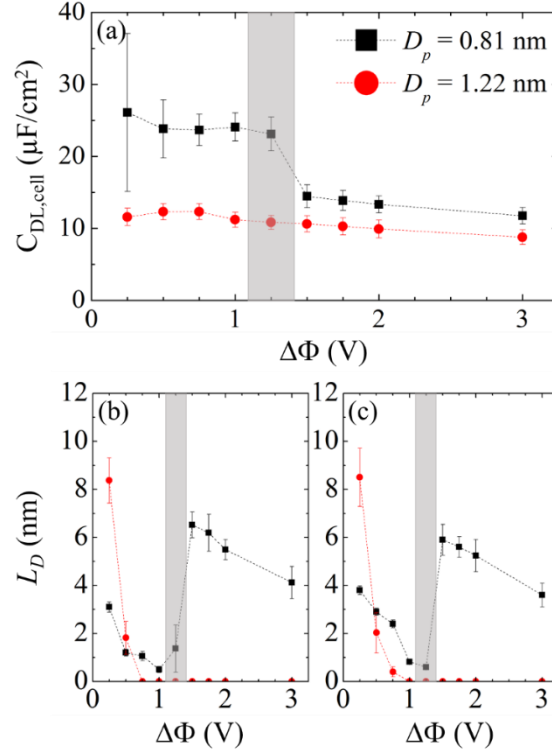
Figure 8.4   (a) Areal integral capacitance of the full-cell ($C_{DL,cell}$ that is normalized to the surface area of one electrode) with respect to the applied full-cell potential ($\Delta\Phi$) which is instantaneously applied. Length of the depletion region (L_D) as a function of $\Delta\Phi$ at the (b) positive and (c) negative electrode. The shaded region in all three panels depicts the transition between migration and stagnation, as discussed in the main text.

To explain these observations, we assess the possible development of a depleted region. Figure 8.4 shows the computed L_D for both electrode cases on the positive (Figure 8.4(b)) and negative (Figure 8.4(c)) sides, respectively. Two distinct regimes become

immediately obvious. The first is the low potential regime ($\Delta\Phi < 1$ V) in which both $D_p = 0.81$ and 1.22 nm cases exhibit a reduction in L_D as $\Delta\Phi$ increases. As discussed in depth later, the repulsive electrostatic interactions between the electrode walls and co-ions drives their expulsion from the pore while the electrode charge and counter-ions migrate from the pore entrance to center. However, a transition occurs between $\Delta\Phi = 1$ and 1.5 V such that when $\Delta\Phi > 1.5$ V, L_D abruptly increases in the $D_p = 0.81$ nm case before gradually decreasing with increasing $\Delta\Phi$. Here, the large density of counter-ions entering the pore prevents co-ion expulsion, such that a depletion region forms within the center of the pore. While similar behavior is seen in the $D_p = 1.22$ nm case, the pore remains large enough for the counter-ions to screen the interaction between the trapped co-ions and electrode wall. Nonetheless, both electrode cases exhibit a transition between co-ions migrating out of the pore and co-ions remaining stagnated inside the pore.

Comparing the positive to negative electrodes, the trend in L_D appears to be qualitatively similar. The major difference is that in the latter case, L_D tends to be larger than the former case when $\Delta\Phi < 1$ V and smaller when $\Delta\Phi > 1.5$ V. This is likely related to the difference in the counter-ion size. In the low potential regime ($\Delta\Phi < 1$ V), the bulky $EMIM^+$ counter-ion in the negative electrode can screen the electrode charge more efficiently than the compact BF_4^- counter-ion in the positive electrode, which can help explain the observation of a larger L_D. By the same argument, the bulkiness of the $EMIM^+$ counter-ion may also facilitate the compression of the depletion region in the high potential regime ($\Delta\Phi > 1.5$ V), thereby resulting in a smaller L_D.

8.5 TRANSIENT MIGRATION OF IONS DURING CHARGING

To understand the molecular origins of the observed transition between co-ion migration and stagnation, we investigate the transient behavior of the cations, anions, and electrode charge throughout the pore with $D_p = 0.81$ nm within the first 100 ps after $\Delta\Phi$ is impulsively applied. We first compare two cases in the low-potential ($\Delta\Phi = 0.5$ V) and high-potential ($\Delta\Phi = 3$ V) regime, which are depicted by color maps in Figure 8.5. For simplicity, we once again focus only on the positive electrode.
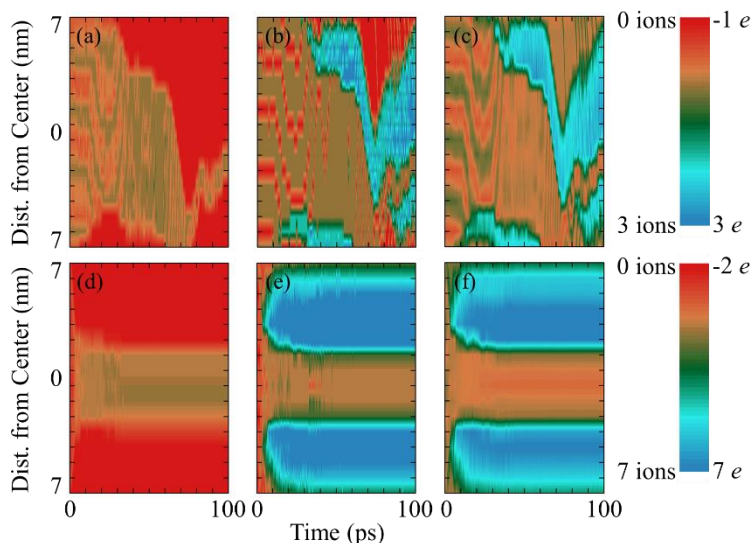
Figure 8.5   Color maps depicting the variation in time of the (a) number of cations, (b) number of anions, and (c) electrode charge (in e) along the length of the positive electrode when the applied full-cell potential is 0.5 V. For comparison, the variation in time of the (d) number of cations, (e) number of anions, and (f) electrode charge (in e) along the length of the positive electrode when the applied full-cell potential is 3 V. The plots have a spatial resolution of 0.5 nm and temporal resolution of 20 fs. The electrode diameter is 0.81 nm.

Within the first 10 ps when $\Delta\Phi = 0.5$ V is applied, the color maps of the $EMIM^+$ co-ion (Figure 8.5(a)) and BF_4^- counter-ion (Figure 8.5(b)) display an axial segregation

145

similar to that of the neutral case; the electrode is polarized accordingly (Figure 8.5(c)). Throughout the next 25 ps ($10 < t < 35$ ps), a clear electrokinetic flow appears in which the still segregated ions travel both inward and outward throughout the electrode; notice that the pore entrance starts to become rich in both counter-ions and positive electrode charge. In the next time interval when $35 < t < 70$ ps, the co-ions and counter-ions aggregate in the center of the pore and collectively migrate toward one pore entrance. At the other pore entrance, a rich counter-ion/electrode charge front develops and migrates inward toward the center of the pore. The inherent asymmetry of the ion flow from one pore end to the other is indicative of a trans-axial potential, which results in ion migration similar to that of electro-osmotic flow in channels with overlapped EDLs[199]. Once the collective co-ions and counter-ions reach the pore entrance when $t > 70$ ps, they are expelled from the electrode. However, the removal of co-ions enables the addition of new counter-ions which eventually create another counter-ion rich front that migrates toward the pore center. As a result, the collective aggregate of co-ions and counter-ions that remain in the pore are gradually pushed back toward the pore center; in this case, these ions continue to drift for nearly 1.5 ns. The $\Delta\Phi = 3$ V case is far simpler (Figure 8.5(d)-(f)). Within the first 10 ps, a rich counter-ion front develops from both pore entrances and quickly migrates toward the center of the pore. In this case, the co-ions and counter-ions that were originally inside the pore are compressed together as the rich counter-ion front migrates inward. These ions continue to migrate for another 400 ps as the two counter-ion fronts equilibrate.
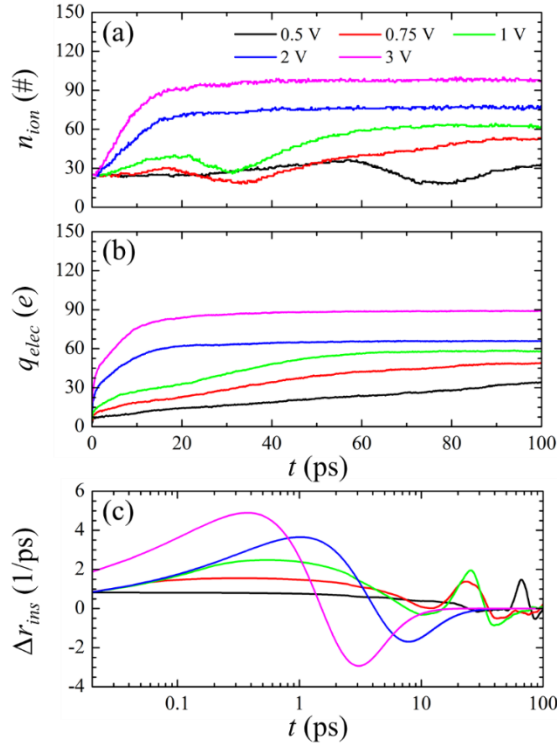
Figure 8.6   (a) Total number of confined ions (n_{ion}), (b) total excess surface charge (q_{elec}), and (c) the difference in the rate of electrode charge insertion and ion insertion (Δr_{ins}) within the positive electrode as a function of time (t) when the listed full-cell potential is applied starting 0 V. The electrode diameter is 0.81 nm.

Now that a general idea of the ion transport behavior is established, we next consider a wider range of $\Delta\Phi$. As seen in Figure 8.6, we simplify our analysis by computing the total sum of ions (n_{ion}) and electrode charge (q_{elec}) within the positive electrode as a function of t. In the low-potential regime ($\Delta\Phi < 1$ V), n_{ion} initially increases, then decreases, and finally readily increases; the point at which n_{ion} begins to decrease indicates when co-ion/counter-ion clusters are expelled from the pore. Interestingly, the time of ion expulsion occurs at increasingly lower t as $\Delta\Phi$ increases. In addition, the rate of ion insertion ($r_{i,ins} = \partial n_{ion}/\partial t$) also increases as $\Delta\Phi$ increases. Given that the ion flux into the pore also increases

147

with $\Delta\Phi$, we attribute the more rapid expulsion of the co-ion/counter-ion cluster to the faster counter-ion front that develops to push the clusters out. In the high-potential regime ($\Delta\Phi > 1.5$ V), we find that both n_{ion} and q_{elec} exhibit similar behavior in which both initially increase before saturating, which is consistent with nearly immediate filling of the pore by counter-ions. On closer inspection, the rate of q_{elec} insertion ($r_{e,ins} = \partial q_{elec}/\partial t$) is observed to be larger than $r_{i,ins}$ within the first 5 ps, which we quantify in Figure 8.6(c) as Δr_{ins} ($= r_{e,ins} - r_{i,ins}$). Here, the large peaks observed in Δr_{ins} suggest that when the electrode surface current far exceeds the ionic current, counter-ion filling dominates the ion transport dynamics and thereby restricts co-ion expulsion. In contrast when the electrode current is comparable to the ionic current, as in the $\Delta\Phi < 1$ V cases, both counter-ion and co-ion transport contribute to the overall ion transport dynamics; note that the observed spikes when $t > 10$ ps are associated with the cluster expulsion event. This illustrates that in addition to the magnitude of $\Delta\Phi$, τ_{chg} may be important.

The influence of τ_{chg} is investigated next by linearly varying $\Delta\Phi$ from 0 to 3 V over τ_{chg}, after which the system is allowed to equilibrate for 2 ns. Figure 8.7 shows the computed $C_{DL,cell}$ and L_D as a function of τ_{chg} when $D_p = 0.81$ nm. At fast charging rates ($\tau_{chg} < 40$ ps), $C_{DL,cell}$ dramatically decreases with decreasing τ_{chg}. Here, we find that the suppression in $C_{DL,cell}$ is commensurate with a larger L_D that can be as large as 5 nm, which effectively makes 30% of the electrode inaccessible for charge storage. However, an abrupt change in both $C_{DL,cell}$ and L_D is predicted when $\tau_{chg} > 40$ ps. At these slow charging rates, $C_{DL,cell}$ saturates around 14 μF/cm^2 while L_D is less than 1.5 nm. Note that even at a large

τ_{chg} of 10 ns, some co-ions remain trapped within the pore. Nonetheless, these results suggest that the rate capability of these subnanometer electrodes is dictated by the rate at which co-ions (and their paired counter-ions) are removed from the pore.
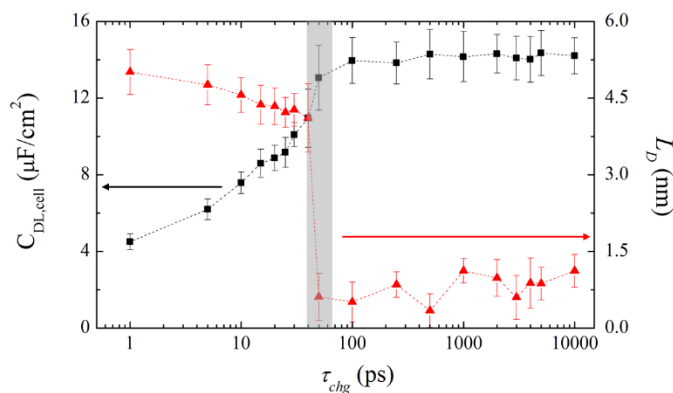
Figure 8.7   The influence of charging time (τ_{chg}) on (left) the full-cell capacitance ($C_{DL,cell}$ in black squares) and (right) length of the depleted region (L_D in red triangles) at the positive electrode with diameter 0.81 nm when the applied full-cell potential is 3 V. The shaded region depicts the transition between migration and stagnation, as discussed in the manuscript.

8.6 CONCLUSIONS

To summarize, we investigated the capacitance of ionic liquid confined within charged cylindrical nanopores with diameters 0.81 and 1.22 nm using non-equilibrium molecular dynamics. While we find that the capacitance is expectedly larger using the narrower pore, an interesting inhomogeneity is observed as well. The smaller pore is found to develop a so-called depletion region in the center of the pore, in which an equal number of co-ions and counter-ions remain trapped. As this depletion region cannot accommodate excess charge, a significant fraction of the electrode does not participate in charge storage.

Molecular analysis during the transient charging regime attributes the development of the depletion region to the rapid over-filling of counter-ions into the pore. In addition, the length of the depletion region is found to be strongly dependent on the competition between forced electro-kinetic flow and natural ion convection, which in turn can be controlled by the magnitude of the applied potential or the charging rate (or essentially, the scan rate). It is evident that such phenomena may be related to the experimentally observed capacitance fading at high rates. Due to the limited scope of this work, however, many other factors remain largely unexplored; these factors can include the possible non-uniformity of the pore structure, the geometry of different ions (including size, flexibility, and charge distribution), the presence of solvent molecules, different surface chemistries with a resultant surface charge redistribution, and possible electrolyte decomposition due to charge localization (especially at the depletion region interface). Nonetheless, these findings highlight the importance of investigating the transition between the migration or stagnation of confined ions for the design of future nanoporous materials for supercapacitor applications.

Chapter 9: Pore Dispersity and Ion Kinetics in Nanoporous Carbons

9.1 INTRODUCTION TO NANOPOROUS CARBON

Expanding on the work presented in Chapters 7 and 8, realistic nanoporous carbon (NPCs) electrodes immersed in ionic liquid are now considered. The development of NPCs is motivated by experimental work[36,37] on carbide-derived carbons (CDCs) that suggested that the areal capacitance (C_{ar}) exhibits dramatic enhancement when the nominal pore width (W_p) is comparable to the size of the electrolyte ions. The subject, however, remains somewhat controversial as others have reported a clear independence of C_{ar} with respect to W_p.[200] The main basis for this claim is that the commonly used Brunauer–Emmett–Teller (BET) method of characterizing the surface area may result in misleading C_{ar} values. Interestingly, while the specific capacitance (C_{sp}) should be a more reliable metric, no such trends have been reported based on C_{sp}. Nonetheless, several theoretical studies explain the discrepancy in C_{ar} by showing that the maximum C_{ar} is only achieved at certain potentials for a given W_p.[181,201] These authors postulate that the absence of a clear W_p dependence in Ref. 200 is related to broad pore dispersity which may be common in most NPC materials. However, the exact impact of pore dispersity on the capacitance remains unclear.

In this chapter, a resolution to the C_{ar} debate, as well as insights into C_{sp}, is attempted by investigating the role of pore dispersity, in both size and shape, on C_{ar} and C_{sp}. Here, the dynamic charge storage behavior of 1-ethyl-3-methylimidazolium (EMIM) tetrafluoroborate (BF4) ionic liquid (IL) confined within realistic nanoporous carbon (NPC) electrodes is studied using non-equilibrium molecular dynamics simulations.

151

9.2 COMPUTATIONAL METHODS

A. Electrode Structure Generation

Initial NPC structures were generated using the Mimetic model presented in Ref. 202. Simulation domains were $4.55 \times 4.55 \times 20$ nm^3 (using periodic boundary conditions) with initial number densities of 0.05, 0.054, and 0.06 #/Å^3 in a *fcc* lattice configuration. Temperatures were quenched from 20000 K to 700 K under the NVT ensemble using the Nosé-Hoover thermostat[60] with a quench time of 1.6 ns and timestep of 0.07 fs. After generation, 2 nm of carbon atoms were removed from each end to make the structures non-periodic in the *z* direction. Then, unphysical and dangling carbons were removed from the system after which hydrogen atoms were attached to the remaining *sp* carbon. The volumes were then relaxed in the *xy* direction under the NPT ensemble using a Nosé-Hoover barostat/thermostat[60] and AIREBO potential[203] for 500 ps with a timestep of 1 fs. The final *xy* dimensions of the NPC-12, NPC-10, and NPC-9 electrodes were 4.54×4.54, 4.57×4.57, and 4.58×4.58 nm^2, respectively.

B. Force Field

The ionic liquid was described using a coarse-grained approach such that EMIM$^+$ and BF$_4^-$ were reduced to four and one interaction centers, respectively, as depicted in Figure 9.1. The non-bonding parameters were adapted from Ref. 191 as summarized in Table 9.1; the charges (*q*) were re-scaled following the fashion of Ref. 192 while the zero-energy pair-wise distance (σ) were re-optimized to reproduce experimental density and

diffusivity. The bond, angle, and dihedral parameters were adopted from Ref. 56 with the latter case adapted for the OPLS form. The LJ parameters for the electrode carbon and hydrogen atoms were taken from Ref. 193. All LJ and Coulomb energies were calculated using a spherical cutoff radius of 16 Å with the long-range Coulomb energies included by the particle-particle particle-mesh method[54].

The charge of each electrode atom was allowed to fluctuate to emulate constant potential surfaces (with $\Delta\Phi$). We adapted the charge equilibration (Qeq) scheme[194], based on electronegativity equalization, which is commonly used in ReaxFF simulations[195]. Here, the electronegativity of the positive (negative) electrode is rigidly shifted by $-\Delta\Phi/2$ ($+\Delta\Phi/2$) and the charges are solved iteratively with the sum of the total electrode charge constrained to zero. The short-range Coulomb interactions included shielding corrections[195] while the long-range Coulomb interactions were solved using the fast multipole method[196]. The Qeq parameters for carbon and hydrogen were adopted from Ref. 197.

Table 9.1   Coarse-grain parameters primarily from Ref. 191 and 56, with q re-scaled following the fashion of Ref. 192 and σ re-optimized to reproduce experimental density and diffusivity.

Site	ε (kcal/mol)	σ (Å)	q (e)
A	0.157	3.90	0.1733
B	0.643	4.32	0.3741
C	0.141	3.90	0.1647
D	0.157	3.90	0.0679
E	0.339	4.1	-0.7800

C. Molecular Dynamics
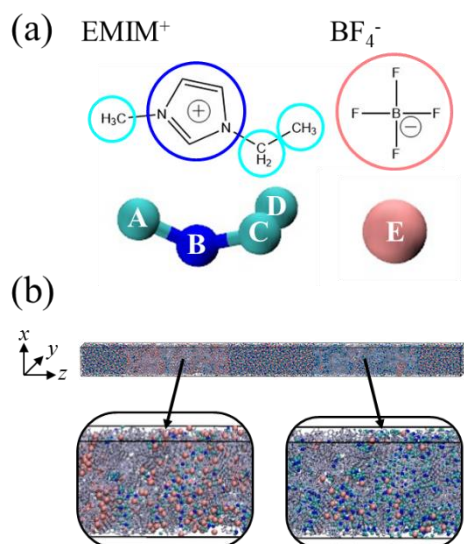
Figure 9.1 (a) Schematic of the EMIM/BF$_4$ ionic liquid studied in this work. Each ion is coarse-grained such that a group of atoms (circled) are modeled as a single interaction site. In particular, the EMIM$^+$ cation is modeled using four interaction centers (shown by the cyan and blue balls labeled A-D) while the BF$_4^-$ anion is modeled using a single interaction center (shown by the pink ball labeled E). (b) Schematic of the simulation domain (periodic in all three directions) consisting of two 16 nm porous carbon electrodes (shown by grey lines) immersed in ionic liquid (shown by the cyan, blue and pink balls). The length of the simulation domain is 60 nm in the z direction.

All MD simulations were performed using LAMMPS[105] and consisted of two fixed 16 nm electrodes separated by 14 nm of electrolyte, as seen in Figure 9.1, for a total length of 60 nm in the z direction with periodic boundary conditions in all three directions; the cross sectional areas were consistent with that of each electrode. Each simulation was initially sparse with a z length of 90 nm and 4164 IL pairs that were randomly distributed outside the electrodes. Initial equilibration was run for 10 ns under the NVT ensemble with a temperature of 850 K controlled by a Nosé-Hoover thermostat[60] with a 1 ps damping factor and 2 fs timestep. During this period, the electrode atoms were kept rigid with null

154

charge and moved linearly to their final positions; the simulation domain was also linearly deformed to its final length. A second equilibration step was performed at $\Delta\Phi = 0$ V for 10 ns with the electrode charges updated every 100 fs and the temperature gradually decreased from 850 K to 300 K. Fixing the temperature at 300 K, charges were updated every 2 fs while the systems were further equilibrated over 1 ns. Similarly, a $\Delta\Phi = 3$ V was impulsively applied and equilibrated for 2 ns. Finally, molecular trajectories were extracted every 5 ps over a production run of 4 ns to compute the DoC profiles.

To prepare the capacitance calculations, each simulation underwent pre-cycling by linearly varying $\Delta\Phi$ between 0 and the target $\Delta\Phi$ for at least 3 charge and 2 discharge ramps with 1 ns in each direction (total pre-cycling time was at least 5 ns); the pre-cycling was considered complete when the largest and smallest peak-to-peak values of the electrode charge deviated by less than 1% from the previous cycle. Discharge production runs were carried out by first holding $\Delta\Phi$ for 250 ps before allowing $\Delta\Phi$ to linearly decrease to 0 V over 1 ns; molecular trajectories were extracted every 2 ps.

All reported results were extracted from the average trajectories from 4 independent simulations with different initial atomic configurations.

9.3 NANOPOROUS CARBON STRUCTURAL CHARACTERIZATION

As depicted in Figure 9.1, we consider a simulation domain that emulates a two-electrode supercapacitor cell filled with 1-ethyl-3-methylimidazolium ($EMIM^+$) tetrafluoroborate (BF_4^-) ionic liquid (IL), modeled using a coarse-grain force field (see

Methods). The nanoporous carbon (NPC) electrodes were generated to ensure sp^2 hybridization with hydrogen-passivated edges (see Methods), which are hereafter denoted as NPC-12A, NPC-10A, and NPC-9A according to their nominal pore sizes. Table 9.2 summarizes their structural properties, as characterized using a Monte Carlo sampling technique[204]. We should note that these properties were based on spherical sampling probes with a radius of 2.25 Å to emulate adsorption by N_2 molecules.

Table 9.2.   Summary of the structural characteristics$^\perp$ of the three nanoporous carbon electrodes studied in this work. All pore geometry analysis was performed using a Monte Carlo sampling approach described in Ref. 204.

	NPC-12A	NPC-10A	NPC-9A
Density (ρ), g/cm^3	0.96	1.03	1.09
Surface Area (S), m^2/g	1072	836	750
Pore Volume (V_p), cm^3/g	0.185	0.121	0.093
Average Pore Size (W_p), Å	12.4	10.8	9.6
Hydrogen Content, at.%	8	10	11

$^\perp$ Using a spherical probe with a comparable adsorption cross-section to N_2 (~ 2.25 Å)

In each simulation, the charge equilibration scheme (see Methods) is used to emulate constant potential surfaces with an imposed potential difference ($\Delta\Phi$) with reference to the surface potentials of the two electrodes. To characterize the electrolye-electrode interface, we adopt the degree of confinement (DoC) definition as described in Ref. 188; briefly, the DoC quantifies the solid-angle fraction of the counter-ion/electrode coordination shell that is occupied by electrode atoms. Figure 9.2 depicts the DoC of ions within the NPG-9A electrodes when $\Delta\Phi = 0$ and 3 V. Upon charging, it is evident that the EMIM$^+$ cation (Figure 9.2(a)) tends to shift toward high DoC sites (*i.e.*, confined carbon

pores) when the electrodes are negatively polarized and low DoC sites (*i.e.*, edges and planes) when the electrodes are positively polarized. In other words, these ions expectedly seek highly-confined electrode regions when acting as a counter-ion and minimally-confined electrode regions when acting as a co-ion. Interestingly, the BF_4^- anion behavior (Figure 9.2(b)) is consistent with the exception of its counter-intuitive tendency to occupy highly-confined sites when acting as a co-ion. This is likely related to the small and compact nature of the anion, which we will discuss in detail later.
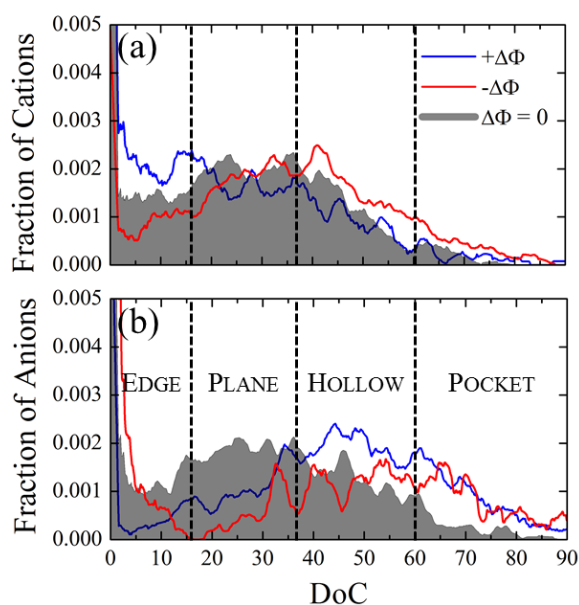
Figure 9.2   Distribution of (a) cation and (b) anion degrees of confinement (DoC) within the NPG-9A electrode when the full-cell applied potential ($\Delta\Phi$) is 0 and 3 V. Dashed lines depict the boundaries that distinguish edge, plane, hollow, and pocket sites.

In discussions below, we generalize the electrode regions into five categories – edge (DoC < 16%), plane (16% < DoC < 37%), hollow (37% < DoC < 60%), pocket (DoC > 60%), and other (DoC = 0%) – always with reference to the counter-ion DoC; the "other" qualification refers to the portion of the electrode that either has zero ions or only co-ions

157

in its vicinity. Note that these definitions are based on natural partitions as depicted in Figure 9.2; their ranges are slightly larger than those of Ref. 188 as we include hydrogen-terminated edges in our electrode structures.

9.4 DISCHARGE CAPACITANCE USING NANOPOROUS CARBON

To evaluate the capacitance, each simulation is first pre-cycled (see Methods) with at least 3 charge and 2 discharge ramps. These simulations are then held at $\Delta\Phi$ for 250 ps before linearly discharged to 0 V over 1 ns. The difference in the total electrode charge (q_{elec}) between 0 V and $\Delta\Phi$ is used to calculate the discharge capacitance ($C_D = 2q_{elec}/\Delta\Phi$); we should note that the factor of two is adopted from experimental procedures for symmetric two-electrode cells to approximate the half-cell potential.

Figure 9.3 shows the computed C_D at different $\Delta\Phi$ for the three NPC electrodes. First, we evaluate the areal C_D ($C_{ar} = C_D/S$) seen in Figure 9.3(a) based on our approximation of the surface area (of a single electrode) and find a clear dependence on the nominal pore size of the electrode. Specifically, with $\Delta\Phi = 3$ V, the C_{ar} is predicted to increase from 13 to 18 $\mu\text{F/cm}^2$ as the nominal pore size decreases from 12 to 9 Å; this trend is consistent with the experimental work of Chmiola and coworkers[36] and Largeot and coworkers[37] which demonstrate that the capacitance can be maximized as the pore size approaches the size of the electrolyte ions. However, this trend is not predicted to translate to the specific C_D ($C_{sp} = C_D/m$) seen in Figure 9.3(b) (based on the mass of a single electrode), in which the NPC-9A and NPC-12A electrodes are estimated to perform best

(around 138 F/g at $\Delta\Phi = 3$ V). While this discrepancy between C_{ar} and C_{sp} has always been present throughout the literature, a unifying relationship between the two values and the electrode structure remains unclear.
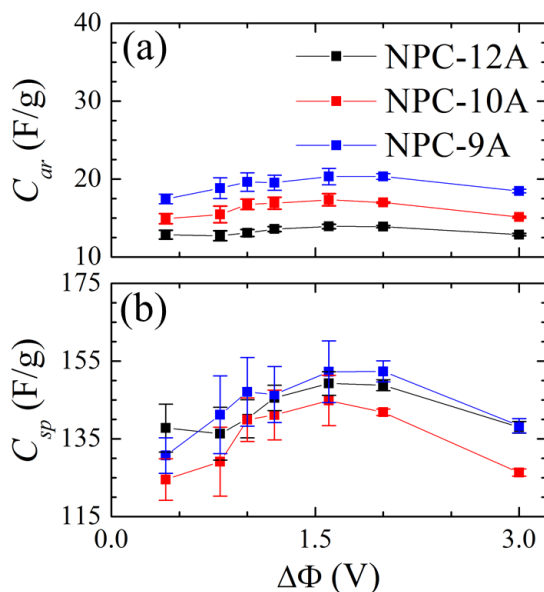
Figure 9.3   Comparison of the (a) areal (C_{ar}) and (b) specific (C_{sp}) discharge capacitances as a function of the applied full-cell potential ($\Delta\Phi$) using each nanoporous carbon electrode in a two-electrode configuration immersed in EMIM/BF$_4$ ionic liquid. The capacitances were calculated using the specific surface area (based on a N$_2$ gas probe) or mass of a single electrode. Note that the differences between the computed C_{ar} can vary significantly depending on the choice of gas molecule for structural characterization. Here, we do not consider the electrode capacitance contribution as it is assumed to be much larger than the double-layer contribution.

9.5 INFLUENCE OF CONFINEMENT ON CAPACITANCE

Previous theoretical work attempting to understand the influence of the pore size on capacitance consistently showed that the induced electrode charge storage directly scales with the confinement of ions within electrode regions.[188] Physically, this is intuitive

159

as each carbon atom is polarized and should participate in the screening of the ion charge. Indeed, our calculations exhibit similar behavior. For example, we find that in the NPC-9A case when $\Delta\Phi$ = 3 V, the electrode atoms in pocket sites store an average of 0.036 e/atom, which is greater than the average charge per electrode atom in hollow sites (0.028 e/atom) and plane sites (0.023 e/atom).
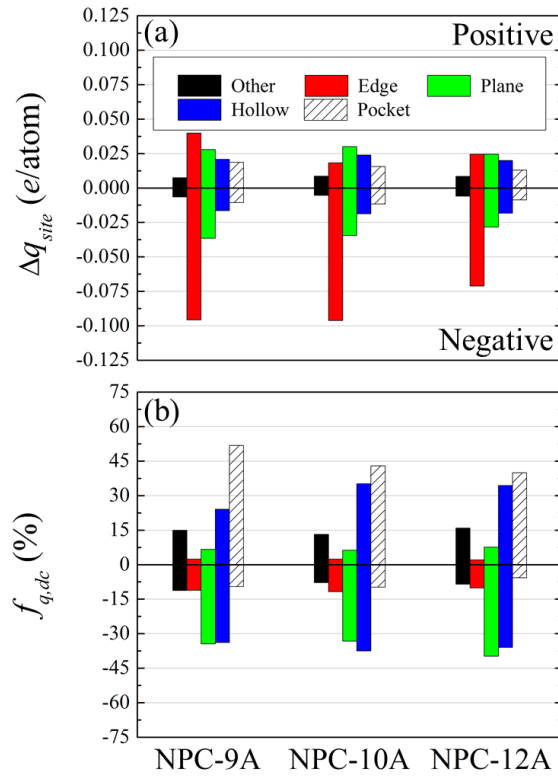
Figure 9.4   (a) Comparison of the discharge capacity per site (Δq_{site}) for the three electrode cases when the applied full-cell potential is 3 V. (b) Fraction of the capacitance attributed to the total discharge capacity per site ($f_{q,dc}$) for the three electrode cases when the applied full-cell potential is 3 V.

Upon discharging the system, however, two important observations are made. The first is that when $\Delta\Phi$ = 0 V, q_{elec} is not zero which shows that charge remains trapped within the electrode. The second is that the charge trapped within pocket sites greater exceeds that

160

of q_{elec}, which is compensated by depleted charge regions throughout the rest of the electrode. This significant charge puddling is analogous to that of graphene near charged impurities at the charge neutrality point.[205] As such, a more accurate metric for the capacitance is the discharge capacity per site (Δq_{site}) which indicates the change in q_{elec} (per atom, per site) upon discharge.

Figure 9.4(a) shows the computed Δq_{site} at each aforementioned electrode site (*i.e.*, other, edge, plane, hollow, pocket) for the three NPC electrodes considered. Surprisingly, the pocket sites display the smallest Δq_{site} compared to other sites due to the large amount of charge that remains trapped. In contrast, the edge sites tend to have the largest Δq_{site}, particularly in the negative electrode, which is chemically intuitive given that the presence of H-terminated edge defects promotes a greater accumulation of electrons compared to the basal plane[140]. This suggests that the confined nature of the pocket sites does not inherently enable large charge storage if the charge cannot be efficiently extracted.

Next, we investigate the contribution of the total discharge capacity of each site to the capacitance ($f_{q,dc}$) as shown in Figure 9.4(b); note that this fraction is calculated on an atomic basis rather than surface area basis. At both the positive and negative electrodes, the contribution from the pocket sites tends to increase as the pore size decreases. In addition, the contribution from the pocket sites tends to be much larger at the positive terminal, which is related to the size of the counter-ion. As discussed earlier, the compact BF_4^- counter-ion readily fills the pocket sites under positive polarization while the bulky $EMIM^+$ counter-ion prefers to fill the hollow and plane sites under negative polarization. Given that the C_{ar} is predicted to increase with smaller pore size, it appears that the

increased contribution of the pocket sites may be related. If we consider the fact that the effective surface area of an atom is reduced when part of a negative curvature surface compared to a planar surface, the observed trend in C_{ar} can be explained. However, an explanation for the observed trend in C_{sp} remains unclear. One possible reason is related to ion kinetics; during discharge, the extent to which counter-ions can escape from highly-confined regions may directly influence the capacitance. To assess this possibility, we evaluate the transient behavior of ions and electrode charge during the 1 ns discharge phase.

9.6 ION KINETICS DURING DISCHARGE

Figure 9.5(a)-(c) shows the fraction of the positive electrode utilized with counter-ions by each site (f_{util}) as a function of time (t) during discharge. First, we consider the utilization of sites when $t = 0$ ns. Here, it is evident that in all three cases, BF_4^- anions in pocket sites consistently tend to utilize around 50% of the electrode. In addition, the initial f_{util} of the hollow (other) sites diminishes (increases) as the nominal pore size decreases. The most interesting observation, however, is the extent to which f_{util} of the pocket sites decreases in the NPC-12A and NPC-9A cases compared to the NPC-10A case. Recall that the pocket sites tend to have the smallest Δq_{site}, which is on a per-atom (or effectively, per-mass) basis. Hence, the greater efficiency of counter-ion removal during discharge in the NPC-12A and NPC-9A cases compared to the NPC-10A case may be associated with the previously predicted discrepancies in C_{sp}.

162
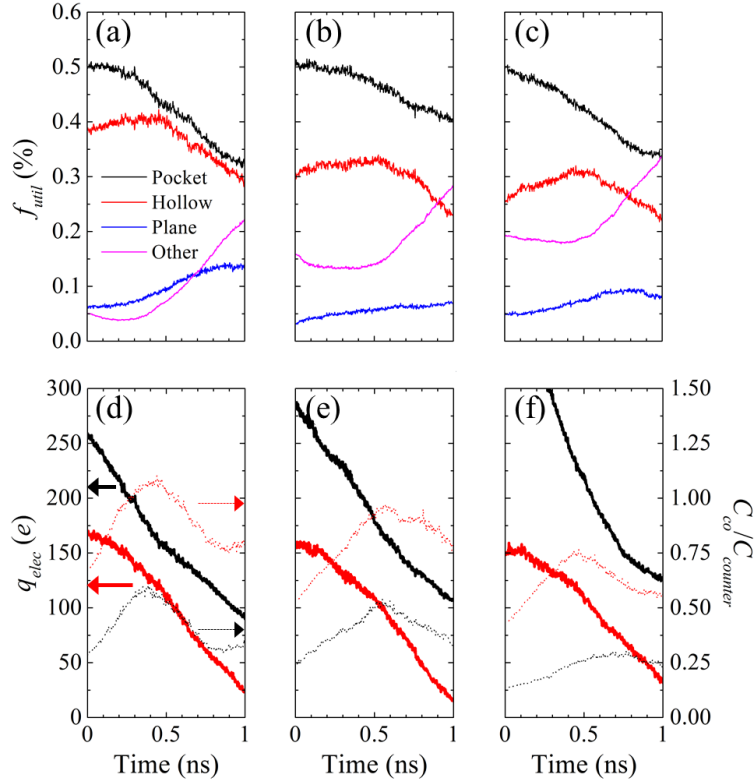
Figure 9.5   Discharge profiles of positive electrode when the applied full-cell potential varies from 3 to 0 V over 1 ns in a non-equilibrium MD simulation. The fraction of the electrode utilized (f_{util}) as each type of listed site in the (a) NPC-12A, (b) NPC-10A, and (c) NPC-9A case is shown. In addition, the (left axis) total charge stored (q_{elec}) and the (right axis) ratio of anion-cation coordination number (C_{co}) to the anion-anion coordination number ($C_{counter}$) in the pocket (black) and hollow (red) sites of the (d) NPC-12A, (b) NPC-10A, and (c) NPC-9A case is shown.

A potential mechanism for ion extraction can be conceived based on the f_{util} behavior of the other sites. In all three cases, the f_{util} of the hollow sites tends to increase while $t < 0.5$ ns, before diminishing. But the increase in the NPC-12A and NPC-9A cases is far more notable. This suggests that the hollow sites facilitate ion extraction from the pocket sites by accommodating extra counter-ions. Interestingly, the q_{elec} of the hollow sites (Figure 9.5(d)-(f)) continues to decrease despite the increase in counter-ion

163

accommodation, suggesting that the electrode-ion electrostatic interaction is not the primary driving force. However, we do find that the ratio of $EMIM^+$ co-ions to BF_4^- counter-ions that populate the coordination shell around hollow-adsorbed anions ($C_{co}/C_{counter}$) increases while $t < 0.5$ ns. A reorganization of the ions at the interface occurs such that the coordinated $EMIM^+$ cations stabilize anion accumulation due to the favorable ion-ion interactions. Eventually when $t > 0.5$ ns, the depletion of the hollow-site q_{elec} appears to be sufficient enough to allow anions (and coordinated cations) to lift-off from the surface into bulk-like reservoirs contained within the electrode volume, such that both f_{util} and $C_{co}/C_{counter}$ diminish.

9.7 RELATIONSHIP BETWEEN CAPACITANCE AND PORE SHAPE AND ITS DISPERSITY

In order for this reorganization of ions to occur, a dispersity of both pore shape and pore size should be present throughout the electrode. We propose that one way to approximate the pore shape, if we assume that the majority of the electrode consists of negative-curvature surfaces, is through knowledge of the specific surface area (S), pore volume (V_p), and the nominal pore size (W_p). Then, we define a pore shape factor (F_{ps})

$$F_{ps} = \frac{W_p}{\left(\frac{2V_p}{S}\right)}$$

such that the pores are nominally slit-like when $F_{ps} = 2$, cylindrical-like when $F_{ps} = 4$, and spherical-like when $F_{ps} = 6$. The dispersity of F_{ps} ($\approx \partial F_{ps}/\partial R_{gp}$) can then be qualitatively

164

assessed by the change in F_{ps} with respect to the radius of the probe molecule (R_{gp}) used to measure S and V_p. Figure 9.6(a) shows the calculated F_{ps} with varying R_{gp}. The larger slope seen in the NPC-12A and NPC-9A cases compared to the NPC-10A case indirectly confirms that the former two electrodes have greater pore shape dispersity, and therefore larger C_{sp}.
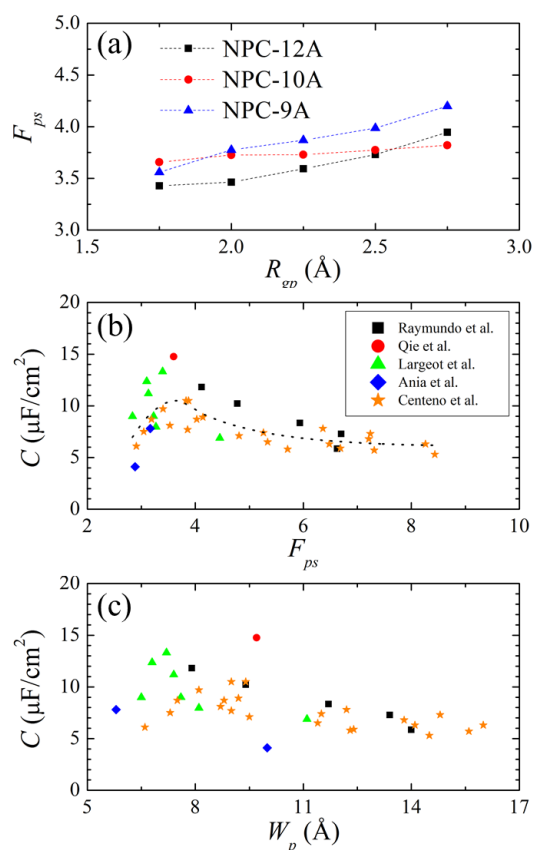
Figure 9.6   (a) Estimated pore shape factor (F_{ps}) based on the structural properties of the electrodes evaluated using different gas probe radii (R_{gp}). Comparison of experimental areal capacitance (C) based on BET surface areas with respect to (b) F_{ps} and (c) pore width (W_p). The dashed line in (b) serves as a visual guide. Experimental values were extracted from Ref. 37, 200, 206, 207, and 208.

The F_{ps} can also be helpful to understand trends in the C_{ar}. The coordination of ions by the electrode should be large when the pores are cylindrical-like. In addition, the effective surface area per atom is reduced compared to surfaces with less curvature. Hence, if we consider the F_{ps} when $R_{gp} = 2.25$ Å (*e.g.*, N$_2$), we find that our predicted C_{ar} increases as F_{ps} approaches 4 (*i.e.*, cylindrical-like). We can also extend this analysis to previously reported experimental capacitances (*C*) of nanoporous carbon. In Figure 9.6(b), we compare *C* as a function of F_{ps} from five different sources; here, the BET surface area is used and the W_p is estimated from provided pore size distributions when not directly reported. Remarkably, a distinct correlation is observed although the maximum appears to be centered around $F_{ps} \approx 3.7$. In comparison, *C* as a function of W_p is presented in Figure 9.6(c). The correlation with W_p is much weaker, which is consistent with the work of Centeno and coworkers[200] that showed a nearly independent relationship between *C* and W_p. This suggests that the capacitance may be more strongly described by the pore dispersity, characterized as F_{ps} in this work, than by W_p. However, in materials with very narrow pore size distributions (*e.g.*, CDCs), the choice of W_p may exhibit more influence.

9.8 CONCLUSIONS

We investigated the relationship between the structural properties of nanoporous carbons (immersed in EMIM/BF$_4$ ionic liquid) and the discharge capacitance using non-equilibrium molecular dynamics. The three electrodes studied in this work had nominal pore widths of 12.4, 10.8, and 9.6 Å with large capacitances of 138 F/g (13 µF/cm^2), 126

F/g (15 μF/cm^2), and 138 F/g (18 μF/cm^2), respectively, at 3 V. In an attempt to unify the discrepancies between the areal and specific capacitances, we analyzed the molecular origin of these capacitance values by studying both the electrode charge and ion redistribution during discharge. Our results show that significant charge can remain trapped within sites in which counter-ions are highly-confined by the electrode surface. Counter-ion extraction was found to be facilitated by the presence of pores that are connected to gradually less-confined electrode regions, which in turn allowed a gradual reorganization of ions to stabilize counter-ion accumulation and eventual desorption. Therefore, larger specific capacitances were attributed to more efficient ion extraction while larger areal capacitances were attributed to the greater utilization of confined regions. Based on this mechanism, a new structural property was proposed, termed the pore shape factor, which was demonstrated to show a strong correlation to experimental data and can serve as an alternative physical descriptor to the commonly used pore width.

These findings suggest that the design of future materials for supercapacitors requires an understanding of the relationship between pore dispersity and the molecular migration of ions (and surface charge) under quasi-equilibrium conditions. We anticipate that such insights may also help explain scattered impedance measurements and improve commonly used phenomenological transmission line models.[209-211] In addition, the approach presented in this work can be extended to study other factors such as different electrode surface chemistries and solvation effects. Finally, these results highlight the importance of reporting in-depth experimental characterization of the electrode structure,

including pore size distributions, specific surface areas, and pore volumes, using different

gas adsorbates.

Chapter 10: Summary and Future Directions

In this dissertation, we presented a fundamental investigation into the relationship between capacitive charge storage and the chemistry/structure of low-dimensional carbon-based nanomaterials (immersed in ionic liquid electrolyte) for use as electrodes in supercapacitors. For this study, we established a unique computational framework that combined ab-initio density functional theory and classical molecular dynamics to study the capacitance of the electrode-electrolyte interface. This approach allowed the interfacial capacitance (C_T) to be evaluated based on the in-series contributions from the quantum (C_Q) and double layer (C_D) capacitances such that $C_T = [(1/C_Q)^{-1} + (1/C_D)^{-1}]^{-1}$. As depicted in Figure 10.1, we explored a large materials design space that broadly encompassed graphene-based materials (Part I) and nanoporous carbons (Part II).

Throughout Part I, we were motivated to understand the potential of graphene-based electrodes as pristine graphene was previously demonstrated to exhibit low C_T due to its limited C_Q. Four types of possible modifications to graphene were considered: (1) local structural defects (*e.g.*, topological defects), (2) extended structural defects (*e.g.*, line edge defects), (3) chemical dopants (*e.g.*, metal dopants), and (4) chemical functionalization (*e.g.*, oxidation of the basal plane). In general, these graphene-derived materials were found to exhibit capacitances that far exceed that of pristine graphene electrodes, which was primarily attributed to the enhanced C_Q while the C_D was only marginally influenced. These findings demonstrate that engineering the disorder

169

throughout graphene-derived materials can be a viable strategy for future supercapacitor electrodes.
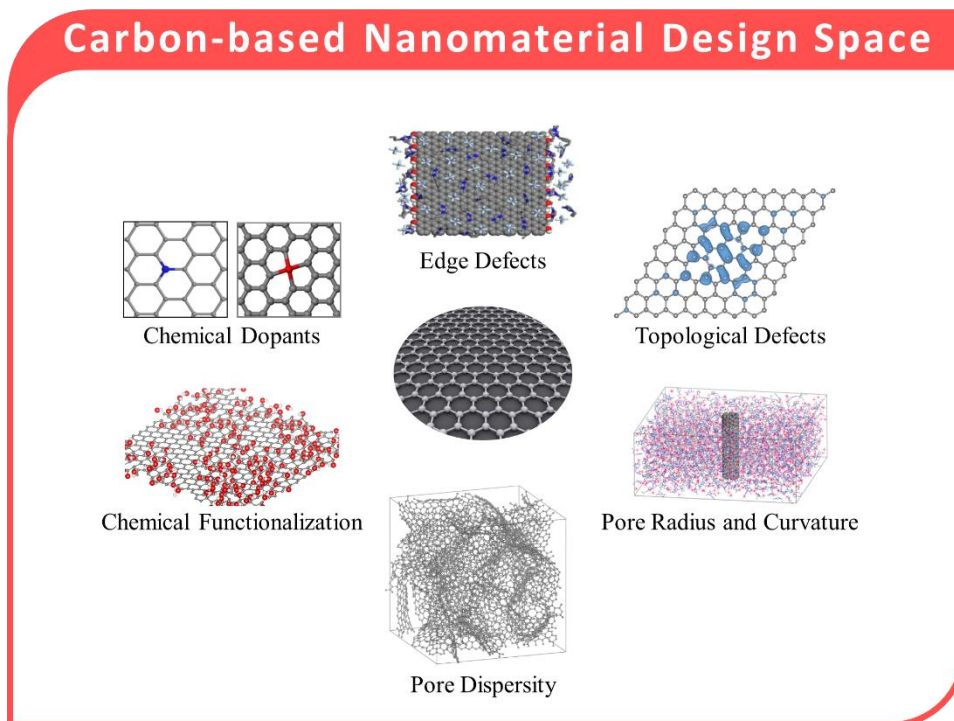
Figure 10.1 Schematic summary of the carbon-nanomaterial design space explored in this work.

Throughout Part II, we were motivated to understand the potential of nanoporous carbon electrodes with particular attention to the relationship between the pore characteristics and the capacitance. Given the strategies presented in Part I, we focused primarily on factors that influence C_D. Three structural factors related to nanoporous carbons were systematically considered: (1) curvature (*e.g.*, outer surface of CNTs), (2) pore diameter (*e.g.*, confinement within CNTs), and (3) pore dispersity (*e.g.*, carbide-derived carbons and activated carbons). In general, manipulating the electrode topology, in particular to promote electrolyte ion confinement, proved to be a viable means of

improving C_D, and therefore C_T, even with diminishing electrode surface area. However, the full utilization of these materials was found to be dependent on the dynamics of ion transport under an external field (*i.e.*, electro-kinetics).

A more detailed summary of the key findings of this dissertation, as well as thoughts of future directions, are described below.

10.1 MATERIALS DESIGN PRINCIPLES TO ENHANCE CAPACITANCE

A. Notable Trends on the Electronic Structure and Quantum Capacitance

The limited C_Q of pristine graphene electrode is a direct consequence of the zero density of states (DOS) at the charge neutrality point (*e.g.*, the Fermi level) that linearly increases away from the Fermi level. The origin of this unique DOS can be traced to the extended conjugation of the π system owing to the 2D honeycomb geometry of graphene. Therefore, one method to increase the availability of states near the charge neutrality point is to disrupt the π system of graphene by the introduction of both chemical and structural disorder. Here, we summarize the impact of different electrode designs on the electronic structure and the C_Q.

Trend 1: Capacitance enhancement is correlated to modification density

Interestingly, the impact of all the modifications explored throughout this dissertation on the electronic structure share a common trait: the predicted enhancement in C_Q is primarily attributed to the resultant quasi-localization of carbon p_z states in the

171

vicinity of the modification site. In the case of topological defects (Chapter 3), this is intuitive as the only important change to the electronic structure is based on a localized distortion to the lattice structure. Yet even when chemical functional groups were considered (Chapter 6), the most relevant changes to the electronic structure were attributed to the p_z states of carbon atoms adjacent to functionalized sites, which could remain partially coupled to the disrupted π system. A notable exception is the case of transition metal dopants (Chapter 4); the hybridization between the metal $3d$ states and carbon $2p$ states can also introduce non-bonding d states close to the Fermi level which considerably increases the number of available states. Nonetheless, this suggests that the C_Q enhancement can be estimated from the concentration of modified sites along the graphene lattice.

Figure 7.1 depicts the average (with respect to positive and negative polarization) C_Q (at ±0.5 V) of graphene-derived materials as a function of concentration of directly modified atoms; in other words, the concentration does not include the degree of lattice reconstruction that may result from each type of modification. Remarkably, the increase in C_Q is confirmed to be generally correlated to the modification concentration while independent of the type of modification; here, transition metal dopants are excluded due to its inclusion of $3d$ states. In addition, it is clear that even at very low concentrations (< 1 at.%), the C_Q of graphene exhibits dramatic improvements. Another important feature is the ability of graphene to remain metallic even at large modification concentrations approaching 30 at.%, as contiguous regions of conjugated π states can still exist. However, graphene may become semi-conducting at these concentrations if the modifications to the

lattice are homogeneously dispersed (Chapter 6) or even if the modification concentration continues to increase. Therefore, there is a limit to the potential benefit of disorder engineering to C_Q, although this ceiling is quite high.
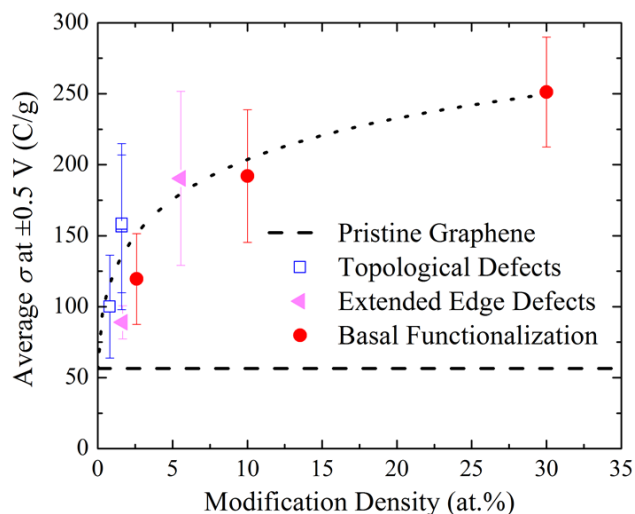
Figure 10.2   Comparison of the average excess electrode charge (σ evaluated at an electrode potential of ±0.5 V) of graphene-based materials modified with different atomic concentrations (at.%). The dashed line indicates the σ of pristine graphene, which serves as a reference point. The dotted line is a visual aid demonstrating the trend.

Trend 2: Materials optimization should include inherent asymmetric enhancement in capacitance

The introduction of chemical and structural disorder in these materials also tends to induce an asymmetric enhancement in C_Q with respect to positive and negative polarization. In a standard two-electrode configuration, then, the energy density will be limited by the lower of the two asymmetric C_Q. Therefore, optimal materials design also involves understanding which types of modifications are better suited for electron or hole

injection. According to the analysis presented throughout Part I, it appears that the suitability of each modification primarily depends on the charge withdrawing/donating nature of the modified site. However, in many cases this behavior depends more on the nature of hybridization rather than the relative electronegativity of bonded species (*e.g.*, oxygen is usually more electronegative than carbon). For example, the π states near most topological defects (Chapter 2) tend to be electron withdrawing (similar to *p*-type dopants) and consequently favor positive polarization. In graphene oxide, the oxidation sites along the basal plane (Chapter 6) similarly serve as *p*-type sites and favor positive polarization. On the other hand, oxidized edge defects serve as an *n*-type site (Chapter 5) as the lone pair oxygen states slightly hybridize with adjacent carbon p_z states (*i.e.*, electron donating) and consequently favor negative polarization. Therefore, modifications that tend to deplete (inject) electrons from (to) the extended π system are generally better suited as positive (negative) electrodes materials.

B. Notable Trends on the Double Layer Microstructure and Capacitance

The C_D of the electric double layer (EDL) at the electrode-electrolyte interface is directly related to the molecular behavior of accumulated ions. For example, at the interface of pristine graphene electrodes, the IL microstructure is known to exhibit distinct cation/anion segregation perpendicular to the electrode surface that tends to extend up to 2-3 nm. The origins of this layering can be traced to the over-screening of the electrode surface charge by the compact layer of adjacent counter-ions; the strong counterion-coion

electrostatic attraction triggers the formation of subsequent ion layers. Nonetheless, the potential drop across the EDL, and thereby C_D, is found to be primarily determined by the packing density of the immediately adjacent layer of counter-ions. Here, we summarize the impact of different electrode designs on the C_D.

Trend 3: Most graphene modifications weakly perturb the double layer and capacitance

At low concentrations (less than 5 at.%) of chemical or structural modification to graphene, such as those presented in Chapters 3 and 4, the microstructure of the electric double layer was observed to be nearly the same as that of pristine graphene in both neutral and charged states. Under neutral conditions, this was attributed to the fact that any charge redistribution along the graphene sheet was localized to the modified sites. Given the small Debye length of ionic liquids, only the ions closest to the modified sites were required to reorganize to screen the perturbed field. Relatedly, excess charge carriers were predicted to spread broadly across the graphene lattice as most of the π system remained intact. Therefore, the resultant ion accumulation at the EDL also remained the same while the C_D was virtually unaffected.

Trend 4: When double layers are noticeably perturbed, the spatial accumulation of excess charge determines the capacitance

At larger modification concentrations, such as the cases presented in Chapters 5 and 6, the charge redistribution along the graphene lattice was observed to induce a notable restructuring of the EDL. For example, in the presence of both edge defects or hydroxyl

functional groups, the electrolyte ions that reorganized to screen the localized surface charge tended to trigger alternating cation/anion ordering (*i.e.*, segregation) parallel to the electrode surface under neutral conditions. Interestingly, the C_D, in comparison to that of pristine graphene electrodes, is observed to increase near edge defects (Chapter 5) and decrease near basal-functionalized hydroxyl groups (Chapter 6). This difference was attributed to the tendency of injected charge carriers to localize at sites that allow counter-ions to accumulate with ease (difficulty) in the edge defect (hydroxyl functionalization) case. Therefore, at these large modification concentrations, the C_D also strongly depends upon the electronic structure of the electrode material.

Trend 5: Promoting ion segregation via the electrode topology can improve capacitance

As described in Part I, the C_D of the electric double layer (EDL) is dependent on the molecular packing of ions at the electrode-electrolyte interface. One important aspect that was previously identified is the degree of cation-anion segregation; the C_D was found to be inversely related to greater counter-ion/co-ion mixing within the EDL.

Throughout Part II, the influence of electrode topology on C_D was found to exhibit a similar dependence. For example, electrode surfaces with increasing positive curvature (Chapter 7) tended to encourage increasingly enhanced C_D. While this was primarily attributed to the natural decay of an electric field in cylindrical geometries, the promotion of ion mixing due to weaker electrode-electrolyte electrostatic interactions mitigated this benefit, especially at large applied potentials. On the other hand, increasingly narrow cylindrical nanopores (Chapter 8) were predicted to have dramatically enhanced C_D (with

respect to planar electrodes), especially when the pore diameter is small enough to only accommodate single-molecule chains of ions. Upon charging, ideal segregation can occur such that only counter-ions remain in the pore while co-ions are expelled, thereby allowing more charge to be stored at the electrode walls with greater C_D. Even in the case of materials with broad pore size distributions, such as nanoporous carbons (Chapter 9), the amount of local excess charge stabilized by counter-ions directly scaled with the degree of ion confinement by the electrode surface as these highly-confined environments also promoted electrolyte segregation. Therefore, the C_D was found to increase as the electrode surface topology, as characterized by the introduced pore shape factor, became more cylindrical-like.

Nonetheless, the full C_D can only be utilized if both the charged state (with ideally segregated ions) and neutral state (with ideally mixed ions to maintain charge neutrality) are efficiently accessed during the rapid charge/discharge cycles of supercapacitor operation. The kinetics that dictate this transition are described in the next section.

10.2 INSIGHTS INTO ION ELECTROKINETICS UNDER CONFINEMENT

In an ideal supercapacitor, the microstructure of the EDL during the charged and uncharged states should reversibly transition between ideal counter-ion/co-ion segregation and mixing, respectively, in order to maximize the C_D. This is especially true when the primary strategy to improve C_D is through ion confinement. However, as observed in Chapters 8 and 9, the failure of counter-ions to migrate out of pores during discharge (or

similarly, co-ions during charging) effectively prevents local capacitive storage in those regions. During the charge phase, these stagnated ions can avert local accumulation of excess electrode charge (Chapter 8). Similarly, during discharge, these trapped ions can inhibit the utilization of excess electrode charge (Chapter 9). Two primary factors (described below) were identified to influence the ion transport under an external field, or so-called electrokinetics, in these confined regions.

First, the so-called scan rate (as used in cyclic voltammetry measurements), which depends on the applied potential and the rate of charge/discharge, was found to have an interesting non-linear relationship with C_D. For example, during the charging of subnanometer cylindrical pores (Chapter 9), an abrupt capacitive loss was observed beyond a critical scan rate. This was attributed to the development of a so-called depletion region in which co-ions remained trapped within the pores; beyond the critical scan rate, the depletion region was predicted to always develop. According to our analysis, the critical scan rate is dependent on the competition between forced electro-kinetic flow and natural ion convection.

The second factor is the geometry of the electrode, with particular attention to materials with broad pore size distributions. In Chapter 9, we found that the ion stagnation (as previously described) could be mitigated, to a certain extent, if the electrode structure contained pores with broadly varying pore shapes (as characterized by the aforementioned pore shape factor). In particular, an electrode topology with a connected network of pores with gradually diminishing confinement was identified to facilitate ion extraction and

eventual desorption from the electrode surface. Our analysis showed that such structural features were necessary to aid counter-ion/co-ion reorganization during discharge.

Here, we have identified factors that may be essential to understand the dynamics related to capacitance. More importantly, it is evident that our fundamental knowledge of the dynamics at electrode-electrolyte interfaces remains limited, thereby warranting further investigation. For instance, the influence of the scan rate and electrode structure should be inherently related, although their relative contributions remain unclear. This work therefore provides both motivation and a framework to explore the transitions between charged and uncharged states that may accessed during supercapacitor operations.

10.3 PERSPECTIVE ON NEW RESEARCH DIRECTIONS

As stated in Chapter 1, the development of electrode materials for supercapacitors has historically been driven by the paradigm that the capacitance is limited by the efficiency of ion packing and accumulation in the electric double layer. Naturally, the exploration of carbon materials, such as activated carbons, was guided by a specific research question: *how can we increase the specific and volumetric surface areas of conductive materials?*

Recently, the benefits from this approach have yielded diminishing returns as cost-effective methods to create high surface area materials have matured. As a result, most commercial supercapacitors can be considered a commodity product, in which price is the main distinguishing feature while performance tends to be comparable across the market. The emergence of carbon nanomaterials, however, has provided a new pathway to develop

next-generation supercapacitors with the potential to out-class current devices. Yet interestingly, the use of these materials as electrodes has demonstrated enhanced capacitive performance that does not necessarily scale with surface area. However, early experimental reports noticed a possible correlation between the capacitance and the average pore width, which was attributed to selective ion segregation based on pore size.[36,37] These observations prompted a shift to a new research question: *how does the structure of the electrode influence ion packing and the capacitance?*

Motivated by this question, recent experimental[200,212-214] and theoretical[21,85,86,179,188,215,216] works have attempted to elucidate the relationship between the capacitance and pore size, pore distribution, pore volume, and other facets of the electrode topology. Throughout this work, however, we have demonstrated that other nuances can significantly affect the capacitance. Some of these factors include the ease of charge injection into the electrode (*i.e.*, the quantum capacitance), the preferred spatial accumulation of excess charge carriers throughout the electrode, as well as the kinetics of ion reorganization in response to an external field. These findings suggest that the open question that guides research should be amended to: *how does the electrode chemistry and structure affect excess charge accumulation and how efficiently do ions respond to screen the field?*

Based on this amended research question, suggestions to improve two common practices in theoretical simulations are proposed. The first common practice is the evaluation of the electric double layer microstructure and capacitance at thermodynamic equilibrium. Instead, it may be more appropriate to probe the capacitance using non-equilibrium simulations (*e.g.*, emulated cyclic voltammetry) in order to capture other

accessible pseudo-equilibrium states. To achieve this, improvements should be made to the constant potential method commonly used to approximate the electrode excess charge distribution. While previously used methods were limited to surface atoms with equal polarizability, the method presented in Chapters 8 and 9 has the ability to distinguish chemically-diverse species. Nonetheless, this model can be improved to incorporate more complex phenomena, such as nonlinear electrostatic screening observed in few-layer graphene[217], which may be necessary for low-dimensional carbon nanomaterials.

10.4 POTENTIAL FUTURE DIRECTIONS

A. Tailoring Performance with Ionic Liquid Optimization

One attractive aspect of ionic liquids is their large design space, spanning the many types of cations (*e.g.*, imidazolium, phosphonium, pyridinium, etc.) and anions (*e.g.*, borates, phosphates, sulfonimides) that can be synthesized and paired together. For supercapacitors, choosing the proper cation-anion pair with a given electrode material can further improve the capacitance. To help sieve through this large parameter space to optimize performance, the size of the ion is commonly chosen as a defining characteristic. For example, the compact Cl^- anion has been predicted to yield larger capacitances than PF_6^-, a bulkier anion, at graphene and carbon nanotube interfaces due to the effective ion packing in the former case.[85] In nanoporous materials, the capacitance is also expected to be optimal when the ion size is slightly smaller than the average pore width to allow only single-ion accomodation.[37] Indeed, the work presented here exhibits similar trends. In

Chapter 8, the axial charge distribution as well as the size of the depletion region differed at the negative and positive electrodes due to the differences in the cation and anion size. Similarly, the electrode surface utilization in Chapter 9 depended on the size of the counter-ion.

While the ion size has been a successful physical descriptor, it may be important to investigate further the influence of different ion shapes and charge distributions on the double layer formation and capacitance. For example, imidazolium cations with long tails paired with compact anions can form heterogeneous domains due to (1) the strong electrostatic attraction between the charged head groups of the cations and the anions and (2) the van der Waals interactions between the weakly charged tail groups.[218] As observed in Chapter 6, such heterogeneity can impede ion reorganization upon electrode charging. In addition, the shape and charge distribution of the ions can also influence their electrokinetic behavior, as observed with ionic liquid lubricants under an external field[219], which is especially important when in highly-confined regions. Therefore, these additional considerations concerning the ion size, shape/flexibility, and charge distribution may be probed to tailor the design of future ionic liquids.

B. Developing Carbon-Based Materials for Pseudo-Capacitors

The characteristic differences between supercapacitors (high power density) and batteries (high energy density) can be attributed to the differences in their charge storage mechanisms. For example, batteries involve redox reactions at the interface which

inherently deliver more charge than simply storing them electrostatically in the double layer of supercapacitors. On the other hand, ion reorganization and diffusion in the double layer is typically much faster than charge transfer kinetics in batteries. Devices that utilize both charge transfer and double layer formation for energy storage are called pseudo-capacitors, which have moderate power densities and energy densities. Typically, the active electrode material consists of a metal oxide, such as MnO_2 or V_2O_5, supported on a conductive carbon matrix.[220,221] Reduced graphene oxide has also demonstrated pseudo-capacitive characteristics, which has the added benefit of larger electrical conductivity compared to metal oxides.[222,223] However, in all of these cases, an aqueous electrolyte is required as the reaction, which should be reversible, involves either protons, hydronium ions, or intercalation of alkali ions.[221]

Currently, it remains to be seen if modified carbon nanomaterials immersed in ionic liquid can be used in a pseudo-capacitive manner. Based on conventional mechanisms, it seems unlikely given the large electrochemical windows of ionic liquids. However, in this work, effects analogous to pseudo-capacitance have been demonstrated through chemical/mechanical modification of graphene. For example, the dramatically enhanced capacitance predicted for transition metal-doped graphene (Chapter 4) may be attributed to the filling of the metal $3d$ non-bonding states, effectively changing the metal valency. Pseudo-capacitive effects in graphene oxide can also be hypothesized based on the stability analysis presented in Chapter 6. In this case, it is conceivable that with different structures, oxygen concentrations, and operating potentials, electrochemical reduction based on interacting functional groups may occur. The challenge, however, is to ensure that the

reaction can be reversible. This will likely depend on both the electronic structure of the electrode material and the relative stability of the product species adsorbed on the surface compared to their solubility in the ionic liquid.

C. Understanding Charging Dynamics and Impedance

As porous carbon supercapacitor electrodes utilize increasingly narrow pores, it is important to understand the factors that facilitate or inhibit ion transport, and to a certain extent, charge carrier transport, thus enabling the design of materials that maintain large power densities. The charging dynamics are typically characterized by the impedance, which can be measured with electrochemical impedance spectroscopy. The observed impedance is then related to an equivalent circuit model with parameters that depend upon the pore structure. In the commonly used de Levie transmission line model, uniform cylindrical rods are assumed with key parameters including the pore radius, length, and number of pores.[224] In the past, this model has been useful for porous electrodes with large pores and wide pore distributions.[225] However, contemporary porous electrodes, especially those fabricated with subnanometer pores, tend to exhibit anomalous impedance such as a previously unobserved dependence on the applied potential.[226] Given the observations in Chapter 9, namely the differences in the charging profiles between electrode sites with different shapes, it is timely to explore the molecular charging behavior of ions confined within these nanostructures to aid in the development of macroscopic models and understanding of charge and ion transport in these materials. Beyond studying the role of

electrode topology, the ion reorganization mechanism described in Chapter 9 also suggests that the role of ion-solvent interactions should also be considered.

D. Extending to Other Applications

On a final note, it is worth mentioning that the concepts developed in this dissertation may be extended to other applications involving electrified solid-liquid interfaces. One notable example is water desalination through a capacitive deionization (CDI) mechanism.[227] Here, polarized carbon nanomaterials are often used to electrostatically attract and extract salts from a brine feed. Many of the operating principles are similar to supercapacitors, including the need for wide electrochemical windows, long electrode lifetimes, and large capacitances. However, a key metric that distinguishes water desalination from supercapacitors is the energy efficiency of ion extraction. Namely, materials should be optimized to maximize the amount of ions adsorbed on the surface with minimal energy (the product of excess charge and voltage). Conceivably, this might be achieved by promoting co-ion/counter-ion mixing to stabilize more counter-ions at the interface, similar to the discharge mechanism identified in Chapter 9. Therefore, a theoretical approach, such as the methodology and analysis presented in Chapters 8 and 9, may help elucidate design principles to maximize CDI efficiency.

Another example is the recent use of ionic liquids as gate dielectrics in field effect transistors (FET).[228] Here, the intention is to utilize the semiconductor-ionic liquid electric double layer to induce large charge carrier densities in the FET channel; in other words, a

large capacitance is favorable in order to maximize the charge carrier density with minimal energy consumption. In this case, the two key metrics are the carrier mobility and the threshold voltage. The carrier mobility has been observed to decrease with increasing capacitance[229], which is likely related to the ionic-liquid-induced polarization of the channel surface acting as shallow traps[230]. On the other hand, the threshold voltage can be tuned based on the alignment of the semiconductor and gate flat band potentials, which is also associated with the potential variation through the EDL.[231] This motivates an in-depth study into the performance of these devices based on the coupling between channel material and ionic liquid, which is well-suited for the theoretical approach presented in Part I.

The methodologies, analyses, and conclusions of this work may therefore be broadly applicable to future studies involving the interfacial accumulation of excess charge and ions under external potential.

References

(1)   Barton, J. P.; Infield, D. G. Energy Storage and Its Use with Intermittent Renewable Energy. *IEEE Trans. Energy Convers.* **2004**, *19* (2), 441–448.

(2)   Yang, Z.; Zhang, J.; Kintner-Meyer, M. C. W.; Lu, X.; Choi, D.; Lemmon, J. P.; Liu, J. Electrochemical Energy Storage for Green Grid. *Chem. Rev.* **2011**, *111*, 3577–3613.

(3)   Chen, H.; Cong, T. N.; Yang, W.; Tan, C.; Li, Y.; Ding, Y. Progress in Electrical Energy Storage System: A Critical Review. *Prog. Nat. Sci.* **2009**, *19* (3), 291–312.

(4)   Karden, E.; Ploumen, S.; Fricke, B.; Miller, T.; Snyder, K. Energy Storage Devices for Future Hybrid Electric Vehicles. *J. Power Sources* **2007**, *168* (1 SPEC. ISS.), 2–11.

(5)   Simon, P.; Gogotsi, Y. Materials for Electrochemical Capacitors. *Nat. Mater.* **2008**, *7* (11), 845–854.

(6)   Winter, M.; Brodd, R. J. What Are Batteries, Fuel Cells, and Supercapacitors? *Chem. Rev.* **2004**, *104* (10), 4245–4269.

(7)   Bakker, M. G.; Frazier, R. M.; Xu, C.; Pan, S.; Spear, S.; Chopra, N.; Bara, J. E.; Burkett, S. Perspectives on Supercapacitors, Pseudocapacitors and Batteries. *Nanomater. Energy* **2012**, *1* (3), 136–158.

(8)   Helmholtz, H. Ueber Einige Gesetze Der Vertheilung Elektrischer Ströme in Körperlichen Leitern Mit Anwendung Auf Die Thierisch-Elektrischen Versuche. *Ann. Phys.* **1853**, *165* (6), 211–233.

(9)   Stern, O. ZUR THEORIE DER ELEKTROLYTISCHEN DOPPELSCHICHT. *Zeitschrift für Elektrochemie und Angew. Phys. Chemie* **1924**, *30* (21-22), 508–516.

(10)   Rogers, R.; Seddon, K. Ionic Liquids--Solvents of the Future? *Science* **2003**, *302*, 792–793.

(11)   Xu, W.; Angell, C. Solvent-Free Electrolytes with Aqueous Solution-like Conductivities. *Science* **2003**, *302*, 422–425.

(12)   Lewandowski, A.; Galiński, M. Carbon–ionic Liquid Double-Layer Capacitors. *J. Phys. Chem. Solids* **2004**, *65* (2-3), 281–286.

(13)   Paek, E.; Pak, A. J.; Hwang, G. S. A Computational Study of the Interfacial Structure and Capacitance of Graphene in [BMIM][PF6] Ionic Liquid. *J.*

Electrochem. Soc. **2013**, *160* (1), A1–A10.

(14) Maolin, S.; Fuchun, Z.; Guozhong, W.; Haiping, F.; Chunlei, W.; Shimou, C.; Yi, Z.; Jun, H. Ordering Layers of [Bmim][PF$_6$] Ionic Liquid on Graphite Surfaces: Molecular Dynamics Simulation. *J. Chem. Phys.* **2008**, *128* (13), 134504.

(15) Kislenko, S. A.; Samoylov, I. S.; Amirov, R. H. Molecular Dynamics Simulation of the Electrochemical Interface Between a Graphite Surface and the Ionic Liquid [BMIM][PF$_6$]. *Phys. Chem. Chem. Phys.* **2009**, *11* (27), 5584–5590.

(16) Lockett, V.; Sedev, R.; Ralston, J.; Horne, M.; Rodopoulos, T. Differential Capacitance of the Electrical Double Layer in Imidazolium-Based Ionic Liquids: Influence of Potential, Cation Size, and Temperature. *J. Phys. Chem. C* **2008**, *112*, 7486–7495.

(17) Alam, M. T.; Masud, J.; Islam, M. M.; Okajima, T.; Ohsaka, T. Differential Capacitance at Au(111) in 1-Alkyl-3-Methylimidazolium Tetrafluoroborate Based Room-Temperature Ionic Liquids. *J. Phys. Chem. C* **2011**, *115* (40), 19797–19804.

(18) Alam, M. T.; Islam, M.; Okajima, T.; Ohsaka, T. Capacitance Measurements in a Series of Room-Temperature Ionic Liquids at Glassy Carbon and Gold Electrode Interfaces. *J. Phys. Chem. C* **2008**, *112*, 16600–16608.

(19) Kornyshev, A. Double-Layer in Ionic Liquids: Paradigm Change? *J. Phys. Chem. B* **2007**, *111* (20), 5545–5557.

(20) Feng, G.; Jiang, D.; Cummings, P. T. Curvature Effect on the Capacitance of Electric Double Layers at Ionic Liquid / Onion-Like Carbon Interfaces. *J. Chem. Theory Comput.* **2012**, *8* (3), 1058–1063.

(21) Vatamanu, J.; Cao, L.; Borodin, O. On the Influence of Surface Topography on the Electric Double Layer Structure and Differential Capacitance of Graphite/ionic Liquid Interfaces. *J. Phys. Chem. Lett.* **2011**, *2*, 2267–2272.

(22) Ma, K.; Woodward, C. E.; Forsman, J. Classical Density Functional Study on Interfacial Structure and Differential Capacitance of Ionic Liquids near Charged Surfaces Classical Density Functional Study on Interfacial Structure and Differential Capacitance of Ionic Liquids near Charged Surfaces. *J. Phys. Chem. C* **2014**, *118*, 15825–15834.

(23) Lauw, Y.; Horne, M.; Rodopoulos, T.; Leermakers, F. Room-Temperature Ionic Liquids: Excluded Volume and Ion Polarizability Effects in the Electrical Double-Layer Structure and Capacitance. *Phys. Rev. Lett.* **2009**, *103* (11), 1–4.

(24) Simon, P.; Gogotsi, Y. Capacitive Energy Storage in Nanostructured Carbon-

Electrolyte Systems. *Acc. Chem. Res.* **2012**, *46* (5), 1094–1103.

(25) Wang, G.; Zhang, L.; Zhang, J. A Review of Electrode Materials for Electrochemical Supercapacitors. *Chem. Soc. Rev.* **2012**, *41* (2), 797–828.

(26) Islam, M. M.; Alam, M. T.; Okajima, T.; Ohsaka, T. Electrical Double Layer Structure in Ionic Liquids: An Understanding of the Unusual Capacitance−Potential Curve at a Nonmetallic Electrode. *J. Phys. Chem. C* **2009**, *113* (9), 3386–3389.

(27) Islam, M.; Alam, M. T.; Ohsaka, T. Electrical Double-Layer Structure in Ionic Liquids : A Corroboration of the Theoretical Model by Experimental Results. *J. Phys. Chem. C* **2008**, *112*, 16568–16574.

(28) Lockett, V.; Horne, M.; Sedev, R.; Rodopoulos, T.; Ralston, J. Differential Capacitance of the Double Layer at the Electrode/ionic Liquids Interface. *Phys. Chem. Chem. Phys.* **2010**, *12* (39), 12499–12512.

(29) Randin, J.-P.; Yeager, E. Differential Capacitance Study of Stress-Annealed Pyrolytic Graphite Electrodes. *J. Electrochem. Soc.* **1971**, *118* (5), 711–714.

(30) Gerischer, H. An Interpretation of the Double Layer Capacity. *J. Phys. Chem.* **1985**, *89*, 4249–4251.

(31) Gerischer, H.; McIntyre, R.; Scherson, D.; Storck, W. Density of the Electronic States of Graphite: Derivation from Differential Capacitance Measurements. *J. Phys. Chem.* **1987**, *91* (1), 1930–1935.

(32) Luryi, S. Quantum Capacitance Devices. *Appl. Phys. Lett.* **1988**, *52* (6), 501–503.

(33) Paek, E.; Pak, A. J.; Kweon, K. E.; Hwang, G. S. On the Origin of the Enhanced Supercapacitor Performance of Nitrogen-Doped Graphene. *J. Phys. Chem. C* **2013**, *117* (11), 5610–5616.

(34) Xia, J.; Chen, F.; Li, J.; Tao, N. Measurement of the Quantum Capacitance of Graphene. *Nat. Nanotechnol.* **2009**, *4* (8), 505–509.

(35) Stoller, M. D.; Magnuson, C. W.; Zhu, Y.; Murali, S.; Suk, J. W.; Piner, R.; Ruoff, R. S. Interfacial Capacitance of Single Layer Graphene. *Energy Environ. Sci.* **2011**, *4* (11), 4685–4689.

(36) Chmiola, J.; Yushin, G.; Gogotsi, Y.; Portet, C.; Simon, P.; Taberna, P. L. Anomalous Increase in Carbon Capacitance at Pore Sizes Less than 1 Nanometer. *Science* **2006**, *313* (5794), 1760–1763.

(37) Largeot, C.; Portet, C.; Chmiola, J.; Taberna, P.; Gogotsi, Y.; Simon, P. Relation

between the Ion Size and Pore Size for an Electric Double-Layer Capacitor. *J. Am. Chem. Soc.* **2008**, *130*, 2730–2731.

(38) Schrödinger, E. An Undulatory Theory of the Mechanics of Atoms and Molecules. *Phys. Rev.* **1926**, *28* (6), 1049–1070.

(39) Born, M.; Oppenheimer, R. Zur Quantentheorie Der Molekeln. *Ann. Phys.* **1927**, *20* (84), 457–484.

(40) Hohenberg, P.; Kohn, W. Inhomogeneous Electron Gas. *Phys. Rev.* **1964**, *136* (3B), B864–B871.

(41) Kohn, W.; Sham, L. J. Self-Consistent Equations Including Exchange and Correlation Effects. *Phys. Rev.* **1965**, *140* (4A), A1133–A1138.

(42) Kresse, G.; Furthmüller, J. Efficient Iterative Schemes for Ab Initio Total-Energy Calculations Using a Plane-Wave Basis Set. *Phys. Rev. B. Condens. Matter* **1996**, *54* (16), 11169–11186.

(43) Perdew, J. P.; Burke, K.; Ernzerhof, M. Generalized Gradient Approximation Made Simple. *Phys. Rev. Lett.* **1996**, *77* (18), 3865–3868.

(44) Burke, K. Perspective on Density Functional Theory. *J. Chem. Phys.* **2012**, *136* (15), 150901.

(45) Becke, A. D. Perspective: Fifty Years of Density-Functional Theory in Chemical Physics. *J. Chem. Phys.* **2014**, *140* (18), 18A301.

(46) Snow, E. C.; Wood, J. H. The Frozen Core Approximation in Solid State and Molecular Calculations. *Chem. Phys. Lett.* **1974**, *25* (1), 111–113.

(47) Blöchl, P. Projector Augmented-Wave Method. *Phys. Rev. B* **1994**, *50* (24), 17953–17979.

(48) Alder, B. J.; Wainwright, T. E. Studies in Molecular Dynamics. I. General Method. *J. Chem. Phys.* **1959**, *31* (2), 459.

(49) Shaw, D. E.; Bowers, K. J.; Chow, E.; Eastwood, M. P.; Ierardi, D. J.; Klepeis, J. L.; Kuskin, J. S.; Larson, R. H.; Lindorff-Larsen, K.; Maragakis, P.; et al. Millisecond-Scale Molecular Dynamics Simulations on Anton. In *Proceedings of the Conference on High Performance Computing Networking, Storage and Analysis - SC '09*; ACM Press: New York, New York, USA, 2009; p 1.

(50) Jorgensen, W. L. Optimized Intermolecular Potential Functions for Liquid Alcohols. *J. Phys. Chem.* **1986**, *90* (7), 1276–1284.

(51) Wang, J.; Wolf, R. M.; Caldwell, J. W.; Kollman, P. A.; Case, D. A. Development and Testing of a General Amber Force Field. *J. Comput. Chem.* **2004**, *25*, 1157−74.

(52) Jones, J. E. On the Determination of Molecular Fields. II. From the Equation of State of a Gas. *Proc. R. Soc. A Math. Phys. Eng. Sci.* **1924**, *106* (738), 463–477.

(53) Plimpton, S. J.; Lawton, W. E. A Very Accurate Test of Coulomb's Law of Force Between Charges. *Phys. Rev.* **1936**, *50* (11), 1066–1071.

(54) Toukmaji, A. Y.; Board, J. A. Ewald Summation Techniques in Perspective: A Survey. *Comput. Phys. Commun.* **1996**, *95* (2-3), 73–92.

(55) Deserno, M.; Holm, C. How to Mesh up Ewald Sums. I. A Theoretical and Numerical Comparison of Various Particle Mesh Routines. *J. Chem. Phys.* **1998**, *109*, 7678−93.

(56) Wang, Y.; Izvekov, S.; Yan, T.; Voth, G. A. Multiscale Coarse-Graining of Ionic Liquids. *J. Phys. Chem. B* **2006**, *110*, 3564–3575.

(57) Liu, Z.; Wu, X.; Wang, W. A Novel United-Atom Force Field for Imidazolium-Based Ionic Liquids. *Phys. Chem. Chem. Phys.* **2006**, *8* (9), 1096–1104.

(58) Lippert, R. A.; Bowers, K. J.; Dror, R. O.; Eastwood, M. P.; Gregersen, B. A.; Klepeis, J. L.; Kolossvary, I.; Shaw, D. E. A Common, Avoidable Source of Error in Molecular Dynamics Integrators. *J. Chem. Phys.* **2007**, *126* (4), 046101.

(59) Verlet, L. Computer "Experiments" on Classical Fluids. I. Thermodynamical Properties of Lennard-Jones Molecules. *Phys. Rev.* **1967**, *159* (1), 98–103.

(60) Hoover, W. Canonical Dynamics: Equilibrium Phase-Space Distributions. *Phys. Rev. A* **1985**, *31* (3), 1695–1697.

(61) Henkelman, G.; Arnaldsson, A.; Jónsson, H. A Fast and Robust Algorithm for Bader Decomposition of Charge Density. *Comput. Mater. Sci.* **2006**, *36* (3), 354–360.

(62) Bayly, C. I.; Cieplak, P.; Cornell, W.; Kollman, P. A. A Well-Behaved Electrostatic Potential Based Method Using Charge Restraints for Deriving Atomic Charges: The RESP Model. *J. Phys. Chem.* **1993**, *97* (40), 10269–10280.

(63) Reed, S. K.; Lanning, O. J.; Madden, P. a. Electrochemical Interface between an Ionic Liquid and a Model Metallic Electrode. *J. Chem. Phys.* **2007**, *126* (8), 084704.

(64) Banhart, F.; Kotakoski, J.; Krasheninnikov, A. V. Structural Defects in Graphene. *ACS Nano* **2011**, *5* (1), 26–41.

(65)   Kotakoski, J.; Meyer, J. C.; Kurasch, S.; Santos-Cottin, D.; Kaiser, U.; Krasheninnikov, A. V. Stone-Wales-Type Transformations in Carbon Nanostructures Driven by Electron Irradiation. *Phys. Rev. B* **2011**, *83* (24), 245420.

(66)   Kotakoski, J.; Krasheninnikov, A.; Kaiser, U.; Meyer, J. From Point Defects in Graphene to Two-Dimensional Amorphous Carbon. *Phys. Rev. Lett.* **2011**, *106* (10), 105505.

(67)   Ugeda, M. M.; Brihuega, I.; Hiebel, F.; Mallet, P.; Veuillen, J.-Y.; Gómez-Rodríguez, J. M.; Ynduráin, F. Electronic and Structural Characterization of Divacancies in Irradiated Graphene. *Phys. Rev. B* **2012**, *85* (12), 121402.

(68)   Perdew, J. P.; Wang, Y. Accurate and Simple Analytic Representation of the Electron-Gas Correlation Energy. *Phys. Rev. B* **1992**, *45* (23), 13244–13249.

(69)   Kresse, G.; Joubert, D. From Ultrasoft Pseudopotentials to the Projector Augmented-Wave Method. *Phys. Rev. B* **1999**, *59* (3), 11–19.

(70)   Monkhorst, H. J.; Pack, J. D. Special Points for Brillouin-Zone Integrations. *Phys. Rev. B* **1976**, *13* (12), 5188–5192.

(71)   Ma, J.; Alfè, D.; Michaelides, A.; Wang, E. Stone-Wales Defects in Graphene and Other Planar sp2-Bonded Materials. *Phys. Rev. B* **2009**, *80* (3), 033407.

(72)   Li, L.; Reich, S.; Robertson, J. Defect Energies of Graphite: Density-Functional Calculations. *Phys. Rev. B* **2005**, *72* (18), 184109.

(73)   Ugeda, M. M.; Fernández-Torre, D.; Brihuega, I.; Pou, P.; Martínez-Galera, a. J.; Pérez, R.; Gómez-Rodríguez, J. M. Point Defects on Graphene on Metals. *Phys. Rev. Lett.* **2011**, *107* (11), 116803.

(74)   El-Barbary, A. A.; Telling, R. H.; Ewels, C. P.; Heggie, M. I.; Briddon, P. R. Structure and Energetics of the Vacancy in Graphite. *Phys. Rev. B* **2003**, *68* (14), 144107.

(75)   Zhang, H.; Zhao, M.; Yang, X.; Xia, H.; Liu, X.; Xia, Y. Diffusion and Coalescence of Vacancies and Interstitials in Graphite: A First-Principles Study. *Diam. Relat. Mater.* **2010**, *19* (10), 1240–1244.

(76)   Lusk, M. T.; Wu, D. T.; Carr, L. D. Graphene Nanoengineering and the Inverse Stone-Thrower-Wales Defect. *Phys. Rev. B* **2010**, *81* (15), 155444.

(77)   Ma, Y. Simulation of Interstitial Diffusion in Graphite. *Phys. Rev. B* **2007**, *76* (7), 075419.

(78) Lehtinen, P.; Foster, A. S.; Ayuela, A.; Krasheninnikov, A.; Nordlund, K.; Nieminen, R. Magnetic Properties and Diffusion of Adatoms on a Graphene Sheet. *Phys. Rev. Lett.* **2003**, *91* (1), 017202.

(79) Lherbier, A.; Dubois, S. M.-M.; Declerck, X.; Niquet, Y.-M.; Roche, S.; Charlier, J.-C. Transport Properties of Graphene Containing Structural Defects. *Phys. Rev. B* **2012**, *86* (7), 075402.

(80) Shirodkar, S. N.; Waghmare, U. V. Electronic and Vibrational Signatures of Stone-Wales Defects in Graphene: First-Principles Analysis. *Phys. Rev. B* **2012**, *86* (16), 165401.

(81) Castro Neto, A. H.; Guinea, F.; Peres, N. M. R.; Novoselov, K. S.; Geim, A. K. The Electronic Properties of Graphene. *Rev. Mod. Phys.* **2009**, *81* (1), 109–162.

(82) Vatamanu, J.; Borodin, O.; Smith, G. D. Molecular Insights into the Potential and Temperature Dependences of the Differential Capacitance of a Room-Temperature Ionic Liquid at Graphite Electrodes. *J. Am. Chem. Soc.* **2010**, *132* (42), 14825–14833.

(83) Fedorov, M. V; Lynden-Bell, R. M. Probing the Neutral Graphene-Ionic Liquid Interface: Insights from Molecular Dynamics Simulations. *Phys. Chem. Chem. Phys.* **2012**, *14* (8), 2552–2556.

(84) Paek, E.; Pak, A. J.; Hwang, G. S. Curvature Effects on the Interfacial Capacitance of Carbon Nanotubes in an Ionic Liquid. *J. Phys. Chem. C* **2013**, *117* (45), 23539–23546.

(85) Feng, G.; Qiao, R.; Huang, J.; Dai, S.; Sumpter, B. G.; Meunier, V. The Importance of Ion Size and Electrode Curvature on Electrical Double Layers in Ionic Liquids. *Phys. Chem. Chem. Phys.* **2011**, *13* (3), 1152–1161.

(86) Xing, L.; Vatamanu, J.; Smith, G. D.; Bedrov, D. Nanopatterning of Electrode Surfaces as a Potential Route to Improve the Energy Density of Electric Double-Layer Capacitors: Insight from Molecular Simulations. *J. Phys. Chem. Lett.* **2012**, *3* (9), 1124–1129.

(87) Merlet, C.; Péan, C.; Rotenberg, B.; Madden, P. A.; Simon, P.; Salanne, M. Simulating Supercapacitors: Can We Model Electrodes As Constant Charge Surfaces? *J. Phys. Chem. Lett.* **2013**, *4* (2), 264–268.

(88) Paek, E.; Pak, A. J.; Hwang, G. S. On the Influence of Polarization Effects in Predicting the Interfacial Structure and Capacitance of Graphene-like Electrodes in Ionic Liquids. *J. Chem. Phys.* **2015**, *142* (2015), 024701.

(89)   Cockayne, E.; Rutter, G. M.; Guisinger, N. P.; Crain, J. N.; First, P. N.; Stroscio, J. A. Grain Boundary Loops in Graphene. *Phys. Rev. B* **2011**, *83* (19), 195425.

(90)   Terrones, H.; Lv, R.; Terrones, M.; Dresselhaus, M. S. The Role of Defects and Doping in 2D Graphene Sheets and 1D Nanoribbons. *Reports Prog. Phys.* **2012**, *75* (6), 062501.

(91)   Zhan, D.; Yan, J.; Lai, L.; Ni, Z.; Liu, L.; Shen, Z. Engineering the Electronic Structure of Graphene. *Adv. Mater.* **2012**, *24*, 4055–4069.

(92)   Lv, R.; Li, Q.; Botello-Méndez, A. R.; Hayashi, T.; Wang, B.; Berkdemir, A.; Hao, Q.; Elías, A. L.; Cruz-Silva, R.; Gutiérrez, H. R.; et al. Nitrogen-Doped Graphene: Beyond Single Substitution and Enhanced Molecular Sensing. *Sci. Rep.* **2012**, *2*, 586.

(93)   Kramm, U. I.; Herrmann-Geppert, I.; Behrends, J.; Lips, K.; Fiechter, S.; Bogdanoff, P. On an Easy Way To Prepare Metal–Nitrogen Doped Carbon with Exclusive Presence of MeN$_4$-Type Sites Active for the ORR. *J. Am. Chem. Soc.* **2016**, jacs.5b11015.

(94)   Jeong, H. M.; Lee, J. W.; Shin, W. H.; Choi, Y. J.; Shin, H. J.; Kang, J. K.; Choi, J. W. Nitrogen-Doped Graphene for High-Performance Ultracapacitors and the Importance of Nitrogen-Doped Sites at Basal Planes. *Nano Lett.* **2011**, *11* (6), 2472–2477.

(95)   Qiu, Y.; Zhang, X.; Yang, S. High Performance Supercapacitors Based on Highly Conductive Nitrogen-Doped Graphene Sheets. *Phys. Chem. Chem. Phys.* **2011**, *13* (27), 12554–12558.

(96)   Kim, G.; Jhi, S.-H.; Lim, S.; Park, N. Effect of Vacancy Defects in Graphene on Metal Anchoring and Hydrogen Adsorption. *Appl. Phys. Lett.* **2009**, *94* (17), 173102.

(97)   Krasheninnikov, A. V.; Lehtinen, P. O.; Foster, A. S.; Pyykkö, P.; Nieminen, R. M. Embedding Transition-Metal Atoms in Graphene: Structure, Bonding, and Magnetism. *Phys. Rev. Lett.* **2009**, *102* (12), 126807–1.

(98)   Santos, E. J. G.; Ayuela, A.; Sánchez-Portal, D. First-Principles Study of Substitutional Metal Impurities in Graphene: Structural, Electronic and Magnetic Properties. *New J. Phys.* **2010**, *12* (5), 053012.

(99)   Rodríguez-Manzo, J. A.; Cretu, O.; Banhart, F. Trapping of Metal Atoms in Vacancies of Carbon Nanotubes and Graphene. *ACS Nano* **2010**, *4* (6), 3422–3428.

(100) Choi, W. I.; Jhi, S.-H.; Kim, K.; Kim, Y.-H. Divacancy-Nitrogen-Assisted

Transition Metal Dispersion and Hydrogen Adsorption in Defective Graphene: A First-Principles Study. *Phys. Rev. B* **2010**, *81* (8), 085441.

(101) Jorgensen, W. L.; Maxwell, D. S.; Tirado-Rives, J. Development and Testing of the OPLS All-Atom Force Field on Conformational Energetics and Properties of Organic Liquids. *J. Am. Chem. Soc.* **1996**, *118* (45), 11225–11236.

(102) Heinz, H.; Vaia, R. A.; Farmer, B. L.; Naik, R. R. Accurate Simulation of Surfaces and Interfaces of Face-Centered Cubic Metals Using 12−6 and 9−6 Lennard-Jones Potentials. *J. Phys. Chem. C* **2008**, *112* (44), 17281–17290.

(103) Minonishi, Y.; Ishioka, S.; Koiwa, M.; Morozumi, S.; Yamaguchi, M. The Core Structure of $1/3\langle 1123 \rangle$ {1122} Edge Dislocations in H.C.P. Metals. *Philos. Mag. A* **2006**, *43* (4), 1017–1026.

(104) Kumełan, J.; Kamps, Á. P.-S.; Tuma, D.; Maurer, G. Solubility of CO in the Ionic Liquid [bmim][PF$_6$]. *Fluid Phase Equilib.* **2005**, *228-229*, 207–211.

(105) Plimpton, S. Fast Parallel Algorithms for Short-Range Molecular Dynamics. *J. Comput. Phys.* **1995**, *117* (1), 1–19.

(106) Wu, M.; Cao, C.; Jiang, J. Z. Electronic Structure of Substitutionally Mn-Doped Graphene. *New J. Phys.* **2010**, *12* (6), 063020.

(107) Wang, S.; Li, S.; Cao, Z.; Yan, T. Molecular Dynamic Simulations of Ionic Liquids at Graphite Surface. *J. Phys. Chem. C* **2010**, *114* (2), 990–995.

(108) Mezger, M.; Schröder, H.; Reichert, H.; Schramm, S.; Okasinski, J. S.; Schöder, S.; Honkimäki, V.; Deutsch, M.; Ocko, B. M.; Ralston, J.; et al. Molecular Layering of Fluorinated Ionic Liquids at a Charged Sapphire (0001) Surface. *Science* **2008**, *322* (5900), 424–428.

(109) Liu, Y.; Zhang, Y.; Wu, G.; Hu, J. Coexistence of Liquid and Solid Phases of Bmim-PF$_6$ Ionic Liquid on Mica Surfaces at Room Temperature. *J. Am. Chem. Soc.* **2006**, *128* (23), 7456–7457.

(110) Bovio, S.; Podesta, A.; Lenardi, C.; Milani, P.; Na, C. I. M. I.; Fisica, D. Evidence of Extended Solidlike Layering in [Bmim][NTf$_2$] Ionic Liquid Thin Films at Room-Temperature. *J. Phys. Chem. B* **2009**, *113* (110), 6600–6603.

(111) Bazant, M. Z.; Storey, B. D.; Kornyshev, A. A. Double Layer in Ionic Liquids: Overscreening vs. Crowding. *Phys. Rev. Lett.* **2011**, *106*, 046102.

(112) Cohen, A. J.; Mori-Sánchez, P.; Yang, W. Insights into Current Limitations of Density Functional Theory. *Science* **2008**, *321* (5890), 792–794.

(113) Brownson, D. A. C.; Munro, L. J.; Kampouris, D. K.; Banks, C. E. Electrochemistry of Graphene: Not Such a Beneficial Electrode Material? *RSC Adv.* **2011**, *1* (6), 978–988.

(114) Song, W.; Ji, X.; Deng, W.; Chen, Q.; Shen, C.; Banks, C. E. Graphene Ultracapacitors: Structural Impacts. *Phys. Chem. Chem. Phys.* **2013**, *15* (13), 4799–4803.

(115) Banerjee, S.; Shim, J.; Rivera, J.; Jin, X.; Estrada, D.; Solovyeva, V.; You, X.; Pak, J.; Pop, E.; Aluru, N.; et al. Electrochemistry at the Edge of a Single Graphene Layer in a Nanopore. *ACS Nano* **2013**, *7* (1), 834–843.

(116) Jia, X.; Campos-Delgado, J.; Terrones, M.; Meunier, V.; Dresselhaus, M. S. Graphene Edges: A Review of Their Fabrication and Characterization. *Nanoscale* **2011**, *3* (1), 86–95.

(117) Zhang, C.; Peng, Z.; Lin, J.; Zhu, Y.; Ruan, G.; Hwang, C.-C.; Lu, W.; Hauge, R. H.; Tour, J. M. Splitting of a Vertical Multiwalled Carbon Nanotube Carpet to a Graphene Nanoribbon Carpet and Its Use in Supercapacitors. *ACS Nano* **2013**, *7* (6), 5151–5159.

(118) Vosko, S. H.; Wilk, L.; Nusair, M. Accurate Spin-Dependent Electron Liquid Correlation Energies for Local Spin Density Calculations: A Critical Analysis. *Can. J. Phys.* **1980**, *58*, 1200–1211.

(119) Hod, O.; Barone, V.; Peralta, J. E.; Scuseria, G. E. Enhanced Half-Metallicity in Edge-Oxidized Zigzag Graphene Nanoribbons. *Nano Lett.* **2007**, *7* (8), 2295–2299.

(120) Lee, G.; Cho, K. Electronic Structures of Zigzag Graphene Nanoribbons with Edge Hydrogenation and Oxidation. *Phys. Rev. B* **2009**, *79* (16), 165440.

(121) Son, Y.-W.; Cohen, M. L.; Louie, S. G. Energy Gaps in Graphene Nanoribbons. *Phys. Rev. Lett.* **2006**, *97* (21), 216803.

(122) Pisani, L.; Chan, J.; Montanari, B.; Harrison, N. Electronic Structure and Magnetic Properties of Graphitic Ribbons. *Phys. Rev. B* **2007**, *75* (6), 064418.

(123) Liu, W.; Yan, X.; Chen, J.; Feng, Y.; Xue, Q. Novel and High-Performance Asymmetric Micro-Supercapacitors Based on Graphene Quantum Dots and Polyaniline Nanofibers. *Nanoscale* **2013**, *5* (13), 6053–6062.

(124) Xu, Y.; Lin, Z.; Zhong, X.; Huang, X.; Weiss, N. O.; Huang, Y.; Duan, X. Holey Graphene Frameworks for Highly Efficient Capacitive Energy Storage. *Nat. Commun.* **2014**, *5*.

(125) Ghatee, M. H.; Moosavi, F. Physisorption of Hydrophobic and Hydrophilic 1-Alkyl-3-Methylimidazolium Ionic Liquids on the Graphenes. *J. Phys. Chem. C* **2011**, *115* (13), 5626–5636.

(126) Chen, D.; Feng, H.; Li, J. Graphene Oxide: Preparation, Functionalization, and Electrochemical Applications. *Chem. Rev.* **2012**, *112* (11), 6027–6053.

(127) Zhu, Y.; James, D. K.; Tour, J. M. New Routes to Graphene, Graphene Oxide and Their Related Applications. *Adv. Mater.* **2012**, *24* (36), 4924–4955.

(128) Pei, S.; Cheng, H. M. The Reduction of Graphene Oxide. *Carbon N. Y.* **2012**, *50* (9), 3210–3228.

(129) Bikkarolla, S. K.; Cumpson, P.; Joseph, P.; Papakonstantinou, P. Oxygen Reduction Reaction by Electrochemically Reduced Graphene Oxide. *Faraday Discuss.* **2014**, *173*, 415–428.

(130) Xu, B.; Yue, S.; Sui, Z.; Zhang, X.; Hou, S.; Cao, G.; Yang, Y. What Is the Choice for Supercapacitors: Graphene or Graphene Oxide? *Energy Environ. Sci.* **2011**, *4*, 2826.

(131) Zhao, B.; Liu, P.; Jiang, Y.; Pan, D.; Tao, H.; Song, J.; Fang, T.; Xu, W. Supercapacitor Performances of Thermally Reduced Graphene Oxide. *J. Power Sources* **2012**, *198* (2012), 423–427.

(132) Karthika, P. Functionalized Exfoliated Graphene Oxide as Supercapacitor Electrodes. *Soft Nanosci. Lett.* **2012**, *02* (October), 59–66.

(133) Chen, Y.; Zhang, X.; Zhang, D.; Yu, P.; Ma, Y. High Performance Supercapacitors Based on Reduced Graphene Oxide in Aqueous and Ionic Liquid Electrolytes. *Carbon N. Y.* **2011**, *49* (2), 573–580.

(134) Kim, T.; Chang Kang, H.; Thanh Tung, T.; Don Lee, J.; Kim, H.; Seok Yang, W.; Gyu Yoon, H.; Suh, K. S. Ionic Liquid-Assisted Microwave Reduction of Graphite Oxide for Supercapacitors. *RSC Adv.* **2012**, *2*, 8808–8812.

(135) Buglione, L.; Chng, E. L. K.; Ambrosi, A.; Sofer, Z.; Pumera, M. Graphene Materials Preparation Methods Have Dramatic Influence upon Their Capacitance. *Electrochem. commun.* **2012**, *14* (2012), 5–8.

(136) Pope, M. A.; Korkut, S.; Punckt, C.; Aksay, I. A. Supercapacitor Electrodes Produced through Evaporative Consolidation of Graphene Oxide-Water-Ionic Liquid Gels. *J. Electrochem. Soc.* **2013**, *160* (10), A1653–A1660.

(137) Deyoung, A. D.; Park, S.; Dhumal, N. R.; Shim, Y.; Jung, Y.; Kim, H. J. Graphene

Oxide Supercapacitors: A Computer Simulation Study. *J. Phys. Chem. C* **2014**, *118* (32), 18472–18480.

(138) Kerisit, S.; Schwenzer, B.; Vijayakumar, M. Effects of Oxygen-Containing Functional Groups on Supercapacitor Performance. *J. Phys. Chem. Lett.* **2014**, *5* (13), 2330–2334.

(139) Xu, K.; Ji, X.; Chen, C.; Wan, H.; Miao, L.; Jiang, J. Electrochemical Double Layer near Polar Reduced Graphene Oxide Electrode: Insights from Molecular Dynamic Study. *Electrochim. Acta* **2015**, *166* (2015), 142–149.

(140) Pak, A. J.; Paek, E.; Hwang, G. S. Impact of Graphene Edges on Enhancing the Performance of Electrochemical Double Layer Capacitors. *J. Phys. Chem. C* **2014**, *118*, 21770–21777.

(141) Paek, E.; Pak, A. J.; Hwang, G. S. Large Capacitance Enhancement Induced by Metal-Doping in Graphene-Based Supercapacitors: A First-Principles-Based Assessment. *ACS Appl. Mater. Interfaces* **2014**, *6* (15), 12168–12176.

(142) Lerf, A.; He, H.; Forster, M.; Klinowski, J. Structure of Graphite Oxide Revisited. *J. Phys. Chem. B* **1998**, *5647* (97), 4477–4482.

(143) Gao, W.; Alemany, L. B.; Ci, L.; Ajayan, P. M. New Insights into the Structure and Reduction of Graphite Oxide. *Nat. Chem.* **2009**, *1* (5), 403–408.

(144) Cai, W.; Piner, R. D.; Stadermann, F. J.; Park, S.; Shaibat, M. A.; Ishii, Y.; Yang, D.; Velamakanni, A.; An, S. J.; Stoller, M.; et al. Synthesis and Solid-State NMR Structural Characterization of 13C-Labeled Graphite Oxide. *Science (80-.).* **2008**, *321*, 1815–1817.

(145) Erickson, K.; Erni, R.; Lee, Z.; Alem, N.; Gannett, W.; Zettl, A. Determination of the Local Chemical Structure of Graphene Oxide and Reduced Graphene Oxide. *Adv. Mater.* **2010**, *22* (40), 4467–4472.

(146) Zhou, S.; Bongiorno, A. Origin of the Chemical and Kinetic Stability of Graphene Oxide. *Sci. Rep.* **2013**, *3*, 2484.

(147) Yan, J.-A.; Chou, M. Y. Oxidation Functional Groups on Graphene: Structural and Electronic Properties. *Phys. Rev. B* **2010**, *82* (12), 125403.

(148) Gaus, M.; Goez, A.; Elstner, M. Parametrization and Benchmark of DFTB3 for Organic Molecules. *J. Chem. Theory Comput.* **2013**, *9*, 338–354.

(149) Elstner, M.; Porezag, D.; Jungnickel, G.; Elsner, J.; Haugk, M.; Frauenheim, T.; Suhai, S.; Seifert, G. Self-Consistent-Charge Density-Functional Tight-Binding

Method for Simulations of Complex Materials Properties. *Phys. Rev. B* **1998**, *58* (11), 7260–7268.

(150) Gaus, M.; Cui, Q.; Elstner, M. DFTB3: Extension of the Self-Consistent-Charge Density-Functional Tight-Binding Method (SCC-DFTB). *J. Chem. Theory* **2011**, *7*, 931–948.

(151) Mulliken, R. S. Electronic Population Analysis on LCAO-MO Molecular Wave Functions. I. *J. Chem. Phys.* **1955**, *23* (10), 1833.

(152) Borodin, O.; Gorecki, W.; Smith, G. D.; Armand, M. Molecular Dynamics Simulation and Pulsed-Field Gradient NMR Studies of Bis(fluorosulfonyl)imide (FSI) and Bis[(trifluoromethyl)sulfonyl]imide (TFSI)-Based Ionic Liquids. *J. Phys. Chem. B* **2010**, *114*, 6786–6798.

(153) Lopes, N. C.; Deschamps, J.; Pa, A. H. Modeling Ionic Liquids Using a Systematic All-Atom Force Field. *J. Phys. Chem. B* **2004**, *108*, 2038–2047.

(154) Canongia Lopes, J. N.; Shimizu, K.; Pádua, A. A. H.; Umebayashi, Y.; Fukuda, S.; Fujii, K.; Ishiguro, S. Potential Energy Landscape of Bis(fluorosulfonyl)amide. *J. Phys. Chem. B* **2008**, *112* (31), 9449–9455.

(155) Battezzati, L.; Pisani, C.; Ricca, F. Equilibrium Conformation and Surface Motion of Hydrocarbon Molecules Physisorbed on Graphit. *J. Chem. Soc. Faraday Trans. 2* **1975**, *71*, 1629–1639.

(156) Pak, A. J.; Paek, E.; Hwang, G. S. Tailoring the Performance of Graphene-Based Supercapacitors Using Topological Defects: A Theoretical Assessment. *Carbon* **2014**, *68* (512), 734–741.

(157) Wood, B. C.; Ogitsu, T.; Otani, M.; Biener, J. First-Principles-Inspired Design Strategies for Graphene-Based Supercapacitor Electrodes. *J. Phys. Chem. C* **2014**, *118* (1), 4–15.

(158) Mattevi, C.; Eda, G.; Agnoli, S.; Miller, S.; Mkhoyan, K. A.; Celik, O.; Mastrogiovanni, D.; Granozzi, G.; Garfunkel, E.; Chhowalla, M. Evolution of Electrical, Chemical, and Structural Properties of Transparent and Conducting Chemically Derived Graphene Thin Films. *Adv. Funct. Mater.* **2009**, *19* (16), 2577–2583.

(159) Robertson, J.; O'Reilly, E. P. Electronic and Atomic Structure of Amorphous Carbon. *Phys. Rev. B* **1987**, *35* (6), 2946–2957.

(160) Dreyer, D. R.; Park, S.; Bielawski, C. W.; Ruoff, R. S. The Chemistry of Graphene Oxide. *Chem. Soc. Rev.* **2010**, *39* (1), 228–240.

(161) Shimizu, K.; Pensado, A.; Malfreyt, P.; Pádua, A. a. H.; Canongia Lopes, J. N. 2D or Not 2D: Structural and Charge Ordering at the Solid-Liquid Interface of the 1-(2-Hydroxyethyl)-3-Methylimidazolium Tetrafluoroborate Ionic Liquid. *Faraday Discuss.* **2012**, *154*, 155–169.

(162) Merlet, C.; Limmer, D. T.; Salanne, M.; van Roij, R.; Madden, P. A.; Chandler, D.; Rotenberg, B. The Electric Double Layer Has a Life of Its Own. *J. Phys. Chem. C* **2014**, *118*, 18291–18298.

(163) Huang, H.; Li, Z.; She, J.; Wang, W. Oxygen Density Dependent Band Gap of Reduced Graphene Oxide. *J. Appl. Phys.* **2012**, *111* (5), 054317.

(164) Bagri, A.; Mattevi, C.; Acik, M.; Chabal, Y. J.; Chhowalla, M.; Shenoy, V. B. Structural Evolution During the Reduction of Chemically Derived Graphene Oxide. *Nat. Chem.* **2010**, *2* (7), 581–587.

(165) Schnorr, J. M.; Swager, T. M. Emerging Applications of Carbon Nanotubes. *Chem. Mater.* **2011**, *23* (3), 646–657.

(166) Bandaru, P. R. Electrical Properties and Applications of Carbon Nanotube Structures. *J. Nanosci. Nanotechnol.* **2007**, *7* (3), 1–29.

(167) An, K. H.; Won, S. K.; Park, Y. S.; Choi, Y. C.; Lee, S. M.; Chung, D. C.; Bae, D. J.; Lim, S. C.; Lee, Y. H. Supercapacitors Using Single-Walled Carbon Nanotube Electrodes. *Adv. Mater.* **2001**, *13* (7), 497–500.

(168) Honda, Y.; Haramoto, T.; Takeshige, M.; Shiozaki, H.; Kitamura, T.; Yoshikawa, K.; Ishikawa, M. Performance of Electric Double-Layer Capacitor with Vertically Aligned MWCNT Sheet Electrodes Prepared by Transfer Methodology. *J. Electrochem. Soc.* **2008**, *155* (12), A930–A935.

(169) Kaempgen, M.; Chan, C. K.; Ma, J.; Cui, Y.; Gruner, G. Printable Thin Film Supercapacitors Using Single-Walled Carbon Nanotubes. *Nano Lett.* **2009**, *9* (5), 1872–1876.

(170) Lu, W.; Qu, L.; Henry, K.; Dai, L. High Performance Electrochemical Capacitors from Aligned Carbon Nanotube Electrodes and Ionic Liquid Electrolytes. *J. Power Sources* **2009**, *189* (2), 1270–1277.

(171) Kim, B.-W.; Chung, H.-G.; Min, B.-K.; Kim, H.-G.; Kim, W. Electrochemical Capacitors Based on Aligned Carbon Nanotubes Directly Synthesized on Tantalum Substrates. *Bull. Korean Chem. Soc.* **2010**, *31* (12), 3697–3702.

(172) Honda, Y.; Takeshige, M.; Shiozaki, H.; Kitamura, T.; Yoshikawa, K.; Chakrabarti, S.; Suekane, O.; Pan, L.; Nakayama, Y.; Yamagata, M.; et al. Vertically Aligned

Double-Walled Carbon Nanotube Electrode Prepared by Transfer Methodology for Electric Double Layer Capacitor. *J. Power Sources* **2008**, *185* (2), 1580–1584.

(173) Feng, G.; Cummings, P. T. Supercapacitor Capacitance Exhibits Oscillatory Behavior as a Function of Nanopore Size. *J. Phys. Chem. Lett.* **2011**, *2* (22), 2859–2864.

(174) Shim, Y.; Kim, H. J. Nanoporous Carbon Supercapacitors in an Ionic Liquid: A Computer Simulation Study. *ACS Nano* **2010**, *4* (4), 2345–2355.

(175) Huang, J.; Sumpter, B. G.; Meunier, V.; Yushin, G.; Portet, C.; Gogotsi, Y. Curvature Effects in Carbon Nanomaterials: Exohedral versus Endohedral Supercapacitors. *J. Mater. Res.* **2010**, *25* (08), 1525–1531.

(176) Feng, G.; Li, S.; Atchison, J. S.; Presser, V.; Cummings, P. T. Molecular Insights into Carbon Nanotube Supercapacitors : Capacitance Independent of Voltage and Temperature. *J. Phys. Chem. C* **2013**, *117* (18), 9178–9186.

(177) Béguin, F.; Presser, V.; Balducci, A.; Frackowiak, E. Carbons and Electrolytes for Advanced Supercapacitors. *Adv. Mater.* **2014**, *26* (14), 2219–2251.

(178) Kondrat, S.; Kornyshev, A. Superionic State in Double-Layer Capacitors with Nanoporous Electrodes. *J. Phys. Condens. Matter* **2011**, *23* (2), 022201.

(179) Xing, L.; Vatamanu, J.; Borodin, O.; Bedrov, D. On the Atomistic Nature of Capacitance Enhancement Generated by Ionic Liquid Electrolyte Confined in Subnanometer Pores. *J. Phys. Chem. Lett.* **2013**, *4*, 132–140.

(180) Jiang, D. E.; Jin, Z.; Wu, J. Oscillation of Capacitance inside Nanopores. *Nano Lett.* **2011**, *11* (12), 5373–5377.

(181) Wu, P.; Huang, J.; Meunier, V.; Sumpter, B. G.; Qiao, R. Voltage Dependent Charge Storage Modes and Capacity in Subnanometer Pores. *J. Phys. Chem. Lett.* **2012**, *3* (13), 1732–1737.

(182) Spohr, H. V; Patey, G. N. Structural and Dynamical Properties of Ionic Liquids: Competing Influences of Molecular Properties. *J. Chem. Phys.* **2010**, *132* (15), 154504.

(183) Perkin, S. Ionic Liquids in Confined Geometries. *Phys. Chem. Chem. Phys.* **2012**, *14* (15), 5052–5062.

(184) Kondrat, S.; Wu, P.; Qiao, R.; Kornyshev, A. A. Accelerating Charging Dynamics in Subnanometre Pores. *Nat. Mater.* **2014**, *13* (4), 387–393.

(185) He, Y.; Qiao, R.; Vatamanu, J.; Borodin, O.; Bedrov, D.; Huang, J.; Sumpter, B. G. The Importance of Ion Packing on the Dynamics of Ionic Liquids during Micropore Charging. *J. Phys. Chem. Lett.* **2016**, *7*, 36–42.

(186) He, Y.; Huang, J.; Sumpter, B. G.; Kornyshev, A. A.; Qiao, R. Dynamic Charge Storage in Ionic Liquids-Filled Nanopores: Insight from a Computational Cyclic Voltammetry Study. *J. Phys. Chem. Lett.* **2014**, *6*, 22–30.

(187) Tsai, W.-Y.; Taberna, P.-L.; Simon, P. Electrochemical Quartz Crystal Microbalance (EQCM) Study of Ion Dynamics in Nanoporous Carbons. *J. Am. Chem. Soc.* **2014**, *136*, 8722–8728.

(188) Merlet, C.; Péan, C.; Rotenberg, B.; Madden, P. a; Daffos, B.; Taberna, P.-L.; Simon, P.; Salanne, M. Highly Confined Ions Store Charge More Efficiently in Supercapacitors. *Nat. Commun.* **2013**, *4*, 2701.

(189) Ohba, T.; Hata, K.; Chaban, V. V. Nanocrystallization of Imidazolium Ionic Liquid in Carbon Nanotubes. *J. Phys. Chem. C* **2015**, acs.jpcc.5b09423.

(190) Chen, S.; Wu, G.; Sha, M.; Huang, S. Transition of Ionicl Liquid [bmim][PF$_6$] from Liquid to High-Melting-Point Crystal When Confined in Carbon Nanotubes. *J. Am. Chem. Soc.* **2007**, *129*, 2416–2417.

(191) Daily, J. W.; Micci, M. M. Ionic Velocities in an Ionic Liquid under High Electric Fields Using All-Atom and Coarse-Grained Force Field Molecular Dynamics. *J. Chem. Phys.* **2009**, *131* (9), 094501.

(192) Roy, D.; Maroncelli, M. An Improved Four-Site Ionic Liquid Model. *J. Phys. Chem. B* **2010**, *114* (39), 12629–12631.

(193) Jorgensen, W. L.; Maxwell, D. S.; Tirado-rives, J. Development and Testing of the OPLS All-Atom Force Field on Conformational Energetics and Properties of Organic Liquids. *J. Am. Chem. Soc.* **1996**, *118* (15), 11225–11236.

(194) Rappe, A.; III, W. G. Charge Equilibration for Molecular Dynamics Simulations. *J. Phys. Chem.* **1991**, *95*, 3358–3363.

(195) van Duin, A. C. T.; Dasgupta, S.; Lorant, F.; Goddard, W. A. ReaxFF: A Reactive Force Field for Hydrocarbons. *J. Phys. Chem. A* **2001**, *105* (41), 9396–9409.

(196) Nakano, A. Parallel Multilevel Preconditioned Conjugate-Gradient Approach to Variable-Charge Molecular Dynamics. *Comput. Phys. Commun.* **1997**, *104* (1-3), 59–69.

(197) Chenoweth, K.; van Duin, A. C. T.; Goddard, W. a. ReaxFF Reactive Force Field

for Molecular Dynamics Simulations of Hydrocarbon Oxidation. *J. Phys. Chem. A* **2008**, *112* (5), 1040–1053.

(198) Choudhury, A. R.; Winterton, N.; Steiner, A.; Cooper, A. I.; Johnson, K. A. In Situ Crystallization of Low-Melting Ionic Liquids. *J. Am. Chem. Soc.* **2005**, *127* (48), 16792–16793.

(199) Baldessari, F. Electrokinetics in Nanochannels. Part I. Electric Double Layer Overlap and Channel-to-Well Equilibrium. *J. Colloid Interface Sci.* **2008**, *325* (2), 526–538.

(200) Centeno, T. A.; Sereda, O.; Stoeckli, F. Capacitance in Carbon Pores of 0.7 to 15 Nm: A Regular Pattern. *Phys. Chem. Chem. Phys.* **2011**, *13* (27), 12403–12406.

(201) Kondrat, S.; Pérez, C. R.; Presser, V.; Gogotsi, Y.; Kornyshev, A. A. Effect of Pore Size and Its Dispersity on the Energy Storage in Nanoporous Supercapacitors. *Energy Environ. Sci.* **2012**, *5* (4), 6474.

(202) Shi, Y. A Mimetic Porous Carbon Model by Quench Molecular Dynamics Simulation. *J. Chem. Phys.* **2008**, *128* (23), 234707.

(203) Stuart, S. J.; Tutein, A. B.; Harrison, J. a. A Reactive Potential for Hydrocarbons with Intermolecular Interactions. *J. Chem. Phys.* **2000**, *112* (14), 6472.

(204) Willems, T. F.; Rycroft, C. H.; Kazi, M.; Meza, J. C.; Haranczyk, M. Algorithms and Tools for High-Throughput Geometry-Based Analysis of Crystalline Porous Materials. *Microporous Mesoporous Mater.* **2012**, *149* (1), 134–141.

(205) Zhang, Y.; Brar, V. W.; Girit, C.; Zettl, A.; Crommie, M. F. Origin of Spatial Charge Inhomogeneity in Graphene. *Nat. Phys.* **2009**, *5* (10), 722–726.

(206) Raymundo-Piñero, E.; Kierzek, K.; Machnikowski, J.; Béguin, F. Relationship between the Nanoporous Texture of Activated Carbons and Their Capacitance Properties in Different Electrolytes. *Carbon N. Y.* **2006**, *44* (12), 2498–2507.

(207) Qie, L.; Chen, W.; Xu, H.; Xiong, X.; Jiang, Y.; Zou, F.; Hu, X.; Xin, Y.; Zhang, Z.; Huang, Y. Synthesis of Functionalized 3D Hierarchical Porous Carbon for High-Performance Supercapacitors. *Energy Environ. Sci.* **2013**, *6* (8), 2497.

(208) Ania, C. O.; Khomenko, V.; Raymundo-Piñero, E.; Parra, J. B.; Béguin, F. The Large Electrochemical Capacitance of Microporous Doped Carbon Obtained by Using a Zeolite Template. *Adv. Funct. Mater.* **2007**, *17* (11), 1828–1836.

(209) Fletcher, S.; Black, V. J.; Kirkpatrick, I. A Universal Equivalent Circuit for Carbon-Based Supercapacitors. *J. Solid State Electrochem.* **2014**, *18* (5), 1377–1387.

(210) Hasbach, A.; Retter, U.; Siegler, K.; Kautek, W. On the Impedance of Porous Electrodes – Double-Layer Charging and Charge Transfer on an Inhomogeneous inside Electrode Surface. *J. Electroanal. Chem.* **2004**, *561*, 29–35.

(211) Ike, I. S.; Sigalas, I.; Iyuke, S.; Ozoemena, K. I. An Overview of Mathematical Modeling of Electrochemical Supercapacitors/ultracapacitors. *J. Power Sources* **2015**, *273*, 264–277.

(212) Zhang, L.; Yang, X.; Zhang, F.; Long, G.; Zhang, T.; Leng, K.; Zhang, Y.; Huang, Y.; Ma, Y.; Zhang, M.; et al. Controlling the Effective Surface Area and Pore Size Distribution of sp2 Carbon Materials and Their Impact on the Capacitance Performance of These Materials. *J. Am. Chem. Soc.* **2013**, *135*, 5921–5929.

(213) Chen, W.; Rakhi, R. B.; Hedhili, M. N.; Alshareef, H. N. Shape-Controlled Porous Nanocarbons for High Performance Supercapacitors. *J. Mater. Chem. A* **2014**, *2* (15), 5236.

(214) McDonough, J. K.; Frolov, A. I.; Presser, V.; Niu, J.; Miller, C. H.; Ubieto, T.; Fedorov, M. V.; Gogotsi, Y. Influence of the Structure of Carbon Onions on Their Electrochemical Performance in Supercapacitor Electrodes. *Carbon N. Y.* **2012**, *50* (9), 3298–3309.

(215) Feng, G.; Qiao, R.; Huang, J.; Sumpter, B. G.; Meunier, V. Ion Distribution in Electrified Micropores and Its Role in the Anomalous Enhancement of Capacitance. *ACS Nano* **2010**, *4* (4), 2382–2390.

(216) Merlet, C.; Rotenberg, B.; Madden, P. A.; Taberna, P.-L.; Simon, P.; Gogotsi, Y.; Salanne, M. On the Molecular Origin of Supercapacitance in Nanoporous Carbon Electrodes. *Nat. Mater.* **2012**, *11* (4), 306–310.

(217) Kuroda, M.; Tersoff, J.; Martyna, G. Nonlinear Screening in Multilayer Graphene Systems. *Phys. Rev. Lett.* **2011**, *106* (11), 1–4.

(218) Wang, Y.; Voth, G. A. Tail Aggregation and Domain Diffusion in Ionic Liquids. *J. Phys. Chem. B* **2006**, *110* (37), 18601–18608.

(219) Fajardo, O. Y.; Bresme, F.; Kornyshev, a. a.; Urbakh, M. Electrotunable Lubricity with Ionic Liquid Nanoscale Films. *Sci. Rep.* **2015**, *5*, 7698.

(220) Wang, W.; Guo, S.; Lee, I.; Ahmed, K.; Zhong, J.; Favors, Z.; Zaera, F.; Ozkan, M.; Ozkan, C. S. Hydrous Ruthenium Oxide Nanoparticles Anchored to Graphene and Carbon Nanotube Hybrid Foam for Supercapacitors. *Sci. Rep.* **2014**, *4* (ii), 4452.

(221) Kuo, S.; Wu, N. Investigation of Pseudocapacitive Charge-Storage Reaction of MnO2 nH2O Supercapacitors in Aqueous Electrolytes. *J. Electrochem. Soc.* **2006**,

153 (7), A1317.

(222) Lee, Y.-H.; Chang, K.-H.; Hu, C.-C. Differentiate the Pseudocapacitance and Double-Layer Capacitance Contributions for Nitrogen-Doped Reduced Graphene Oxide in Acidic and Alkaline Electrolytes. *J. Power Sources* **2013**, *227*, 300–308.

(223) He, Y. Y.; Zhang, J. J.; Zhao, J. W. Influence of Graphene with Different Oxidation Degrees on Nickel Hydroxide Pseudocapacitor Characterization. *Acta Phys. - Chim. Sin.* **2014**, *30* (2), 297–304.

(224) Barcia, O. E.; D'Elia, E.; Frateur, I.; Mattos, O. R.; Pébère, N.; Tribollet, B. Application of the Impedance Model of de Levie for the Characterization of Porous Electrodes. *Electrochim. Acta* **2002**, *47* (13-14), 2109–2116.

(225) Candy, J. P.; Fouilloux, P.; Keddam, M.; Takenouti, H. The Pore Texture of Raney-Nickel Determined by Impedance Measurements. *Electrochim. Acta* **1982**, *27* (11), 1585–1593.

(226) Suss, M. E.; Baumann, T. F.; Worsley, M. A.; Rose, K. A.; Jaramillo, T. F.; Stadermann, M.; Santiago, J. G. Impedance-Based Study of Capacitive Porous Carbon Electrodes with Hierarchical and Bimodal Porosity. *J. Power Sources* **2013**, *241*, 266–273.

(227) Suss, M. E.; Porada, S.; Sun, X.; Biesheuvel, P. M.; Yoon, J.; Presser, V. Water Desalination via Capacitive Deionization: What Is It and What Can We Expect from It? *Energy Environ. Sci.* **2015**, *8* (8), 2296–2319.

(228) Fujimoto, T.; Awaga, K. Electric-Double-Layer Field-Effect Transistors with Ionic Liquids. *Phys. Chem. Chem. Phys.* **2013**, *15* (23), 8983–9006.

(229) Ono, S.; Miwa, K.; Seki, S.; Takeya, J. A Comparative Study of Organic Single-Crystal Transistors Gated with Various Ionic-Liquid Electrolytes. *Appl. Phys. Lett.* **2009**, *94* (6), 1–4.

(230) Hulea, I. N.; Fratini, S.; Xie, H.; Mulder, C. L.; Iossad, N. N.; Rastelli, G.; Ciuchi, S.; Morpurgo, A. F. Tunable Fröhlich Polarons in Organic Single-Crystal Transistors. *Nat. Mater.* **2006**, *5* (12), 982–986.

(231) Kergoat, L.; Herlogsson, L.; Piro, B.; Pham, M. C.; Horowitz, G.; Crispin, X.; Berggren, M. Tuning the Threshold Voltage in Electrolyte-Gated Organic Field-Effect Transistors. *Proc. Natl. Acad. Sci. U. S. A.* **2012**, *109* (22), 8394–8399.

Vita

Alexander J. Pak was born in New York City, NY and lived there through high school. His first real foray into the science was in a new biochemistry course taught in high school at the Horace Mann School. This class inspired him to pursue a bachelor's degree in Chemical Engineering at M.I.T in Cambridge, MA as part of the Class of 2010. After undergraduate school, Alex spent a year as a Junior Scientist at Nano Terra, Inc., a Cambridge-based start-up company, where he first experienced nanotechnology-related research. In August 2011, he began graduate studies in the McKetta Department of Chemical Engineering at the University of Texas at Austin. Under the guidance of Professor Gyeong S. Hwang, he pursued a Ph.D. in Chemical Engineering with his research topic on fundamental charge storage mechanisms using carbon-based nanomaterials for supercapacitor applications.

Permanent address (or email): alexander.jin.pak@gmail.com

This dissertation was typed by Alexander J. Pak.